Half-Heusler Thermoelectric Materials and Modules

Han Byul Kang

Dissertation submitted to the faculty of the Virginia Polytechnic Institute and State University in partial fulfillment of the requirements for the degree of

Doctor of Philosophy
In
Materials Science and Engineering

Shashank Priya, Chair
Alex O. Aning
Mitsuhiro Murayama
Giti Khodaparast

July 22th
Blacksburg, VA

Keywords: thermoelectric, half-Heusler, nanocomposite, alloy, oxidation, generator

Half-Heusler Thermoelectric Materials and Modules

Han Byul Kang

ABSTRACT

High temperature waste heat recovery has been gaining attention in recent years as it forms one of the largest sources of available energy. A rapid development of thermoelectric (TE) materials that can directly convert heat into electricity through the Seebeck effect, opens promising pathway for harvesting the thermal energy from the surroundings. In order to harvest the high-quality waste heat at elevated temperature, excellent thermal and mechanical stability of the TE materials is critical for a sustainable energy harvesting. In this respect, half-Heusler (hH) alloys are one of the promising high-temperature TE materials due to their high dimensionless thermoelectric figure of merit (zT) along with excellent mechanical and thermal stability. This dissertation demonstrates novel hH compositions and microstructures for the waste heat recovery systems. Focus in the thesis is on development of high performance hH TE materials with excellent in-air thermal stability at high temperatures (>700K). This will allow manufacturing of high efficiency and durable high temperature thermoelectric generators (TEGs).

In chapter 3 and 4, a comprehensive optimization of *n*-type MNiSn and *p*-type MCoSb (M = Hf, Zr, and Ti) compounds is investigated through systematic control of processing parameters during melting and sintering. The synthesis conditions were controlled to

achieve the phase purity, desired microstructure and the enhanced charge-carrier transport. Optimized n-type and p-type compositions are found to exhibit $zT_{max} \sim 1$ at 773 K.

Chapter 5 describes breakthrough in decoupling of TE parameters in n-type half-Heusler (hH) alloys through multi-scale nanocomposite architecture with tungsten nanoinclusions. The tungsten nanoparticles not only assist electron injection, thereby improving electrical conductivity, but also enhance the Seebeck coefficient through energy filtering effect. The microstructure comprises of disordered phases with feature sizes at multiple length scales, which assists in effective scattering of heat-carrying phonons over diverse mean-free-path ranges. Cumulatively, these effects are shown to result in outstanding thermoelectric performance of $zT_{max} \sim 1.4$ at 773 K and $zT_{avg} \sim 0.93$ between 300 and 973 K.

In order to deploy TE materials into a thermal energy conversion device, it is essential to understand the transformation behavior under thermal cycling at high temperatures. In-air thermal stability of the hH compositions is demonstrated in chapter 6. All the optimized compositions are found to be stable below 673 K in-air condition. The *n*-type MNiSn and *p*-type NbFeSb compounds were found to show good thermal stability even at higher temperatures (>773K), whereas MCoSb compounds did not exhibit similar level of stability.

Building upon the improved material performance and thermal stability, uni-coupled TE generators are demonstrated that exhibit high power density of 13.81 $W \cdot cm^{-2}$ and conversion efficiency of 10.9 % under a temperature difference of 674 K. The uni-couple TEG device shows stable performance for more than 150 hours at 873 K in air. These results are very promising for deployment of TE materials in waste heat recovery systems.

Half-Heusler Thermoelectric Materials and Modules

Han Byul Kang

GENERAL AUDIENCE ABSTRACT

Based on the 2012 international energy agency (IEA) report, global waste heat energy is estimated to be in the range of 246 Exajoule (1 EJ = 10^{18} J). Tapping even small fraction of this wasted energy through thermal energy harvesting techniques will allow us to generate significant magnitude of green energy. Thermoelectrics (TEs) are one of the most promising thermal energy conversion materials as they offer cost-effective and environmentally friendly option with solid-state silent operation and scalability. Among many different options for high temperature TE materials, half-Heusler system is one of the leading candidates as it has the potential to provide high performance and thermal stability at temperatures as high as 873 K.

The progress in developing practical half-Heusler materials has been limited for last two decades. Despite many publications, the maximum figure of merit (zT) of *n*-type half-Heusler materials has been stagnant (zT ~ 1.0). Further, there has been a lack of focus towards module development that can operate under realistic conditions. This dissertation provides comprehensive studies on novel thermoelectric compositions and nanocomposites that are suitable for manufacturing of high temperature modules. Microstructural architectures proposed here provide the ability to tailor electronic transport and phonon scattering beyond the commonly demonstrated regimes. Optimized materials were

successfully implemented in efficient and stable thermoelectric generator exhibiting power density on the order of 13.81 $W \cdot cm^{-2}$, which is 1400 % higher than that of the fuel cell (~1 $W \cdot cm^{-2}$).

Acknowledgements

The first lesson from starting a doctoral program in materials science is that no single person can study all field of science and engineering, and networking and collaboration are very important to achieve academic success in effective and efficient way. Fortunately, I have been able to have good collaborators and supporters during my research so that I can make good results and successfully complete my work. Here I would like to dedicate this to all those who have help me to do this research and share joys and sorrows of life during the Ph.D. program.

First of all, I would like to express my sincere gratitude to my advisor, Dr. Shashank Priya for his great guidance during my Ph.D. course. He provided me appropriate advice and full support on my research and encouraged me whenever I have been faced with difficulties in my work. His deep and wide knowledge in science has helped a lot to overcome many challenges. I was deeply inspired by his great passion and broad vision in research, extensive network and collaboration in worldwide, and amazing management and communication skills. It was a great honor for me to work with him.

I am thankful to my committee members, Dr. Alex O. Aning, Dr. Mitsuhiro Murayama, and Dr. Giti Khodaparast for their great advice to make better quality of research. Dr. Aning gave me great discussion on processing of metal alloys. Dr. Murayama guided me to make a solid research plan for my Ph.D. program and helped me a lot to analyze microstructures of materials by his expertise with a transmission electron microscope. Dr. Khodaparast has always provided positive feedbacks and warm encouragements on my work. She and Dr. Brenden A Magill were also good collaborators for my another research topic on magnetoelectric thin films.

I would like to express to my special thanks to my thermal group members: Dr. Bed poudel, Dr. Wenjie Li, Dr. Amin Nozariasbmaz, and Dr. Udara Saparamadu. I might not be able to perfectly finish my work and achieve high quality of research without their incredible support and encouragement. It has been a great pleasure working with them.

I would like to extend my gratitude to DARPA MATRIX thermoelectric team, Dr. Heonjoong Lee, Dr. Myung-Eun Song, Dr. Jeff Sharp, Dr. David Stokes, Dr. Matthew Pearson, Dr. Mercouri Kanatzidis, Dr. Sumantar Sarkar, Dr. Gangjian Tan, Dr. Scott Huxtable, and Dr. Jue Wang. It was an amazing team, and collaboration with them makes it possible to create high quality products in a short period of time. I am also grateful to Dr. Jean. J. Heremans and Adbhut Gupta for their help on Hall effect measurement to investigate the electrical transport in nanocomposites. I would like to thank Dr. Christopher Winkler, Stephen McCartney, and Donald Leber who gave me training session on material characterization tools and clean room nanofabrication.

I would like to express my sincere thanks to all the colleagues in our group for their great help and tight friendship: Dr. Min-Gyu Kang, Dr. Chan Su Han, Dr. Congcong Wu, Dr. Yongke Yan, Dr. Kai Wang, Dr. Xiaotian Li, Dr. Hairui Liu, Dr. Dong Yang, Dr. Rammohan Sriramdas, Dr. Haribabu Palneedi, Dr. Yuanyuan Jiang, Dr. Heon-Cheol Song, Dr. Jinsung Chun, Dr. Deepam Maurya, Dr. Xiaojia Zheng, Dr. Deepa Singh, Dr. Sreenivasulu Gollapudi, Dr. Nathan Sharpes, Dr. Bo Chen, Dr. Shikhar Jha, Dr. Yang Qiang, Dr. Prashant Kumar, Dr. Jiayong Gan, Dr. Ravi Kishore, Dr. Gregory Krummel, Dr. Anthony Jon Garcia, Hyeon Lee, Ricardo Cruz, Colin Stewart, Haoyang Leng, and Yuchen Hou. I also want to thank all my friends in Blacksburg and my hometown. All the

happy memories sharing with them gave me work-life balance and replenished energy to go on.

I gratefully acknowledge financial supports from DARPA MATRIX program, AFOSR, and Center for Energy Harvesting Materials and Systems. In addition, I would like to thank Lauren Mills, Kim Grandstaff, Amanda Stowers McCoy, Jennifer Jordan, and Jennifer Leedy for their technical support and advice on Ph.D. program. They have provided the best resources with useful information and assisted me to focus on my research.

Most of all, I would like to express my greatest gratitude to my parents, Cheol-Ho Kang and Li-won Kim for their unconditional love, wholehearted support and encouragement. Their love has been the most powerful spur and energy to pursue the Ph.D. degree and study in the United States. I also sincerely appreciate to my older brother, Hanbit Kang for his love and devotion. He is my rock and my best friend whom I can really open up myself. With the love and support of my family, I was able to devote my life to academic study and get over tough times in my long journey. At the last moment of this long journey, I want to tell my family that I love you and thank you so much.

Han Byul

Aug. 2019

Table of Contents

List of Figures

List of Tables

Chapter 1 Introduction

A rapid increase in global energy demand and greenhouse-gas emissions has turned the spotlight on energy efficiency and waste energy recovery. It is well-known [1-3] that a substantial portion (20-50 %) of the energy is lost as waste heat, resulting in total loss of 5 to 13 quadrillion Btu/yr [4] across US industry. According to Forman's estimation, the fraction of work potential (Carnot potential) for global heat lost with hot-side temperature above 373 K is 79% and more than 55% waste heat has medium to high hot-side temperature of >573 K [5]. The Carnot efficiency of the system (theoretical maximum for converting thermal energy into useful work) increases with hot-side temperature. This indicates the importance of developing waste heat recovery mechanisms that can operate over wide temperature ranges and provide easy integration with variety of industrial processes. In this respect, thermoelectric (TE) energy harvesting is promising as it can provide wide temperature operation through casacading. Further, thermoelectric modules provide solid-state noiseless operation which is relevant for generator applications.

In order to harvest the high-quality waste heat at elevated temperatures using TEs, it is vital that the TE material has good thermal stability as well as high figure-of-merit (zT) over the entire range of operating temperatures. Half-Heusler (hH) compounds are an important class of TE materials for moderate to high temperature applications due to their excellent mechanical strength and in-air thermal stability [6]. Half-Heusler alloys have potential for mass-scale thermoelectric power generation where not only high output power density but also high mechanical stability and sustainability under repetitive thermal cycling is required. Most widely studied *n*-type MNiSn and *p*-type MCoSb (M = Hf, Zr, and Ti) alloys show much higher hardness (~10 and ~13 GPa) and elastic modulus (~190 and ~220 GPa) compared to that of other TE materials [7,8]. Further, a relatively small difference of coefficient of thermal expansion (CTE) between *n*- and *p*-type hH is

beneficial towards long-term durability of TE modules [7]. The commonly used hH alloys exhibit excellent electrical transport properties as a result of sharp slope of the density of states (DOS) near the Fermi level and the narrow band gap (0.1-1.1 eV) [9,10]. However, relatively high thermal conductivity (7-17 $W \cdot m^{-1}K^{-1}$ at 300 K) of hH alloys limits their zT. The magnitude of thermal conductivity is related to electronic and lattice transport [11]. Various strategies have been developed to effectively reduce the lattice thermal conductivity, such as introducing alloy scattering with additional mass or strain fluctuation [12-14] and enhancing phonon scattering by nanostructuring [15-18].

This thesis demonstrates high TE performance hH alloys through control of processing and microstructural parameters ranging from nanostructuring to sintering conditions. Novel material design is introduced based upon multi-scale structural modification with multi-phase intrinsic and extrinsic metallic nanoinclusions. The high temperature thermal stability of the hH alloys is investigated by monitoring TE property variation during the high temperature heat treatment in air. Based upon the optimized half-Heusler TE alloys, high performance hH thermoelectric generator (TEG) is demonstrated with sustainable operation under high temperature heat cycling in air.

This chapter will provide fundamental theory of thermoelectrics, current challenges in TEs, and our strategies for improving both material performance and thermal stability in order to realize a high output performance TEG module.

1.1 Thermoelectric effect

The thermoelectric effect implies conversion of temperature difference across a material couple to be directly converted into an electric voltage and vice-versa. It is thermodynamically reversible effect in contrast to an irreversible Joule heating (I^2R) that always occurs as a result of

current flow in a resistive material. TE phenomenon comprises of three separate effects: Seebeck effect, Peltier effect and Thomson effect.

1.1.1 Seebeck effect

If two different conductors are connected electrically in series and thermally in parallel and one end of the junction (A) is maintained at higher temperature as compared to other junction (B) as shown in **Figure 1a**, then an electromotive force (V) is created across the junction that is proportional to the temperature gradient. The relationship between the temperature difference (ΔT) and the electric field (ΔV) is called as Seebeck effect and is described as:

$$S_{AB} = S_A - S_B = \frac{\Delta V}{\Delta T} \tag{1.1}$$

where S is the Seebeck coefficient of material (also called as thermopower). This effect has long been used in a thermocouple for sensitive, accurate, and reliable temperature measurements (or controls). This effect is being utilized for power generation to convert heat flux into electricity by forming thermoelectric circuit comprising of two different thermoelectric materials (*n*-doped and *p*-doped semiconductor) as illustrated in **Figure 1b**.

1.1.2 Peltier effect

Peltier effect implies creation of heat when electric current (I) is passed through a junction between two dissimilar conductors (**Fig. 1a**). The magnitude and direction of the generated heat (Q) is dependent on the current flow (I), given as:

$$Q_{Peltier} = \Pi_{AB} \cdot I = (\Pi_A - \Pi_B) \cdot I \tag{1.2}$$

Here Π is the Peltier coefficient which represents how much heat is produced per unit charge, and Π_A and Π_B are the coefficients of conductors A and B. **Figure 1c** shows one of the application of Peltier effect as thermoelectric refrigerator that can cool objects without any moving parts or circulating liquid.

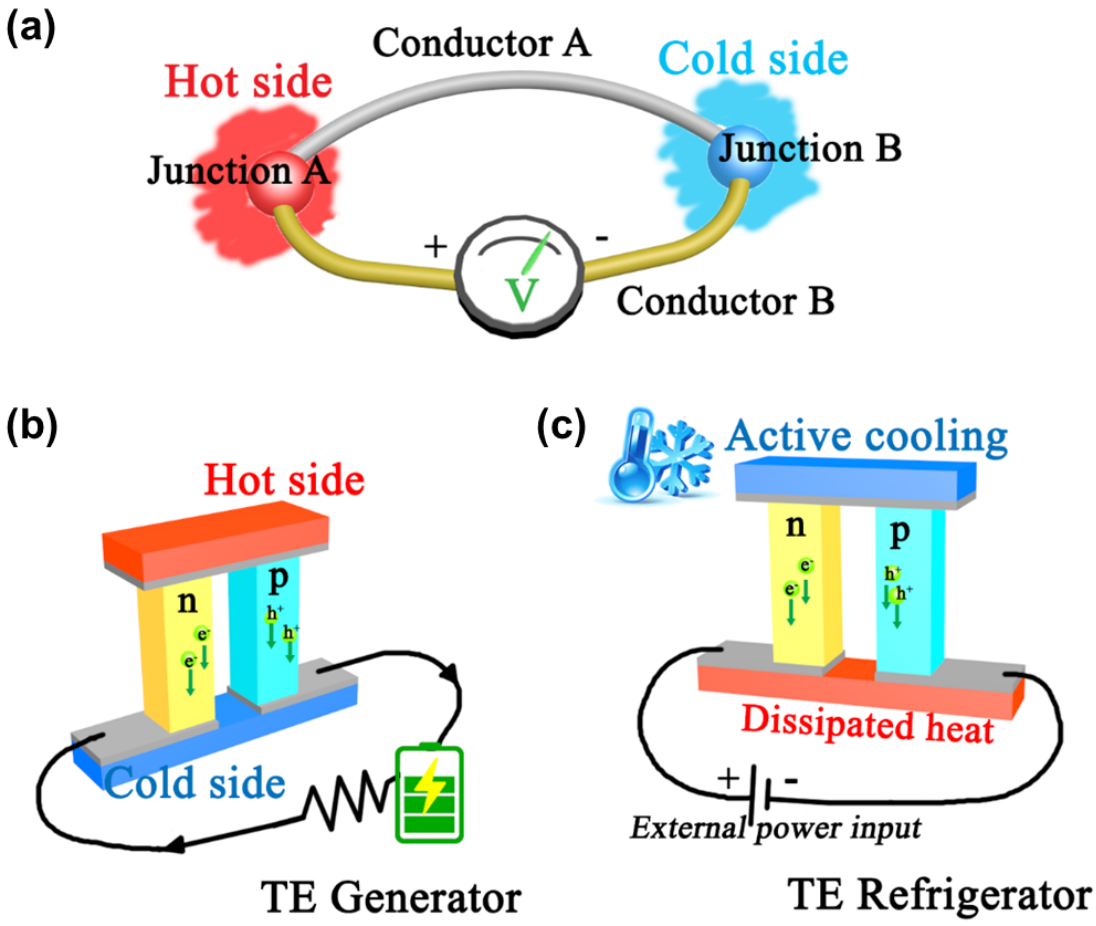

Figure 1.1 Schematic illustrations of (a) Seebeck effect and Peltier effect, (b) thermoelectric generator, (c) thermoelectric refrigerator.

1.1.3 Thomson effect

Thomson effect indicates the heating or cooling of a single current-carrying conductor depending upon the relative direction to temperature gradient. When a current (I) is passed through

a homogeneous conductor placed across a temperature difference (ΔT), Thomson heat ($Q_{Thomson}$) is generated in proportion to both the current and the temperature gradient. It can be described as

$$Q_{Thomson} = \tau \cdot I \cdot \Delta T \tag{1.3}$$

where τ is the Thomson coefficient.

1.1.4 Kelvin (or Thomson) relationships

In 1854, Lord Kelvin (William Thomson) discovered two relationships between the three thermoelectric effects based on fundamental thermodynamics. The first Kelvin relation is given as:

$$\tau = T \cdot \frac{dS}{dT} \tag{1.4}$$

where T is the absolute temperature of the material. It represents relation between the Seebeck coefficient and Thomson coefficient. The second Kelvin relation provides expression of the Peltier coefficient in terms of the Seebeck coefficient as:

$$\Pi = T \cdot S \tag{1.5}$$

These relationships have been experimentally proven in many thermoelectric materials.

1.2 Thermoelectric parameters

TE effects are related to charge or heat carrier transport in a material by external heat or power source. There are several physical properties that contribute to thermal and electrical transport. Thus, it is necessary to understand the interrelationship between these properties along with the individual characteristics to quantitatively explain the thermoelectric effects.

1.2.1 Electrical conductivity

Electrical conduction is the transport of electric charges in a material resulting from an applied electric field. In a classical theory, the electrical conductivity in a solid can be written using Drude model as:

$$\sigma = ne\mu = \frac{ne^2\tau}{m^*} \tag{1.6}$$

where n is carrier concentration, e is electron charge, μ (=eτ/m*) is carrier mobility, m^* is effective mass, and τ is relaxation time.

In quantum mechanics, the flow of electrons in a solid can be described by the Boltzmann transport equation [19]. If we assume that it has a constant relaxation time (τ) and isotropic parabolic energy band, the electrical conductivity can be simplified as:

$$\sigma = \frac{2e^2\tau}{m^*}\left(\frac{m^* k_B T}{2\pi h^2}\right)^{3/2} exp\left(\frac{-|E_F|}{k_B T}\right) \tag{1.7}$$

$$n = 2\left(\frac{m^* k_B T}{2\pi \hbar^2}\right)^{3/2} exp\left(\frac{-|E_F|}{k_B T}\right) \tag{1.8}$$

here k_B is Boltzmann constant, $\hbar$ is Planck's constant, and E_F is the Fermi energy of the system.

1.2.2 Seebeck coefficient

As discussed in 1.1.1, the magnitude of the Seebeck effect is evaluated in terms of Seebeck coefficient (S), defined as the potential difference created per unit temperature difference (Equation 1.1). For metals or heavily doped semiconductors, the Seebeck coefficient can be given by Mott formula as following [20]:

$$S = \frac{\pi^3}{3}\frac{k_B^2 T}{e}\frac{\partial ln\sigma}{\partial E}\Big|_{E=E_F} \tag{1.9}$$

The Mott relation provides the interrelationship between the Seebeck coefficient and the electrical conductivity. It can be further simplified by assuming a parabolic band structure along with energy-independent scattering approximation [21,22] as following:

$$S = \frac{8\pi^2 k_B^2}{3eh^2} m^* T \left(\frac{\pi}{3n}\right)^{2/3} \tag{1.10}$$

This simplified equation indicates that larger effective mass and lower carrier concentration will contribute to the higher Seebeck coefficient.

1.2.3 Thermal conductivity

The heat transport in materials occurs through charge carriers and lattice vibrations (phonons). For metals and semiconductors, the overall thermal conductivity can be expressed as the summation of two independent terms:

$$\kappa = \kappa_e + \kappa_l \tag{1.11}$$

where κ_e is the electronic contribution and κ_l is the phonon contribution to thermal conductivity.

Most of the electronic thermal conductivity is directly related to the electrical conductivity by the Wiedemann-Franz law [23]:

$$\kappa_e = L\sigma T = Lne\mu T \tag{1.12}$$

where L is the Lorenz number, which is defined as the ratio $\kappa_e/\sigma T$. For metals or degenerate semiconductors, it is given as:

$$L = \frac{\pi^2}{3}\left(\frac{k_B}{e}\right)^2 = 2.44 \times 10^{-8} \mathrm{W} \cdot \Omega \cdot \mathrm{K}^{-2} \tag{1.13}$$

Non-degenerate semiconductors have a significant deviation from the degenerate limit number (2.44×10^{-8} $\mathrm{W}\cdot\Omega\cdot\mathrm{K}^{-2}$) when they exhibit alternative scattering mechanisms rather than acoustic

phonons or non-parabolic band structures. Kim *et al.* [24] suggested a simple equation for the Lorenz number given as:

$$L = 1.5 + \exp\left[-\frac{|S|}{116}\right] \tag{1.14}$$

Experimentally measured Seebeck coefficient (*S*) can be applied in the calculation to estimate the Lorenz number.

1.2.4 Lattice thermal conductivity

Another important heat transport mechanism involves lattice vibrations. In a solid, atoms are bonded to each other and thus atomic vibrations are coupled. This introduces waves corresponding to the cooperative vibrations of many atoms that identically oscillate at a single frequency. This is called as "phonon" and it plays a major role in the heat and charge transport. The thermal conductivity due to phonons (κ_l) is proportional to the mean velocity (ν_{ph}) and the mean free path of phonons (l_{ph}), and is given as:

$$\kappa_l = \frac{1}{3} C_v \nu_{ph} l_{ph} \tag{1.15}$$

where C_v is the specific heat capacity at constant volume.

The phonon waves can interact with other phonons or get scattered by the defects, impurities, or crystal boundaries while traveling through the material. The traveling distance (or path) of phonons is determined by these scattering events, and can be defined as:

$$l_{ph} = \nu_{ph} \tau \tag{1.16}$$

where τ is the phonon relaxation time for different types of scattering mechanisms such as phonon-phonon scattering (Umklapp), phonon-impurity scattering, phonon-boundary scattering, and

phonon-electron scattering. Each scattering mechanism can be defined by a relaxation rate ($1/\tau$) and the overall scattering process can be expressed using Matthiessen's rule as:

$$\frac{1}{\tau} = \frac{1}{\tau_U} + \frac{1}{\tau_M} + \frac{1}{\tau_B} + \frac{1}{\tau_{ph-e}} \tag{1.17}$$

where τ_U is Umklapp phonon-phonon scattering, τ_M is phonon-impurity scattering, τ_B is phonon-boundary scattering, and $\tau_{ph\text{-}e}$ is phonon-electron scattering, respectively.

1.2.5 Figure of merit (zT)

By considering all the parameters and their relationships that contribute to the thermoelectric effects, the thermoelectric performance is generally described by dimensionless figure of merit (zT) as:

$$zT = \frac{\sigma S^2}{\kappa} T \tag{1.18}$$

where σ, *S*, *T*, and κ are the electrical conductivity, Seebeck coefficient, absolute temperature (Kelvin), and thermal conductivity, respectively. Here, the electronic transport, $S^2\sigma$, is called as power factor, representing capability of a material for power generation at a given temperature. The figure of merit, zT, indicates that higher electrical conductivity and Seebeck coefficient are preferable along with lower thermal conductivity to maximize zT. However, that is challenging because these properties are strongly coupled with each other. **Figure 1.2** displays a carrier concentration dependence of thermoelectric parameters. For example, electrical conductivity and thermal conductivity are simultaneously increased by increasing carrier concentration. On the other hand, the higher carrier concentration leads to decrease of Seebeck coefficient. Therefore, there exists an optimum point in both power factor (*PF*, $S^2\sigma$) and zT. The optimum carrier

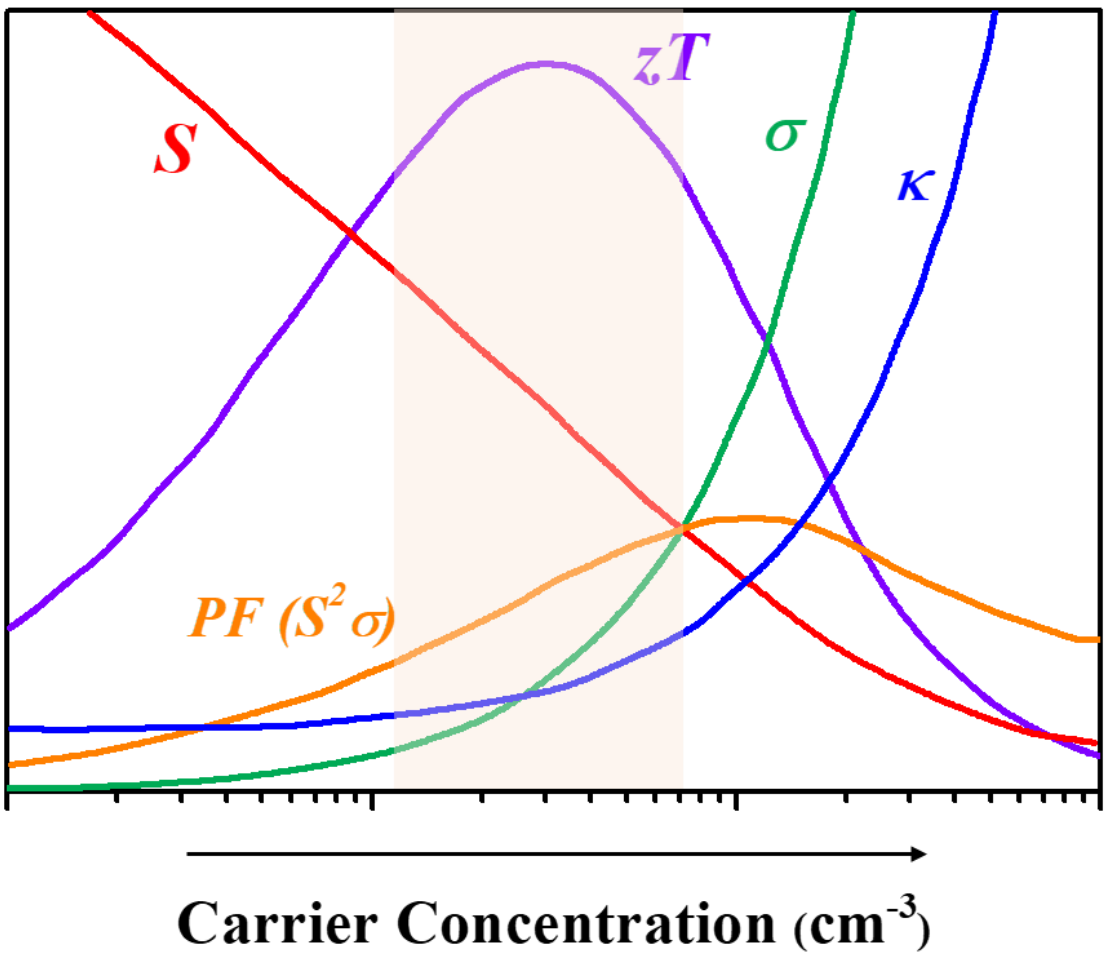

Figure 1.2 Schematic plots of TE properties as a function of carrier concentration [22].

concentration of thermoelectric materials is normally on the order of 10^{19}~10^{21} cm^{-3}, which is range for heavily-doped semiconductors.

The figure of merit for different TE materials exhibits distinct temperature dependence as shown in **Figure 1.3**. Typical TE materials used in demonstrations are Bi_2Te_3 [25,26], PbTe [27], Skutterudite [28,29], half-Heusler [30,31], and SiGe alloys [32,33]. Interestingly, each TE material exhibits the specific temperature region where zT is maximized. For example, Bi_2Te_3 alloy displays highest zT around 376 K while the zT of SiGe alloy is maximized at higher temperature of 1173 K.

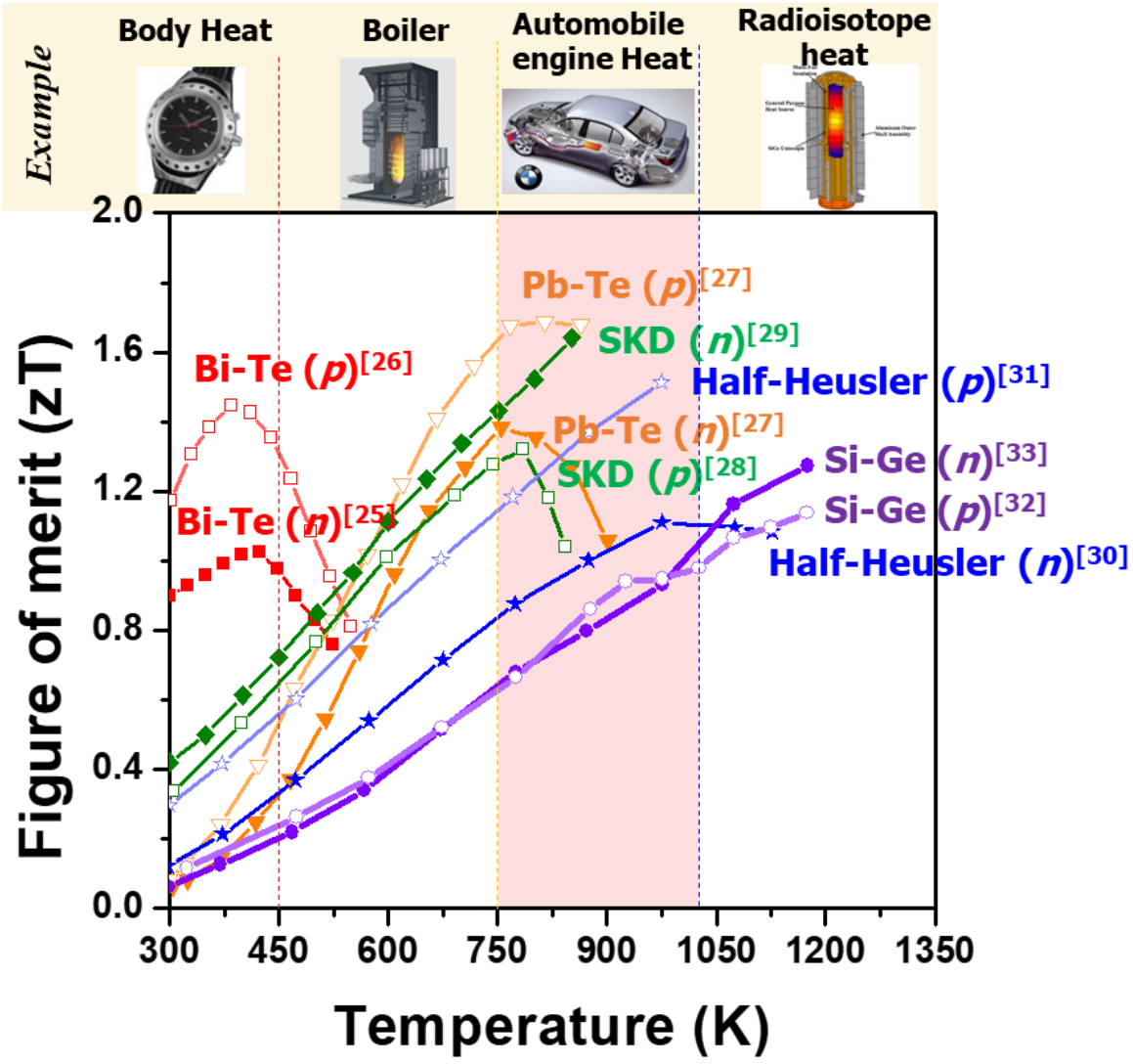

Figure 1.3 Temperature dependence of figure of merit for different thermoelectric materials [25-33].

Therefore, it is important to carefully select a proper TE material according to the temperature region and application as shown in **Figure 1.3**. Here, it can be noted that half-Heusler alloy shows excellent TE performance in the range of 750 to 973 K (marked as red) as compared to other TE materials. This indicates its great potential and advantage in use for medium and high temperature energy harvesting application.

1.3 Thermoelectric generator and conversion efficiency

Thermoelectric energy harvesting has been gaining interest as a promising mechanism for power generation from wasted heat. The thermal power generation device based on TE materials is called as thermoelectric generator (TEG). In general, the TEG consists of *p*-type and *n*-type thermoelectric semiconductor connected electrically in series and thermally in parallel as shown in **Figure 1.4**. When a temperature gradient is applied to the TE materials, an electrical field is developed across the TE legs and current flows through *n*- and *p*-type legs to external circuit through metallic electrodes. Normally, a large number of pairs of *n*- and *p*-type TE semiconductors (couples) are arrayed on an insulator plate. One side of the legs contacts the heat source while the other to a sink to create temperature gradient into the TE material.

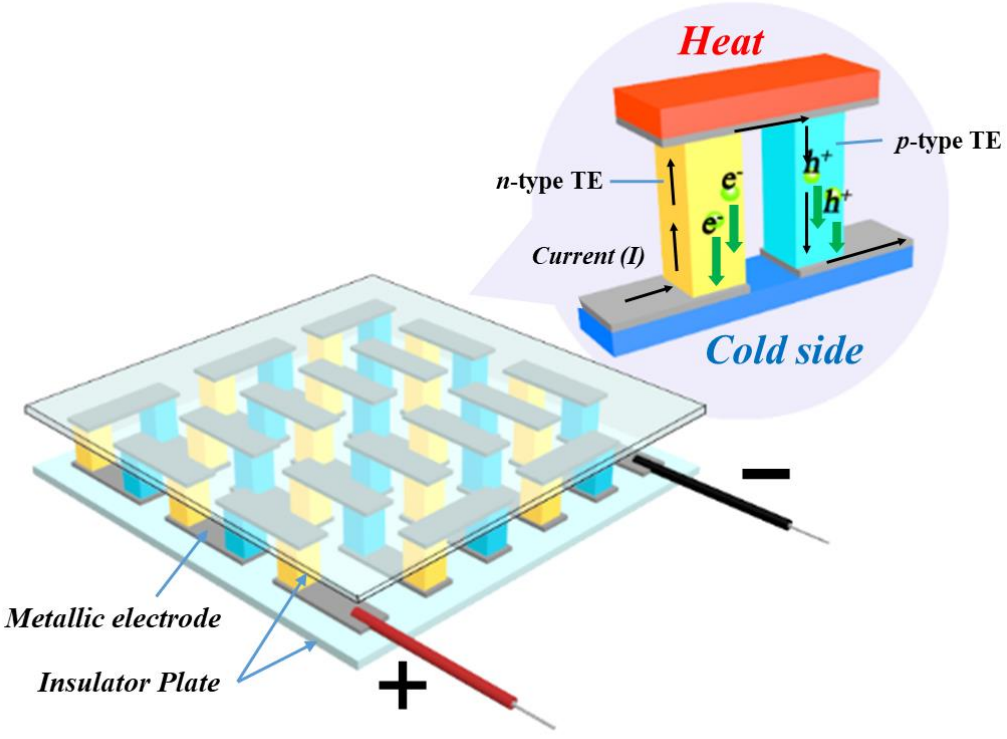

Figure 1.4 Schematic illustration of TEG module and the detailed structure of individual uni-couple in the module.

The conversion efficiency of the TE power generator is defined as:

$$\eta = \frac{T_h - T_c}{T_h} \frac{\sqrt{1+ZT}-1}{\sqrt{1+ZT}+T_c/T_h} \tag{1.19}$$

where T_h is the hot side temperature, T_c is the cold side temperature, and ZT is the average figure of merit for TE materials. The equation implies that higher conversion efficiency of TEG is attributed to both higher material average figure of merit and larger temperature difference between hot and cold side. **Figure 1.5** shows the theoretical calculations for TEG conversion efficiency (η) as a function of the hot side temperature (T_h) and the average figure of merit zT for TE materials while holding the cold side temperature (T_c) as constant at 373 K. It is obvious that higher hot side temperature increases the conversion efficiency and the material zT improvement leads to further enhancement in efficiency. A TEG device with an average ZT of 2.0 can convert thermal energy into electricity with 20% efficiency at hot side temperature of 1000 K.

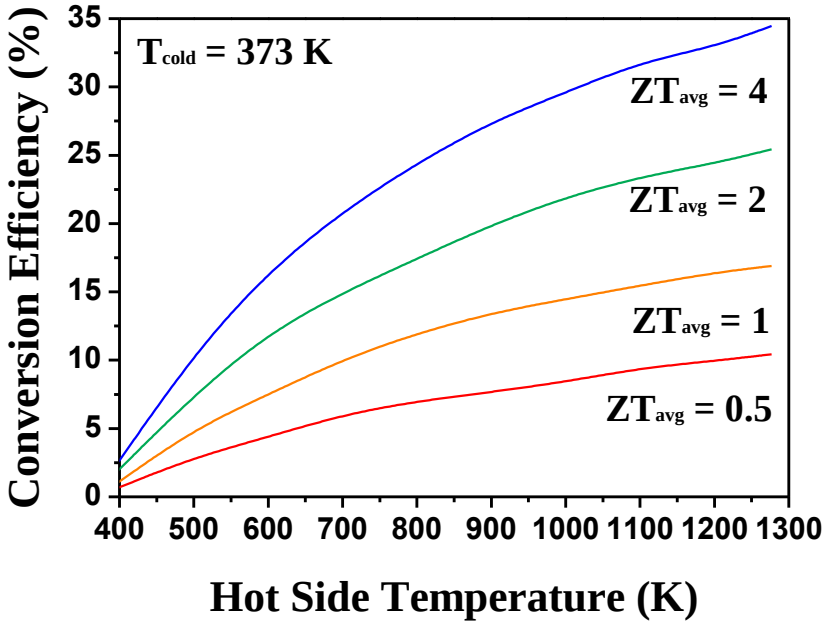

Figure 1.5 Theoretical TEG conversion efficiency as a function of hot side temperature and material's average figure of merit (ZT) [34].

1.4 Half-Heusler alloy

In 1903, *Friedrich Heusler* discovered magnetic intermetallic compound, Cu_2MnSn, and revealed strong ferromagnetic property in this material system [35]. These compounds, termed as "Heusler compound", comprise of ternary intermetallic face-centered cubic (*fcc*) sublattice structures with a composition of A_2BX, where A and B are transition metals and X is in the *p*-block. Half-Heusler alloys have one vacant *fcc* sublattice within three interpenetrating *fcc* sublattice structure, corresponding to a general formula of ABX as shown in **Figure 1.6**. This material can have a wide range of bandgap from 0.1 eV to 3.7 eV depending upon the occupancy of the elements. For thermoelectric application, narrow bandgap (0.1-1.1 eV) compounds are generally used with 18 valence electron count (VEC) per unit cell. All three positions (X, A, and B) in the crystal structure can be doped by other elements to change VEC for hH alloys as represented in **Figure 1.6**. Most widely studied compounds are *n*-type MNiSn and *p*-type MCoSb compounds (M = Hf, Zr, and Ti) that exhibit high Seebeck coefficient of above ~200 μV/K at room temperature in the undoped condition [11,36]. This is related to the sharp feature of the carrier density of state (DOE) near the Fermi energy (higher $\frac{dn(E)}{dE}$) from *d*-band of nickel or cobalt [6,9,37,38].

Despite the high power factor ($S^2\sigma$), a relatively high thermal conductivity has been a bottleneck in achieving high figure of merit in half-Heusler system compared to other TE materials. The thermal conductivity of the typical TE materials are listed in **Table 1.1** [17,26,28,39-42]. The thermal conductivity of half-Heusler alloy is more than double of that other TE materials. A predominant contribution to the high thermal conductivity is related to the higher lattice thermal conductivity. The lattice thermal conductivity can be separately controlled

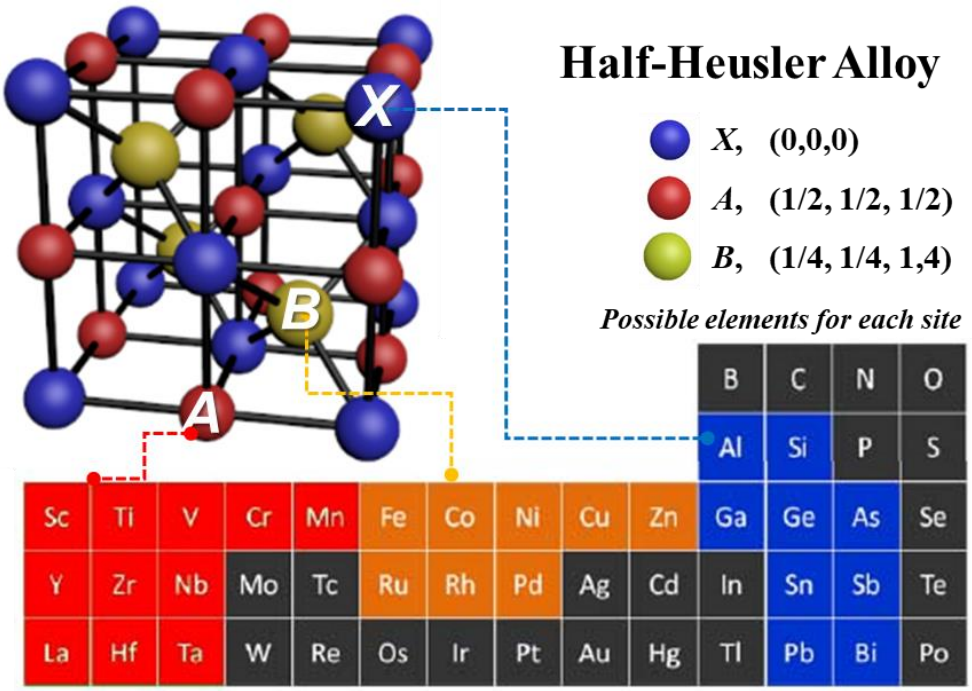

Figure 1.6 Schematic illustration of XAB half-Heusler crystal structure and potential elements that occupy each site [43].

from that of electrical charge transport through promotion of phonon scattering. Enhancing the phonon scattering to reduce the lattice thermal conductivity is one of the most effective pathways in half-Heusler systems.

Table 1.1 A comparison of thermal conductivity and lattice thermal conductivity in TE materials

Materials	Thermal Conductivity (W/m·K)	Lattice Thermal conductivity (W/m·K)
Half-Heusler [17]	5~6	2.5~3.5
Skutterudite [28]	2.0~3.5	1.2~2.0
PbTe [41,42]	1.0~3.0	0.8~1.5
SiGe [39,40]	2.0~3.0	1.5~2.0
$Bi_{0.5}Sb_{1.5}Te_3$ [26]	0.8~1.2	0.3~0.6

1.5 Review on state-of-the-art half-Heusler thermoelectric materials

Figure 1.7 reviews the state-of-the-art zT reported for *n*- and *p*-type half-Heusler alloys in literature [16,30,31,44-51]. **Table 1.2** provides more details on composition, maximum and average zT, and processing strategy. As shown in **Figure 1.7b**, new composition development in *p*-type hH led to significant advancement of thermoelectric performance. As a result, *p*-type hH alloys show higher zT than that of *n*-type. Various approaches and strategies have been applied to control physical properties of hH compounds for improving zT [16,30,31,44-51]. Many of the earlier studies have mainly focused on compositional optimization [11,30,36,52-60]. As discussed in *section 1.2.5*, thermoelectric properties are very sensitive to the carrier concentration and band structure. Half-Heusler structure has excellent variability in terms of doping or substitution of elements because all three atomic positions can be doped by either single or multiple dopants on multiple sites as discussed in *section 1.4* [6,61]. For example, Rausch *et al.* [49] demonstrated effective tuning of TE properties in (Ti/Zr/Hf)$CoSb_{1-x}Sn_x$ system through carrier concentration optimization and phase separation by controlling Sn-doping and Ti/Hf ratio. M-site substitution strategy has been presented in *n*-type MNiSn system [44,46]. Another effective method to achieve higher zT is by enhancing phonon scattering through nanostructures. The nanostructuring approach [16,17] for suppressing thermal conductivity in both *n*-type MNiSn and *p*-type MCoSb system is similar to microstructural studies conducted on other TE materials [26,39,40]. Recently, new *p*-type hH compositions have been investigated based on the theoretical prediction of their high band degeneracy [31,48,50,51,62,63]. These new compositions have shown promising TE performance as described in **Figure 1.7** and **Table 1.2**.

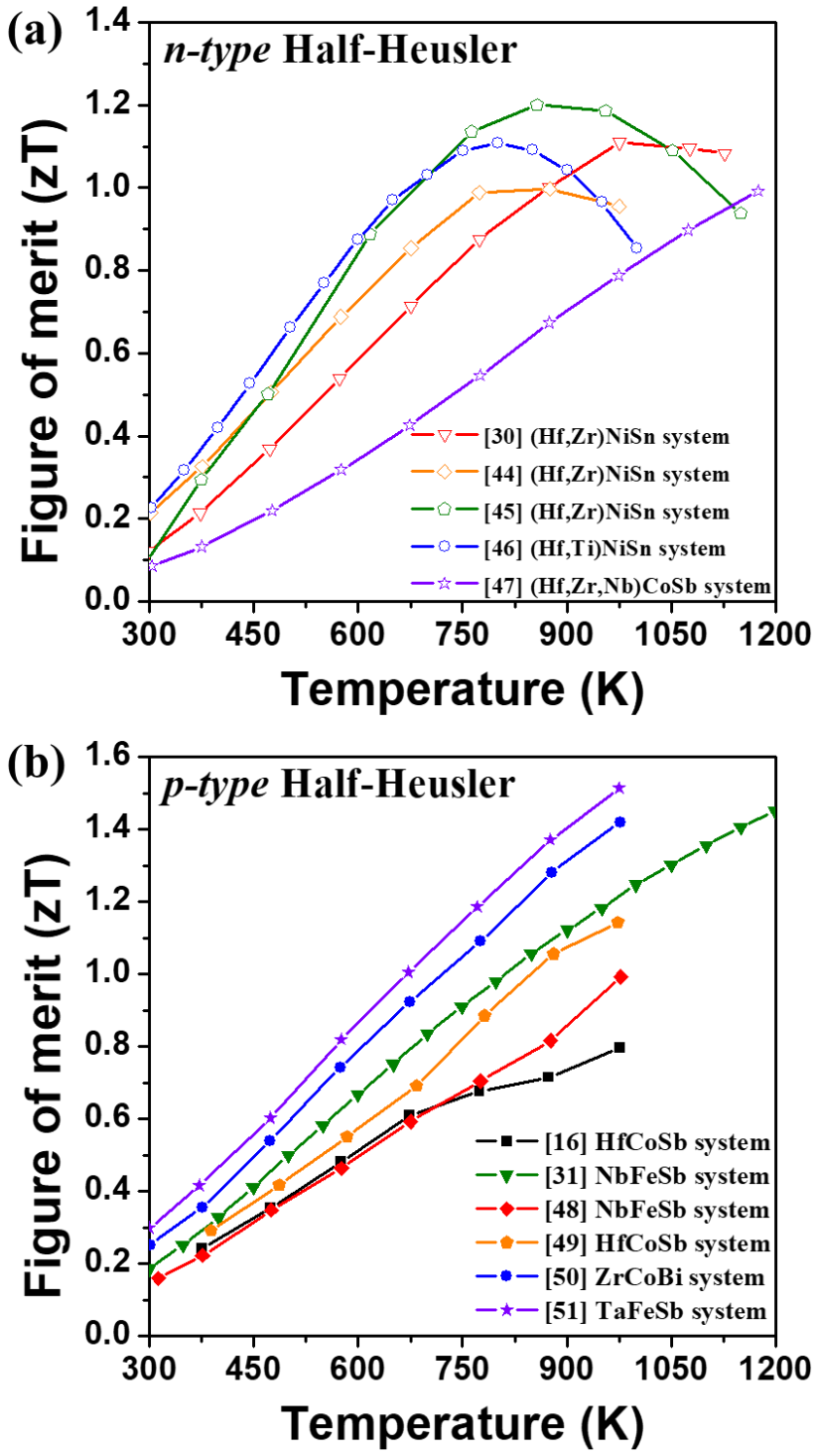

Figure 1.7 State-of-the-art for figure of merit (zT) based on the results published in literature for (a) *n*-type [30,44-47] and (b) *p*-type hH compounds [16,31,48-51]. More detailed information is provided in Table 1.2.

Table 1.2 Summary of the TE performance for the *n*-type and *p*-type half-Heusler alloys based upon the literature [16,30,31,44-51]

#	Composition	Type	zT_{max} (Temp/K)	zT_{avg} (Temp/K)	Major Process	Ref.
1	$Zr_{0.2}Hf_{0.8}NiSn_{0.985}Sb_{0.015}$	*n*	**1.1** (1000)	**0.651** (300-1000)	Composition Optimization	[30]
2	$Hf_{0.25}Zr_{0.75}NiSn_{0.99}Sb_{0.01}$	*n*	**1.0** (973)	**0.722** (300-1000)	Stronger point defect scattering by Hf substitution	[44]
3	$Hf_{0.6}Zr_{0.4}NiSn_{0.995}Sb_{0.005}$	*n*	**1.2** (850)	**0.822** (300-1000)	Annealing near melting point	[45]
4	$Ti_{0.5}Hf_{0.5}NiSn_{0.98}Sb_{0.02}$	*n*	**1.1** (800)	**0.797** (300-1000)	Atomic scale defect disorder by Ti-substitution on Hf site	[46]
5	$(Zr_{0.4}Hf_{0.6})Nb_{0.12}CoSb$	*n*	**0.99** (1173)	**0.419** (300-1000)	Lanthanide contraction using Nb substitution	[47]
6	$Zr_{0.5}Hf_{0.5}CoSb_{0.8}Sn_{0.2}$	*p*	**0.8** (973)	**0.55** (300-973)	Nanostructuring	[16]
7	$FeNb_{0.88}Hf_{0.12}Sb$	*p*	**1.4** (1200)	**0.8** (300-1200)	Selecting heavier dopant of Hf, Optimized PF and reduced $\kappa_{lattice}$	[31]
8	$Nb_{0.6}Ti_{0.4}FeSb_{0.95}Sn_{0.05}$	*p*	**1.0** (973)	**0.53** (300-973)	Composition Optimization	[48]
9	$Ti_{0.25}Hf_{0.75}CoSb_{0.85}Sn_{0.15}$	*p*	**1.2** (973)	**0.72** (400-973)	Composition Optimization Phase separation	[49]
10	$ZrCoBi_{0.65}Sb_{0.15}Sn_{0.20}$	*p*	**1.42** (973)	**0.81** (300-973)	High band degeneracy in conjunction with a lowest mean sound velocity	[50]
11	$Ta_{0.74}V_{0.1}Ti_{0.16}FeSb$	*p*	**1.52** (973)	**0.93** (300-973)	High band degeneracy, strong point defect scattering	[51]

1.6 Objectives and outline

There has been extensive development of TE materials which has resulted in strong and growing demand for practical TE devices. However, the implementation of realistic devices has been lagging as compared to the material development for reasons such as: (i) lack of study on material's

stability under realistic operating condition, (ii) complexity in achieving very low contact resistance on the order of few $\mu\Omega \cdot cm^2$ level, and (iii) challenges in fabricating sustainable and reliable TEG legs exhibiting robust mechanical and thermal strength as well as good matching of thermal expansion coefficient between *p*- and *n*-type legs. This dissertation addresses all these challenges and provides fundamental insight into design of both TE material and modules based upon half-Heusler alloys.

Systematic material optimization process for both *n*-type and *p*-type hH alloys is discussed in *chapter 3 and 4* with baseline of the materials and the synthesis approaches. Using the optimized synthesis conditions and material compositions, novel multi-phase nanocomposite was developed with a record high zT of ~1.4 in *n*-type hH compound. The exceptional TE performance of newly developed materials and underlying mechanisms providing these high responses will be discussed in *chapter 5*. In order to design and implement TEG device, thermal oxidation behavior and stability of the developed TE compounds was studied at high temperatures in air. *Chapter 6* will provide results on implementation of the hH materials in high temperature applications. Lastly in *chapter 7*, high efficiency uni-couple thermoelectric generator (TEG) module is fabricated using developed half-Heusler materials. The uni-couple TEG device showed outstanding conversion efficiency of ~10.7 % and power density of ~13.93 $W \cdot cm^{-2}$ under the temperature difference of 674 K. We believe that this dissertation covering materials to practical devices can provide fundamental guidance for design of both high performance TE materials and modules.

Chapter 2 Experimental and characterization

2.1 Sample preparation

$(Hf_{0.6}Zr_{0.4})NiSn_{0.99}Sb_{0.01}$, $(Hf_{0.5}Zr_{0.5})_{1-x}Ti_xCoSb_{1-y}Sn_y$ (x = 0.0, 0.1, 0.2, and y = 0.10, 0.15, 0.20, 0.25) and $(Nb_{0.6}Ti_{0.4})FeSb_{0.95}Sn_{0.05}$ compositions were synthesized using radio-frequency (RF) induction melting under an argon atmosphere for 5 minutes. Stoichiometric amounts of high purity metal precursors of hafnium piece (99.9%, Alfa Aesar), zirconium slug (99.9%, Alfa Aesar), nickel slug (99.995%, Alfa Aesar), titanium slug (99.995%, Alfa Aesar), niobium slug (99.95%, Alfa Aesar), iron slug (99.95%), antimony shot (99.999%, Alfa Aesar), and tin wire (99.95%, Alfa Aesar) were mixed to obtain the desired compositions. The ingots were rotated and re-melted several times to ensure homogeneity. The resulting ingots were pulverized and transferred in a stainless steel container with grinding balls under an argon environment in a glove box. Mechanical milling was conducted for 4 hours using SPEX mixer/mill (Model 8000D, SPEX SamplePrep, Metuchen, NJ). In order to synthesize multi-phase nanocomposite in *n*-type hH compounds, the grinded *n*-type $(Hf_{0.6}Zr_{0.4})NiSn_{0.99}Sb_{0.01}$ powders were mixed in three different amounts (x = 2, 5, and 10 wt%) with tungsten nanoparticles (99.7%, Sky Spring Nanomaterials) by using SPEX mixer/mill. The mixed powders were consolidated by Spark Plasma Sintering (SPS, Model Dr. Sinter-625V, Fuji, Japan) at three different temperatures of 1223, 1323, and 1423 K under a pressure of 80 MPa for 5 minutes, yielding fully dense pellets. **Figure 2.1** briefly summarizes the flowchart for half-Heusler alloy synthesis. The sintered pellets were cut in the shape of a bar and disk for a ZEM-3 and laser flash thermal diffusivity measurement, respectively.

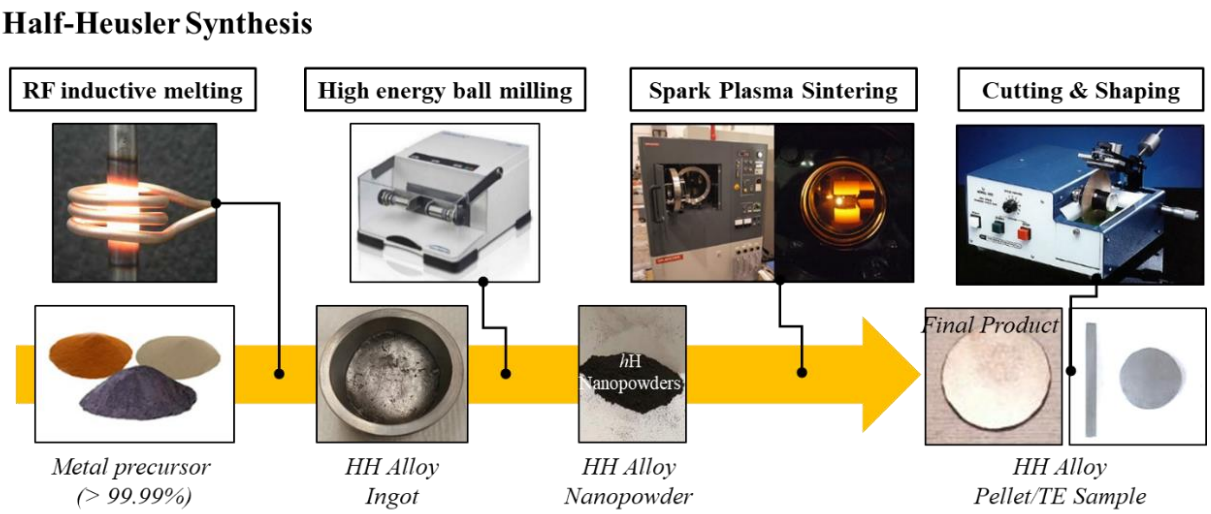

Figure 2.1 Schematic diagram of experimental procedure for hH alloy synthesis.

2.2 Material Characterization

2.2.1 X-ray diffraction (XRD)

The crystal structure and phase formation was investigated using high resolution X-ray diffractometer (Model D8 advance, Bruker) with Cu-*K*α radiation (λ = 1.5418 Å). The refinement by Rietveld method was applied using Panalytical X'Pert highscore plus software. In order to study phase stability of hH alloys at higher temperatures, in-situ XRD was performed while heating the sample stage at 573, 673, 773, 798, 823, 848, and 873 K using Malvern Panalytical X'Pert^3 MRD system.

2.2.2 Microscopy analysis

The microstructure and elemental distribution of the hH alloys was studied using environmental scanning electron microscope (ESEM, Quanta 600 FEG, FEI) with an acceleration voltage of 20 kV. High-resolution iridium was coated on the SEM samples by sputter coater (Leica ACE 600). Cross-sectional SEM samples for the thermal stability study were mounted in Buehler

Probemet epoxy using sample mounting press (Simplimet 2000, Buehler). The mounted cross-sectional samples were polished using auto grinding/polisher (Multiprep, Allied High Tech Products Inc.) with a fine diamond suspension (0.05 μm). Multi-scale *n*-type hH nanocomposite structure was investigated using a high-resolution transmission electron microscope (HRTEM, JEOL 2100).

2.2.3 Physical property characterization

As shown in **Figure 2.2**, the electrical conductivity and Seebeck coefficient were simultaneously measured over the temperature range of 300 to 973 K using a commercial Seebeck coefficient/electric resistance measuring system (ZEM-3, Ulvac-Riko, Japan). The thermal conductivity was determined through the measurement of thermal diffusivity using a laser flash system (LFA 467 HT HyperFlash, Netzsch, Germany/ TC-1200RH, Ulvac-Riko, Japan). Specific heat (C_p) was measured with a differential scanning calorimeter (Netzsch DSC 214) under argon gas protection. Magnetotransport data, consisting of Hall resistivity (transverse electrical resistivity yielding carrier density) and longitudinal resistivity (yielding electrical conductivity and carrier mobility) were measured in a dedicated magnetotransport setup (8400 series, Lakeshore, USA) at room temperature (298 K), using 4-point contact van der Pauw sample configurations with in-paint ohmic contacts. Data was obtained over magnetic fields up to 1.4 T, with a sample current excitation of 200 mA rms. A voltage preamplifier and lock-in amplifier were used to measure the voltage signals. The linearity of the current-voltage characteristics of the ohmic contacts was verified up to the 200 mA excitation current.

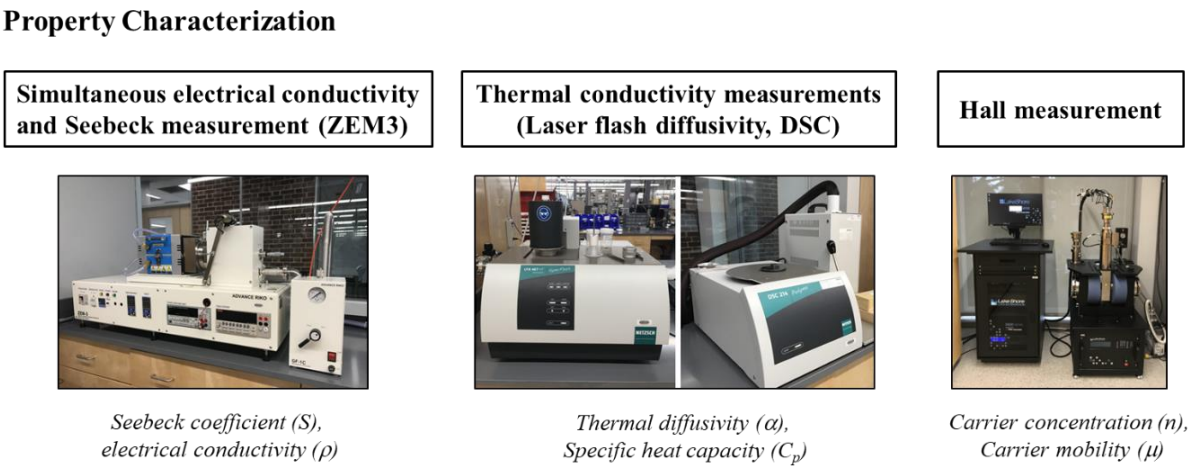

Figure 2.2 Physical property measurement systems for various thermoelectric parameters.

2.3 In-air thermal stability measurement

Figure 2.3 shows experimental procedure for steady-state stability test for half-Heusler alloys at high temperature in-air condition. Several bar-shaped samples were made from the same hH wafer (**Fig. 2.3a**) and then the mass, electrical resistivity, and Seebeck coefficient of the samples were measured at room temperature as represented in **Figure 2.3b** and **2.3c**. The samples show good uniformity in electrical resistivity and Seebeck coefficient. High temperature annealing was applied at 823 and 873 K for 24 and 72 hours in air using box furnace (Blue M box furnace, Lindberg). After the heat treatment, a variation of the base property for annealed samples was explored using ZEM-3 and high resolution electronic balance. The oxidation phases on the surface of annealed samples were identified by XRD (Model D8 advance, Bruker) as described in *the section 2.2.1*. In addition, cross-sectional SEM/EDS mapping was performed to estimate the oxide thickness and elemental analysis as discussed in *the section 2.2.2*.

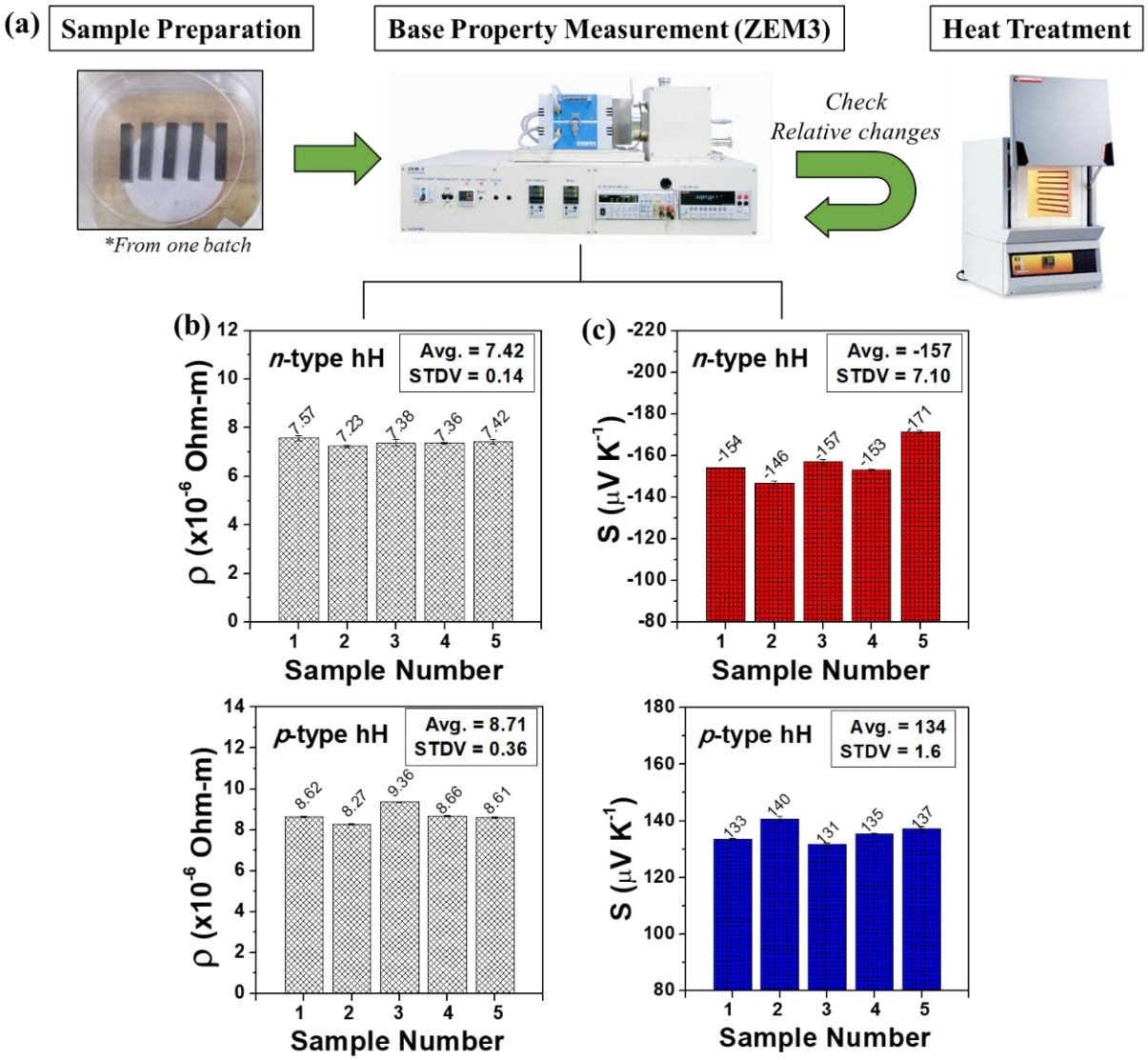

Figure 2.3 (a) Experimental procedure for steady-steady thermal stability test, (b) baseline measurement of electric conductivity, and (c) Seebeck coefficient.

2.4 TEG module fabrication

Figure 2.4 represents the TEG fabrication process based on the developed half-Heusler compounds. The uni-couple hH based TEG modules were fabricated using *n*-type $(Hf_{0.5}Zr_{0.5})NiSn_{0.99}Sb_{0.01}$ half-Heusler with 5 wt% of tungsten nanocomposites and two different

p-type $(Hf_{0.4}Zr_{0.4}Ti_{0.2})CoSb_{0.8}Sn_{0.2}$ and $(Nb_{0.6}Ti_{0.4})FeSb_{0.95}Sn_{0.05}$ compounds. The hH wafers were cut into 2.2 mm x 2.2 mm x 1.94 mm legs for *n*-type and 2.3 mm x 2.3 mm x 1.95 mm legs for *p*-type materials. The *p*- and *n*-legs were connected electrically in series and thermally in parallel by the copper interconnect high-temperature brazing material.

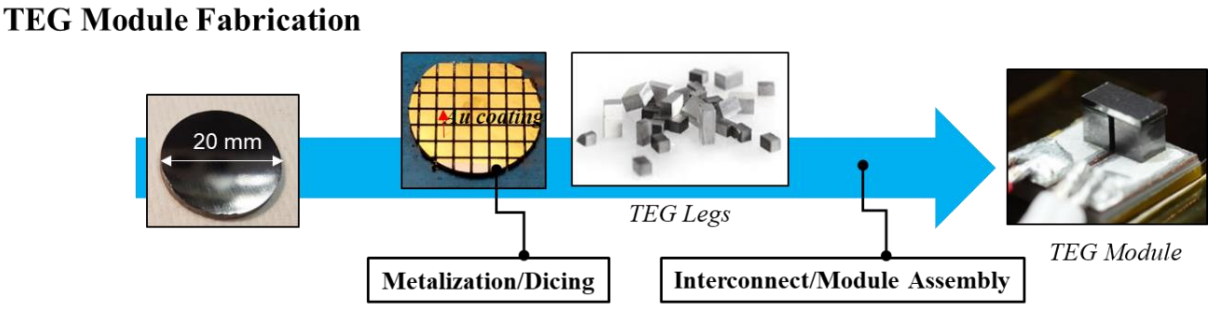

Figure 2.4 Schematic flowchart of TEG module fabrication from a sintered hH wafer to an uni-couple TEG module.

2.5 Device measurement

The contact resistance of legs was measured using home-made scanning probe system [64]. The simultaneous measurement of the output power and the efficiency for TEG was performed under the vacuum condition with a pressure of ~10^{-6} mbar. A constant heat flow from the heater was applied on top side of TEG using home-made power supply. The TEG output performance was evaluated by recording the open circuit voltage (V_{oc}), device voltage (V_d), internal resistance (r_i) and the peak power output (P_{max}) with changing hot side temperature from 473 K to 1023 K under constant cold-side temperature at 293 K. The detailed set up of the measurement is illustrated in **Figure 2.5**.

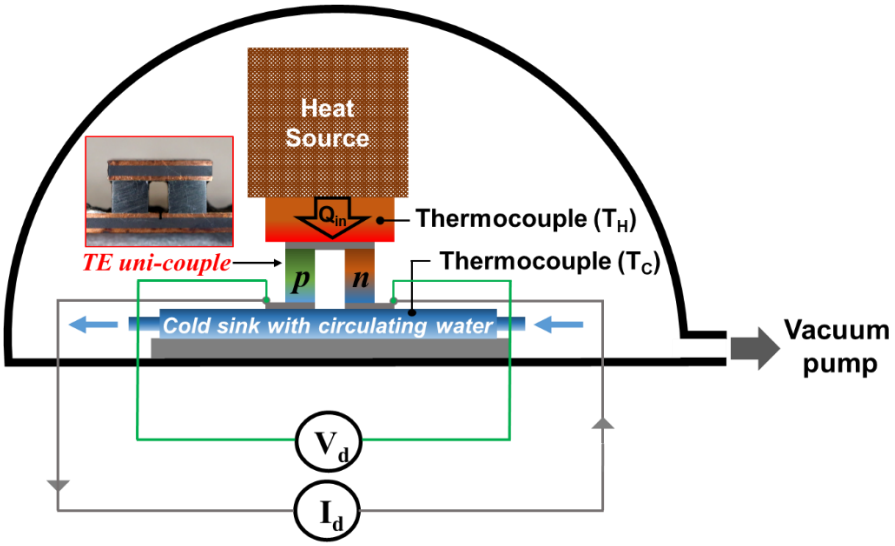

Figure 2.5 Schematic illustration of setup to measure TEG performance and picture of half-Heusler uni-couple TEG

Chapter 3 Fine tuning of thermoelectric properties on *n*-type (Hf,Zr)NiSn half-Heusler alloys

3.1 Introduction

Thermoelectric properties are highly sensitive to the chemical composition, phase purity, crystal structure, and microstructure of materials which affect the electrical and thermal transport behavior. For example, the presence of an impurity phase in thermoelectric compounds leads to a stoichiometric imbalance of the composition and changes carrier density and mobility. This further results in a large deviation in the electrical conductivity and the Seebeck coefficient from the desired number [65-67]. This can also impact the material's thermal conductivity through impurity scattering [68]. The grain size and microstructure play an important role in controlling the thermal conductivity when the length scale is comparable to the mean free path of phonon and electrons for enhanced boundary scattering [15,18]. The thermoelectric parameters are strongly interrelated with each other as discussed in *chapter 1*. For instance, increasing carrier concentration results in a higher electrical conductivity, a lower Seebeck coefficient and an increase of electronic thermal conductivity (κ_e). Thus, there will be limited effect on the zT value.

It is obvious that an optimization of the synthesis process and material composition is needed to achieve a higher zT. In this chapter, we systematically studied *n*-type MNiSn (M = Hf, Zr) based alloys by methodically controlling processing parameters ranging from melting to sintering conditions. The peak zT of *n*-type hH alloy reached to 0.97 at 873K through this comprehensive optimization.

3.2 Synthesis of pure half-Heusler phase

Figure 3.1 shows the phase formation of *n*-type (Hf,Zr)NiSn compounds with different crucibles utilized during the RF induction melting. Out of the various melting techniques, RF induction melting process has benefit in producing homogenous alloys by natural metal stirring from magnetic fields. Pure metal precursors are filled in a crucible and placed in a quartz tube with vacuum sealing as shown in **Figure 3.1a**. After purging and filling argon gas three times, high-frequency alternating current (AC) is applied to heat up the crucible under argon gas flow. Either the crucible or the precursor material should be electrically conductive to heat up by the formation of eddy current. The crucible should be thermally stable and robust to be able to handle the high temperature melting process.

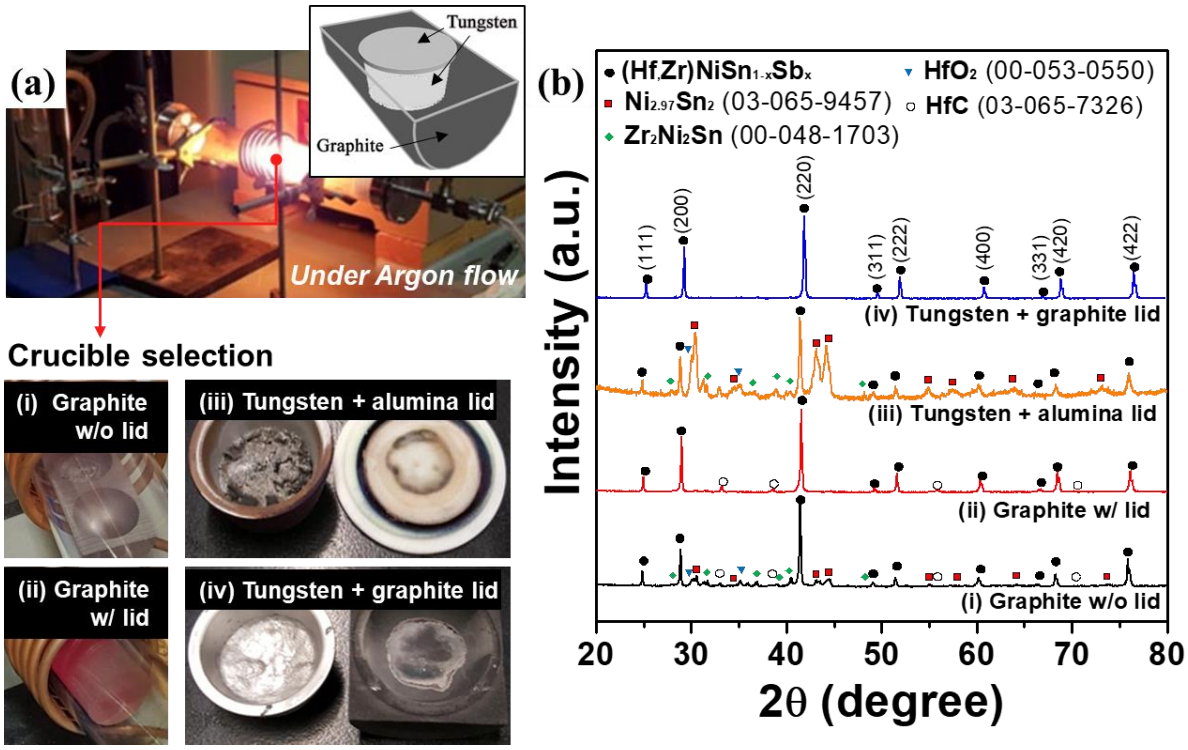

Figure 3.1 (a) RF induction melting set-up and (b) the XRD results of *n*-type hH ingots depending on the crucible selection (i-iv). The inset illustration in (a) represents a final design of the crucible for the melting process.

Due to high melting point and reactive nature of some precursors such as hafnium ($T_{m.p}$ = 2500 K) and zirconium ($T_{m.p}$ = 2128 K), some impurity phases were observed when RF induction heating or heat conservation is not sufficient by removing a lid (**Fig. 3.1a-i**) or by applying an insulating lid (**Fig. 3.1a-iii**) as shown in **Figure 3.1b**. In addition, a graphite crucible reacts with hafnium and produces a hafnium carbide phases (**Fig. 3.1a-ii and 1b**). The tungsten crucible with a conductive lid (**Fig. 3.1-iv**) provides not only sufficient heating but also a good heat conservation as a closed system, resulting in a single pure phase formation. It is noted that graphite has benefits in the induction heating from quicker built-in heat and faster heat transfer due to higher electrical resistivity ($\rho_{graphite}$ = 3-60 x 10^{-5} $\Omega \cdot m$ and ρ_W = 5.6 x 10^{-8} $\Omega \cdot m$) and thermal conductivity ($\kappa_{graphite}$ = 470 $W \cdot m^{-1} \cdot K^{-1}$ and κ_W = 173 $W \cdot m^{-1} \cdot K^{-1}$) even though it makes the impurity phase upon contact with hH. Therefore, the most suitable crucible materials to melt half-Heusler composition is found to be the tungsten crucible with a graphite heat supporter around the crucible as illustrated in the inset of **Figure 3.1a**.

Next, high energy ball milling was used to make nano-sized powders subsequent to the RF induction melting as shown in **Figure 3.2a**. It is important to properly seal a milling jar under inert atmosphere before and after milling to avoid powder oxidation during the loading process. The exposure of the powder to the air can lead to a rapid ignition (the inset of **Fig. 3.2b**) due to high oxidation reactivity of the nanopowders with increasing surface area, resulting in impurity phase formation of hafnium oxide and zirconium oxide as shown in **Figure 3.2b**. **Figure 3.3** presents the microstructure of the hH nanopowders before and after ball milling. It is clear that the particle size is noticeably reduced by the milling process from few tens of micron to few hundred nanometers. In addition, the size and shape of the particles are much more uniform in contrast to the ingot case.

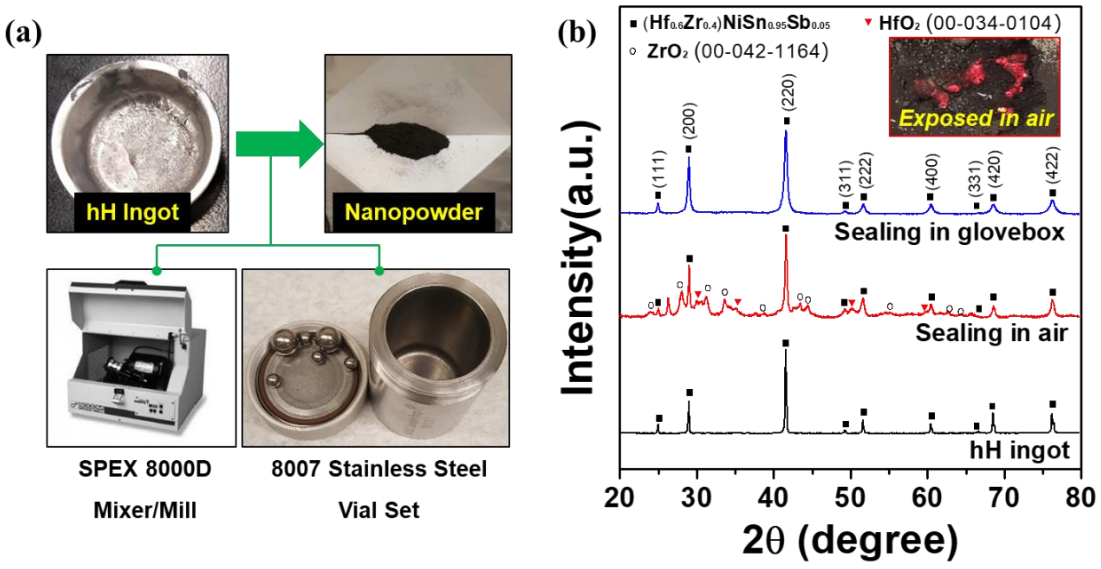

Figure 3.2 (a) High energy ball milling process for a pulverization of hH ingot in nano-scale (b) XRD results of the nanopowders according to the process conditions.

Figure 3.4 shows PXRD peak broadening effect by increasing ball milling time up to 6 hours. All the samples exhibit a single phase without any impurity phases and the diffraction peak became broader with the longer milling time. The peak broadening can be related to particle size reduction as peak width is inversely proportional to crystallite size through Scherrer equation. The Scherrer equation is given as:

$$\beta(2\theta) = \frac{K \cdot \lambda}{L \cdot cos\theta} \qquad (3.1)$$

where λ is the X-ray wavelength ($\lambda_{[Cu\text{-}K\alpha]}$ = 0.15418 nm), θ is the Bragg angle, L is the mean size of the crystalline domains, β is full width half maximum (FWHM), and K is dimensionless shape factor of the crystal. The crystallite size of the nanopowders is plotted as a function of milling time using the equation 3.1 as represented in **Figure 3.4b**. Here, the calculated size may be smaller or equal to the grain size. The crystallite size decreases with increasing milling time and the shrinkage rate reduces after 4 hours.

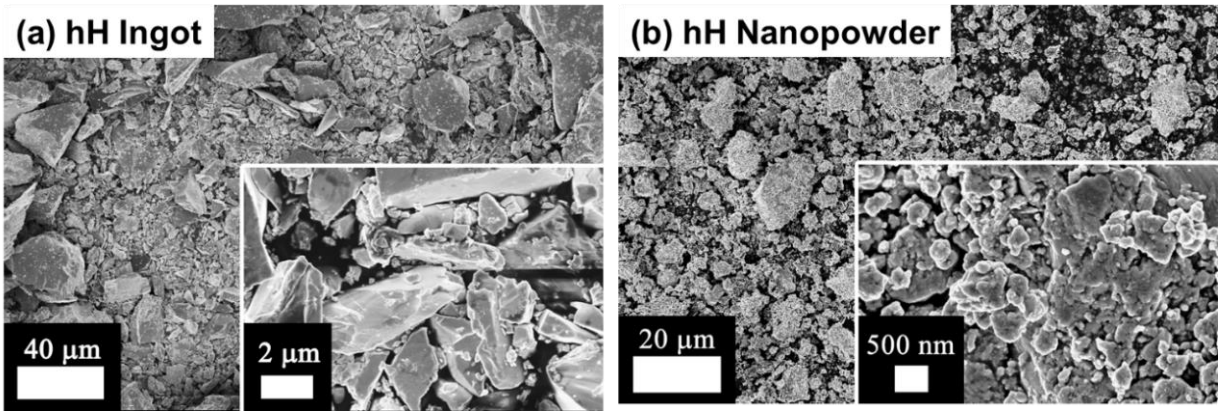

Figure 3.3 SEM images of *n*-type hH (a) ingot and (b) nanopowder after 4 hours of milling.

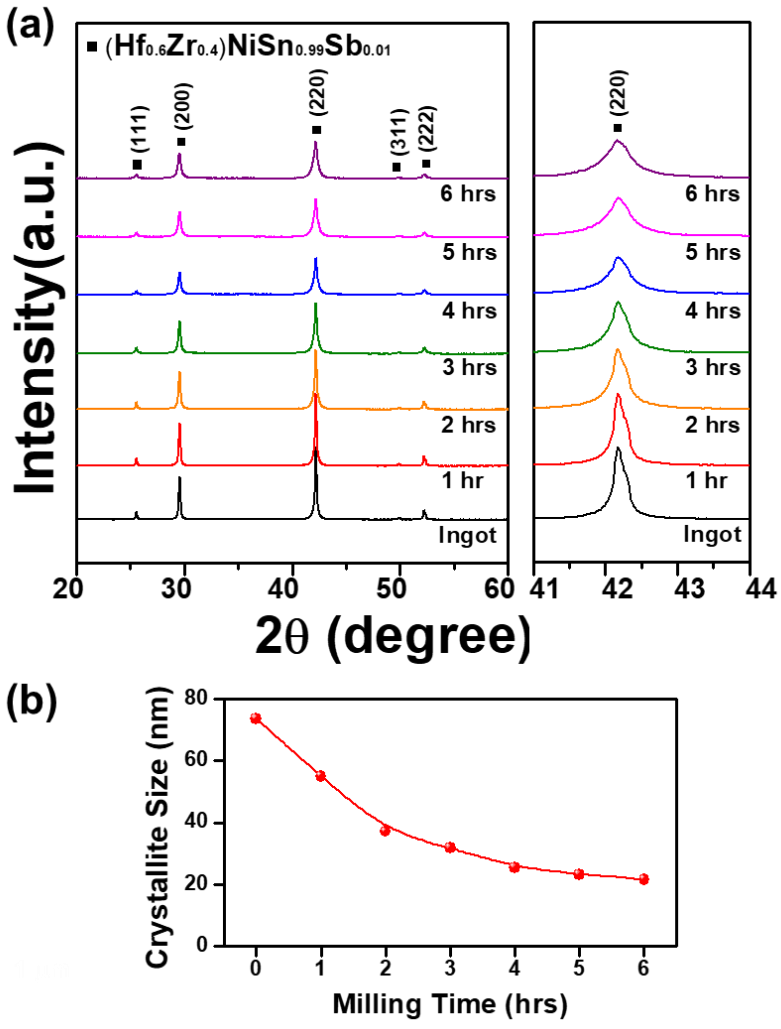

Figure 3.4. (a) Powder x-ray diffractions as a function of high energy ball milling time, (b) corresponding crystal size calculated from x-ray line broadening.

3.3 Effect of sintering temperature on thermoelectric properties

The nanopowder was consolidated using spark plasma sintering (SPS) technique as presented in **Figure 3.5a**. **Figure 3.5b** describes the basic configuration of SPS system. The powder is stacked in a graphite die with the pressure applied along the vertical direction. The pulsed DC power is applied to the electrode and the DC current directly passes through the graphite die and the powder. It generates internal heat in the sample resulting in rapid heating of the material. In contrast, during conventional sintering techniques, heat is provided by external heating source. This internal heating using SPS allows a very high rate of heating or cooling as shown in **Figure 3.5c**. This enhances densification of the sample within a short period of holding time (2~5 min). These features allow retaining of nanosized grains in the densified bulk from a nanopowder by restricting the coarsening and grain growth. Using SPS technique, the optimization of sintering temperature was conducted in *n*-type $(Hf_{0.6}Zr_{0.4})NiSn_{0.99}Sb_{0.01}$ compound.

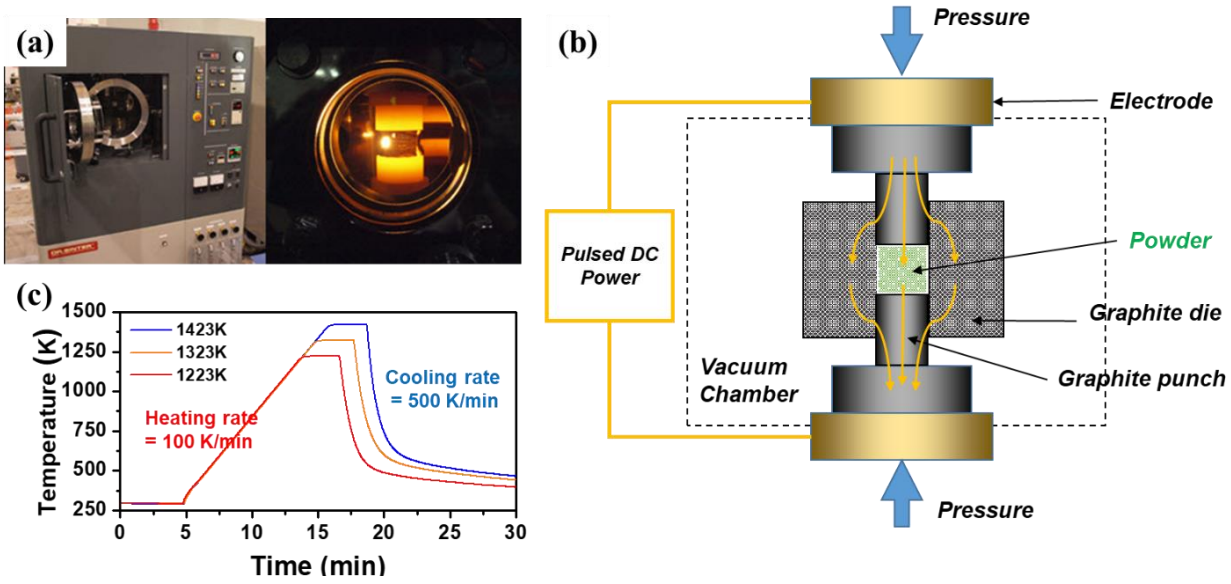

Figure 3.5 (a) Spark plasma sintering (SPS) process, (b) Schematic diagram of SPS system, and (c) temperature profiles of three different sintering conditions.

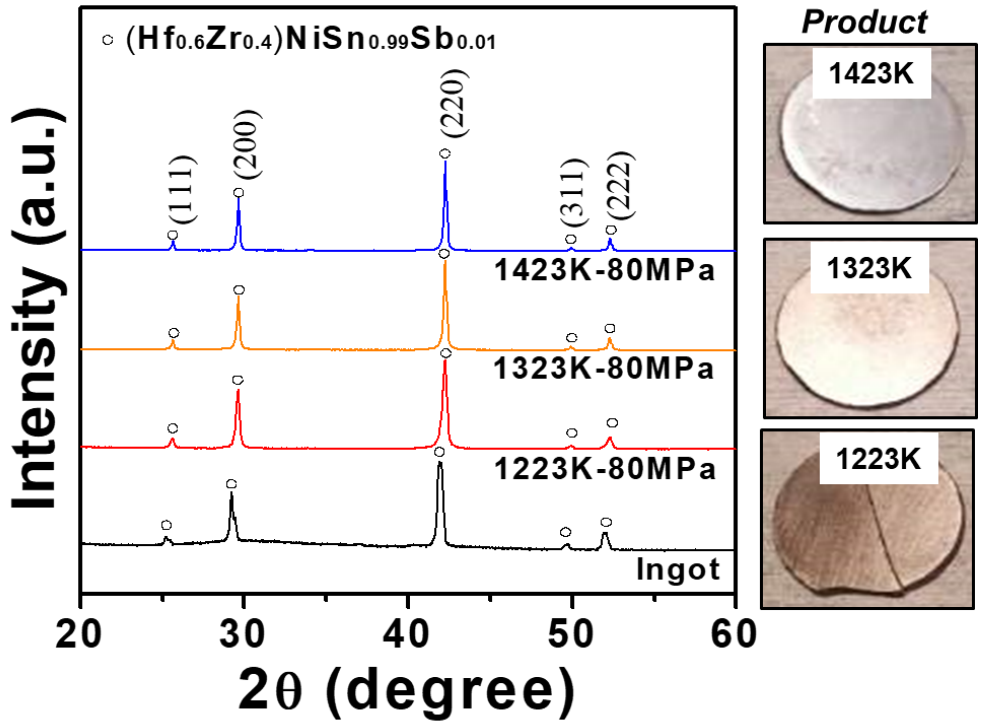

Figure 3.6 X-ray diffraction of SPS pellets as a function of sintering temperature and pictures of obtained samples.

Figure 3.6 represents XRD results under three different sintering temperatures. All three samples show a single phase and no peak shift is observed. Lower sintering temperature of 1223 K results in a poor mechanical strength with some cracks in contrast to the higher sintering temperature (product pictures shown in **Fig. 3.6**). The SEM images in **Figure 3.7a-c** display the effect of sintering temperature on microstructure and density of hH alloy. In general, the SPS pellets exhibit a high density of over 95 % in spite of short sintering time of about 20 minutes, and the density is further improved by applying higher temperatures. The grain size is also gradually increased by elevating sintering temperature as shown in **Figure 3.7d**. The average grain size almost doubles from 450 nm to 1 μm when the sintering temperature is increased from 1223K to 1423 K.

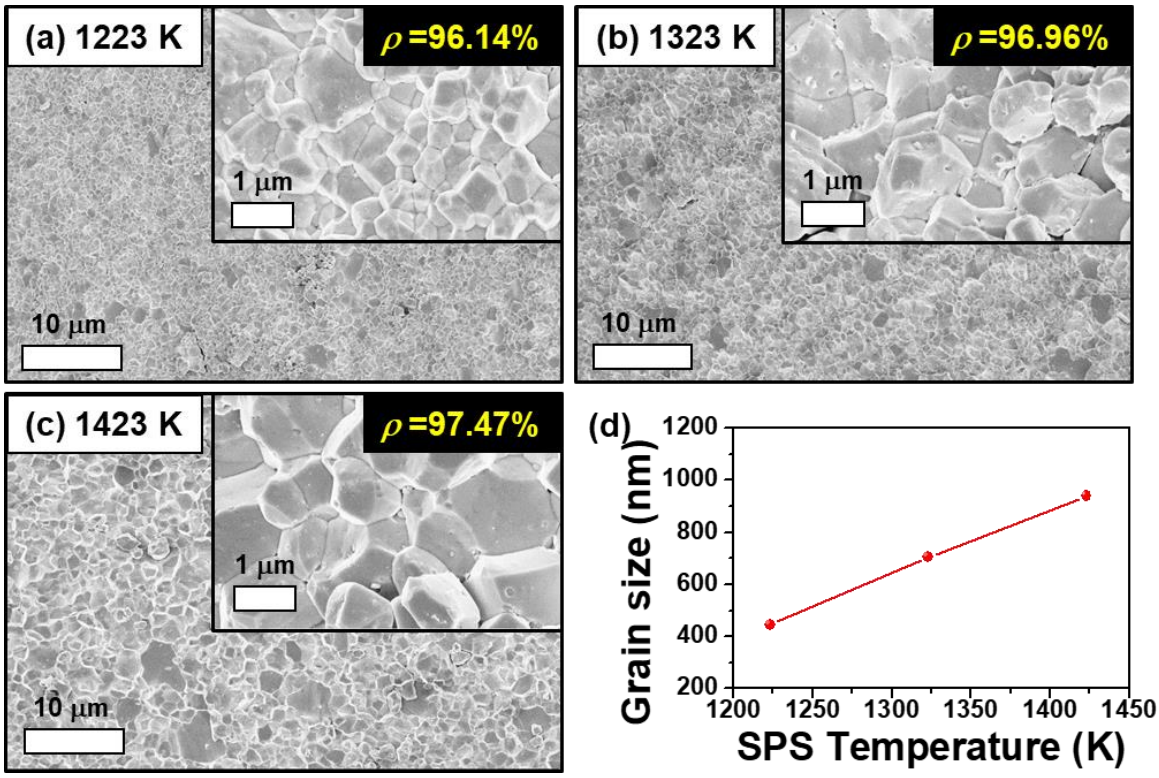

Figure 3.7 SEM images of SPS pellets after sintering at (a) 1223 K, (b) 1323 K, and (c) 1423 K. (d) The average grain size as a function of the temperature.

Figure 3.8 shows the TE property dependence on sintering temperature in *n*-type $(Hf_{0.5}Zr_{0.5})NiSn_{0.99}Sn_{0.01}$ compound. In general, the electrical conductivity is decreased by increasing temperature in a degenerate semiconductor and the lower sintering temperature leads to a rapid drop in the electrical conductivity (**Fig. 3.8a**). Basically, the grain boundaries can act as a scattering center for both charge carriers and heat-carrying phonons and the impact becomes more significant when the grain size considerably goes down to the scale of mean free path of the carriers. Thus, the nanoscale low temperature SPS sample (1223 K) exhibits a substantial decrease in the electrical conductivity by electron-grain boundary scattering in contrast to the higher temperature SPS samples (1323 K and 1423 K). On the other hand, the Seebeck coefficient is increased by reducing the grain size as shown in **Figure 3.8b**. It can be noted that grain boundary can negatively affect the carrier mobility through electron scattering at grain boundaries, however,

it is possible to have a positive impact through energy filtering effect. Minnich *et al.* [69] theoretically showed that low energy electrons can decrease the Seebeck coefficient from a negative portion of the Seebeck distribution curve in heavily doped *n*-type $Si_{80}Ge_{20}$. If scattering mechanism at the grain boundaries is taking place with the energy filtering which preferentially scatters electrons having energies less than the barrier height of the boundary, it can contribute towards higher Seebeck coefficient. As a result, power factor of the three samples are comparable to each other due to balance in the changes occurring between electrical conductivity and Seebeck coefficient (**Fig. 3.8c**). **Figure 3.8d** shows that the effective reduction in the thermal conductivity results from the smaller grain sizes. Enhanced phonon scattering at the grain boundary leads to lower lattice thermal conductivity in samples sintered at lower temperatures as shown in **Figure 3.8e**. The effect of grain size reduction on TE properties is investigated in various TE material systems. Poudel *et al.*[26] demonstrated zT improvement from 1.0 to 1.4 using nanostructured bismuth antimony telluride bulk alloy (BiSbTe). Joshi *et al.* [17] and Yan *et al.* [16] reported simultaneous increase in the Seebeck coefficient and large reduction in the thermal conductivity through nanocomposite approach in *n*-type and *p*-type hH using ball milling process. Similar effect of nanostructuring was demonstrated in both of the *n*-type and *p*-type silicon germanium bulk alloy (SiGe) [39,40]. Here, our result show relatively smaller impact with different sintering conditions compared to the literature, because all the samples were processed using ball milling prior to SPS. There is compromise in electrical transport and thermal conductivity in samples sintered at lower sintering temperatures. The resultant figure of merit (zT) is similar under all three sintering conditions as represented in **Figure 3.8f** and the maximum zT of ~0.9 is achieved at 800 K from the sample sintered at 1423 K.

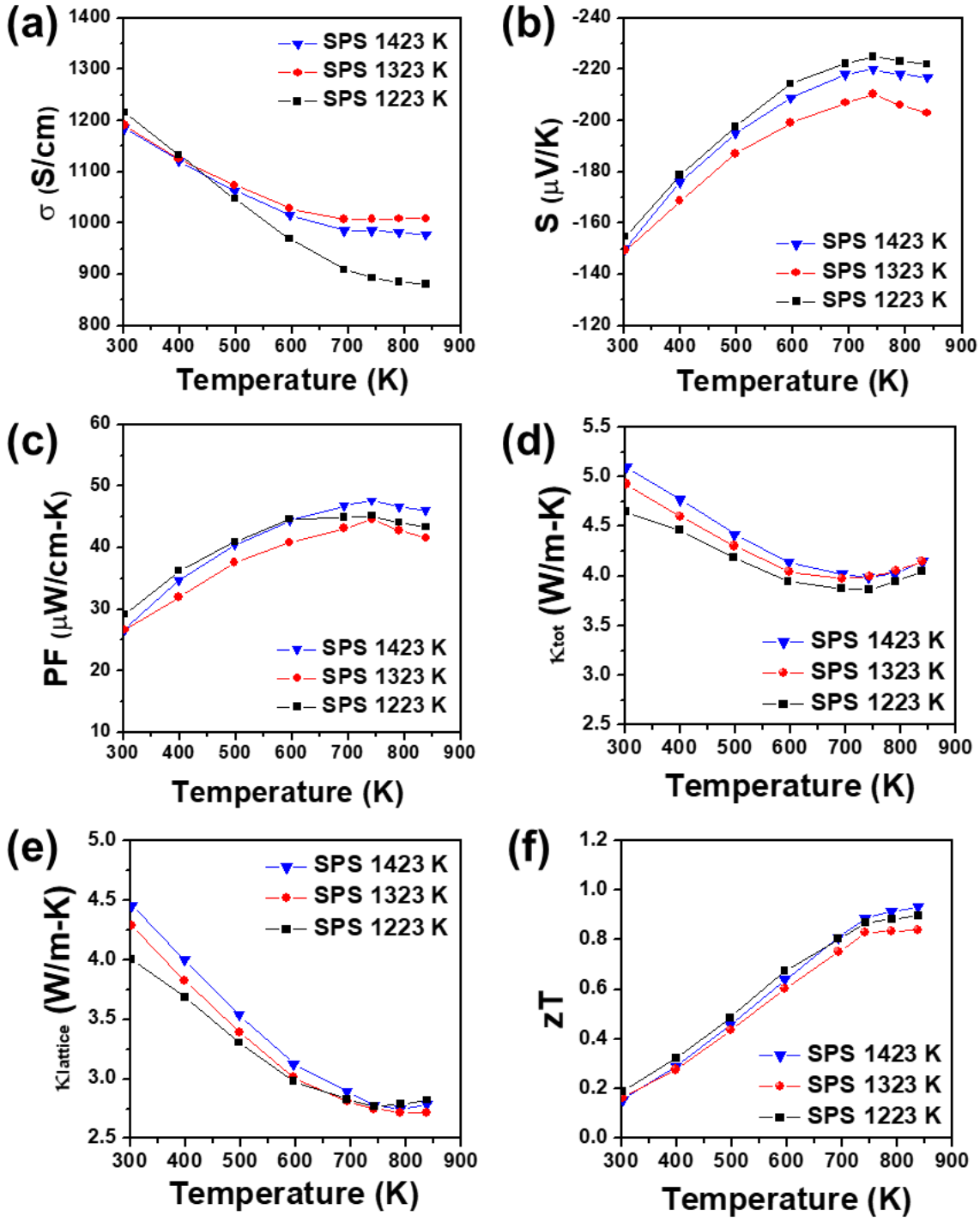

Figure 3.8 Thermoelectric properties of *n*-type hH alloys as a function of sintering temperature. (a) electrical conductivity, (b) Seebeck coefficient, (c) power factor, (d) total thermal conductivity, (e) lattice thermal conductivity, and (f) figure of merit (zT).

3.4 Thermoelectric property improvement through post-annealing process

As shown in **Figure 3.5c**, the spark plasma sintering process involves extremely fast heating and cooling rate (~500 K/min). It is beneficial to retain nanostructures in the densified sample by restricting the grain growth and mass diffusion. On the other hand, it will create structural imperfections such as various defects, phase instability (or segregation), and atomic structural disorder that can influence on TE properties. Thus, it can be expected that a subsequent heat treatment will provide additional tuning of TE properties. Here we studied the effects of post annealing (PA) process on the TE properties in *n*-type hH materials. The post annealing process is performed in tube furnace under argon environment.

Figure 3.9 shows XRD results of the post annealed samples under three different annealing conditions. All samples exhibit hH phase without any impurity phase formations during the heat treatments which means the samples are thermally stable up to 1023 K under inert gas atmosphere. There is a peak shift towards lower angle in the enlarged XRD spectrum between 41-44 two theta degrees in **Figure 3.9a** by applying sufficient temperature and time in the post annealing step. **Figure 3.9b** represents the variation of lattice parameter according to post annealing temperature that is extracted from the XRD patterns. It is obvious that higher temperature allows larger unit cell volume expansion. It is noted that the annealing temperature is low enough to restrict the further grain growth that simultaneously influences the TE properties as discussed in the previous section. This has been confirmed by the microstructure observation using SEM. There is no significant change in the grain size before and after heat treatment as shown in **Figure 3.10a and b** in comparison to the sintering temperature effect in the *section 3.3* (**Fig. 3.7**). Therefore, we can assume that the post heat treatment primarily influences atomic scale structure and defects rather than macroscopic reconstruction.

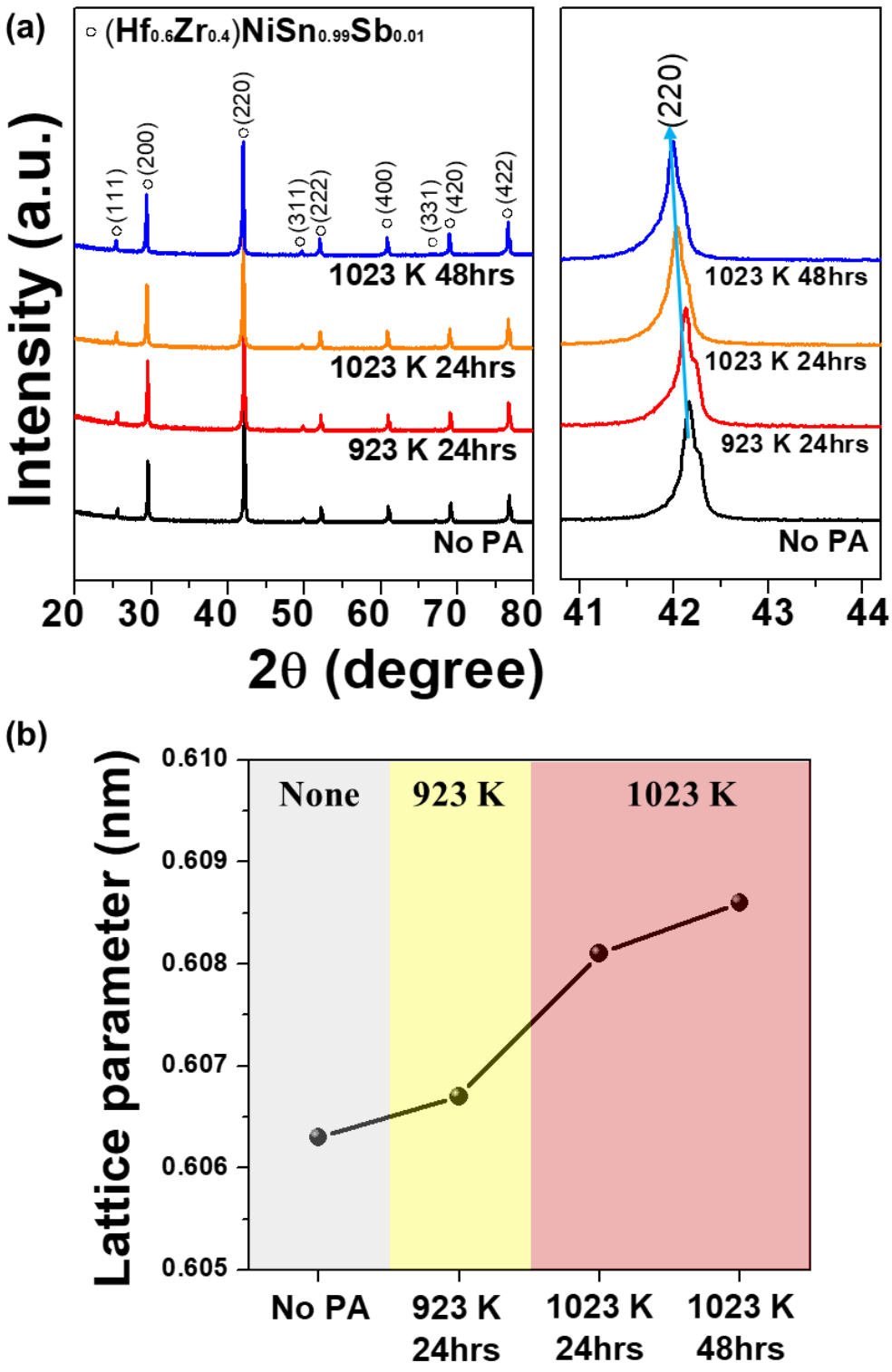

Figure 3.9 (a) XRD results with different post annealing conditions in the same *n*-type hH sample. (b) the calculated lattice parameter as a function of post annealing condition .

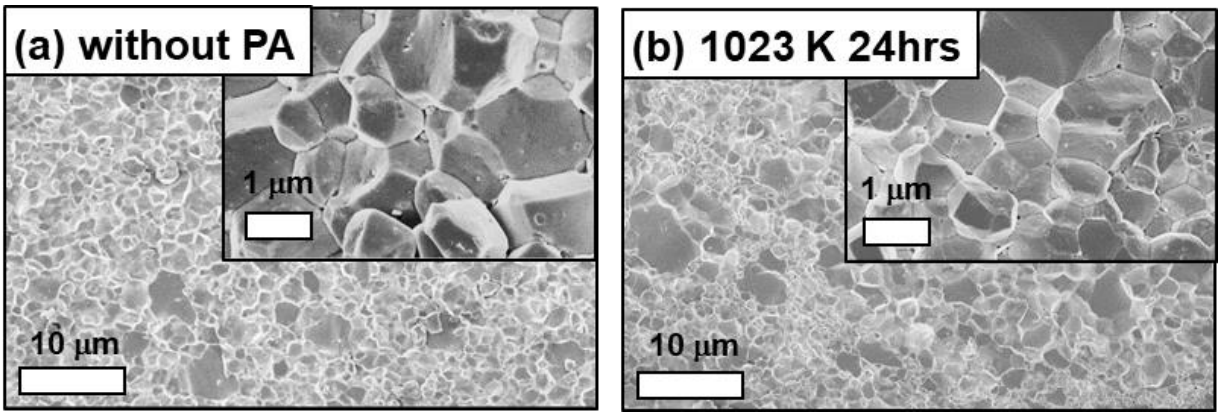

Figure 3.10 SEM image of hH (a) without post annealing (PA), and (b) post annealed hH at 1023 K for 24 hrs.

The atomic scale reconstruction through the PA process affects the carrier transport properties. **Table 3.1** represents the electronic transport characteristics including electrical conductivity, charge carrier concentration and carrier mobility depending upon the post heat treatment conditions. Interestingly the electrical conductivity is increased by applying higher annealing temperatures and it doesn't change significantly with annealing time duration. The low temperature annealing slightly increases the carrier concentration from 23.5 to 24.9x$10^{19}$$cm^{-3}$ with a negligible change in carrier mobility corresponding to small increase in electrical conductivity. A higher PA temperature simultaneously enhances the carrier concentration and mobility that leads to 28.6 % increase in the electrical conductivity. Increasing the annealing time to 48 hours from 24 hours has negligible effect on carrier concentration and mobility. These trends coincide with the unit cell extension inclination in **Figure 3.9b**, which implies that the variation of electronic transport properties is attributed to the atomic scale deformation and changes in structural imperfections. In addition, the results indicate that the atomic reconstruction requires sufficient energy to overcome certain activation barrier for mass and defect (or vacancy) diffusion.

Table 3.1 Room temperature carrier (electron) concentration and mobility of $(Hf_{0.6}Zr_{0.4})NiSn_{0.99}Sb_{0.01}$ compound versus post annealing (PA) conditions

Samples	σ (S/cm)	Carrier Concentration ($x10^{19}cm^{-3}$)	Carrier Mobility ($cm^2V^{-1}s^{-1}$)
No PA	1190	23.5	31.8
PA 923 K 24 hrs	1250	24.9	31.3
PA 1023 K 24 hrs	1530	27.6	34.6
PA 1023 K 48 hrs	1490	26.7	34.7

Further, the influence of PA process on the overall thermoelectric performance was investigated as shown in **Figure 3.11**. The electrical conductivity results are consistent with the Hall effect measurements (**Fig. 3.11a**). Interestingly, the Seebeck coefficient remains almost unaffected from PA process as displayed in **Figure 3.11b**. There are conflicting results in literature on the annealing effect in hH system [11,45,70-72]. Qie *et.al.* [71] reported that the annealed ZrNiSn shows higher electrical resistivity and Seebeck coefficient by controlling the antisite defect concentration. They observed a decrease in carrier concentration (*n*) with prolonged annealing in contrast to our finding. On the other hand, Xie *et al.* [72] demonstrated that there is no obvious distinction in electrical resistivity and Seebeck coefficient between unannealed and annealed ZrNiSn alloy, and both the properties are slightly decreased in annealed sample. The major difference between our result and the literature arises from the simultaneous increase of the carrier concentration and mobility. **Figure 3.12** shows the carrier concentration dependence of Seebeck coefficient with a theoretical Pisarenko curve derived from a single Kane band (SKB) model with the effective mass (m^*) of $2.8m_e$. The PA samples display higher Seebeck coefficient compared to the theoretical prediction that is possibly related to the presence of heavy electrons [11]. It needs

further study in conjunction with comprehensive theoretical calculation to verify all the possible scenarios.

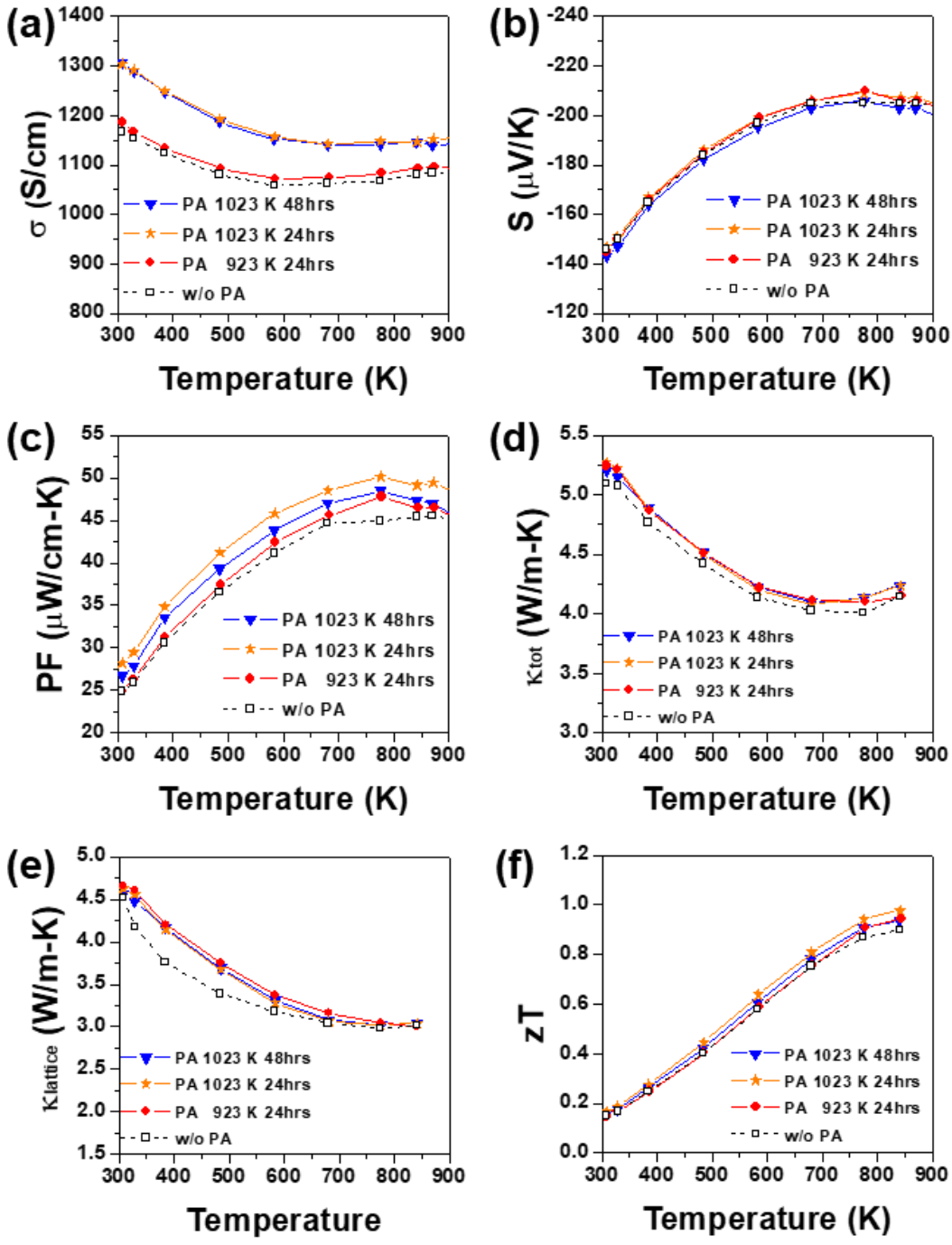

Figure 3.11 Thermoelectric properties of post annealed *n*-type hH alloys according to the PA process condition. (a) electrical conductivity, (b) Seebeck coefficient, (c) power factor, (d) total thermal conductivity, (e) lattice thermal conductivity, and (f) figure of merit (zT)

As a result of PA process, power factor is improved by 15 percent in the sample annealed at 1023 K for 24 hours (**Fig. 3.11c**). We also observed that there is a slight increase in thermal conductivity, more likely, due to the increase of lattice thermal conductivity with the reduction of defects that contribute to phonon scattering (**Fig. 3.11d and e**). Consequently, a peak zT of 0.97 is achieved at 873K and zT is improved by 10% in the overall temperature range in the sample annealed at 1023 K for 24 hours as represented in **Figure 3.11f**.

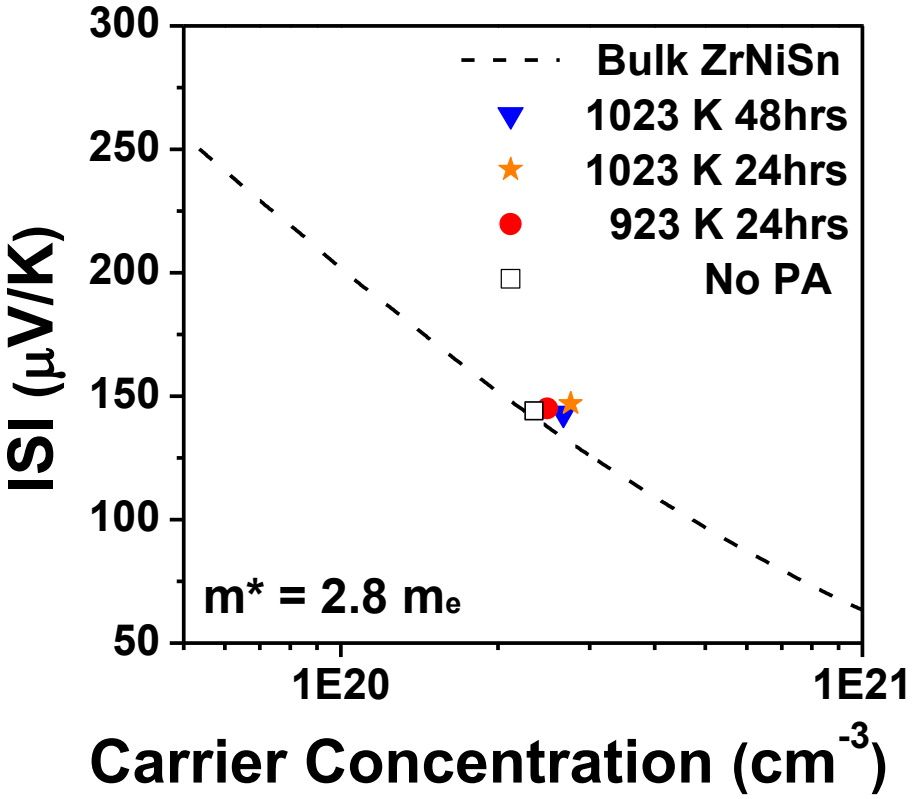

Figure 3.12 Seebeck coefficient versus carrier concentration for *n*-type hH according to post annealing conditions. The Pisarenko curve (dotted line) is obtained using a single Kane band (SKB) model with the DOS effective mass of $m^* = 2.8m_e$.

3.5 Conclusion

The comprehensive optimization for *n*-type $(Hf_{0.6}Zr_{0.4})NiSn_{0.99}Sb_{0.01}$ compound is studied by methodical control of processing parameter from melting to post heat treatment. Single phase hH was successfully synthesized using RF inductive melting. The hH ingot was transformed into nano-sized powders by high energy ball milling. The microstructure of the alloy was controlled by varying spark plasma sintering temperature. The smaller grain size led to decrease in the electrical conductivity and thermal conductivity simultaneously by enhanced scattering at the grain boundaries. Further, the thermoelectric performance was improved by post annealing process. By applying enough annealing temperature and time subsequent to SPS, an additional adjustment of TE properties was obtained with concurrent increase in carrier concentration and mobility accompanied with the variation in electrical conductivity and Seebeck coefficient. As a result, the maximum zT of ~1.0 was achieved by optimizing the processing parameters. This provides a good baseline for fundamental understanding of synthesis parameters and their influence on material property, which can be extended to the other material systems.

Chapter 4 Tailoring thermoelectric properties of *p*-type MCoSb (M = Hf, Zr, and Ti) half-Heusler alloys through dopant engineering

4.1 Introduction

MCoSb and MNiSn (M = Hf, Zr, and Ti) compounds are a good combination to design a TEG module due to similar values of TE properties and thermal expansion coefficient, which is helpful for better durability of device under repeated thermal cycling. In addition, the similarity of starting elements allows use of the same process for *p*-type hH synthesis as that developed for *n*-type hH alloys in *chapter 3*. In this chapter, the optimization of TE properties in *p*-type MCoSb system is studied based on the compositional modification.

In the hH system, we can expect two major effects from the doping approach. First the addition of donor or accepter into the semiconductor, controls the charge carrier concentration and mobility that primarily contributes to charge transport in semiconductor as discussed in the *section 1.2*. It is most effective way to tune the electrical conductivity (σ) and the Seebeck coefficient (*S*) to maximize power factor (σS^2) as shown in **Figure 1.2**. Another important effect of the dopant engineering is the presence of alloy scattering, resulting in a lower thermal conductivity. The substitution of occupied atoms by different atoms will create an atomic disorder and mass fluctuation in the crystal which provides additional scattering mechanism. Half-Heusler structure has three positions that can be doped as discussed in *section 1.4*. Here widely studied *p*-type MCoSb compounds are selected to explore the effects of compositional modification on TE properties. In this chapter, the dopant engineering will be studied as a powerful strategy for TE performance improvement.

4.2 Effect of Sn doping on TE properties

All the established processing conditions in *chapter 3* were successfully translated into *p*-type hH synthesis. **Figure 4.1a** displays the XRD patterns of *p*-type $(Hf_{0.5}Zr_{0.5})CoSb_{1-x}Sn_x$ compounds. All the compositions exhibit single phase without any impurity phases. A small peak shift towards lower angles is observed by increasing tin concentration. It is attributed to the replacement of small size antimony atoms (1.33Å) by bigger size tin atoms (1.45Å). As a result, the calculated lattice parameter is gradually enlarged by increasing tin concentration as shown in **Figure 4.1b**. It is obvious that the substitutional doping of tin (Sn^{+4}) on the antimony site (Sb^{+3}) creates more hole (h^+) carriers in the material corresponding to carrier concentration increase as represented in **Table 4.1**. Therefore, higher tin doping leads to increase in carrier concentration and slightly decrease in mobility, which imparts higher electrical conductivity.

Figure 4.2 shows the temperature dependence of the TE properties as a function of tin concentration (x = 0.10, 0.15, 0.20, and 0.25). The electrical conductivity results are consistent with the Hall effect measurement (**Fig. 4.2a**). The substitution of Sn on Sb site increases the electrical conductivity in the overall temperature region. It exhibits degenerate semiconductor or metal-like behavior with increasing temperature and follows temperature dependency according to relation, $\sigma \propto T^{-0.5}$ that implies alloy scattering is dominant mechanism in the transport [73]. Since there is a large increase in the carrier concentration with Sn doping, it can lead to lower Seebeck coefficient through the relationship, $S \propto n^{-2/3}$ as described in **Equation 1.10**. Thus the effect of Sn doping on the Seebeck coefficient is opposite to the electrical conductivity as shown in **Figure 4.2b**. The contrary relation between the electrical conductivity and the Seebeck coefficient results in counterbalancing calculation of power factor (σS^2) as displayed in **Figure**

4.2c. The lowest Sn doping represents the highest power factor due to the bigger impact of the Seebeck coefficient in the calculation (S^2).

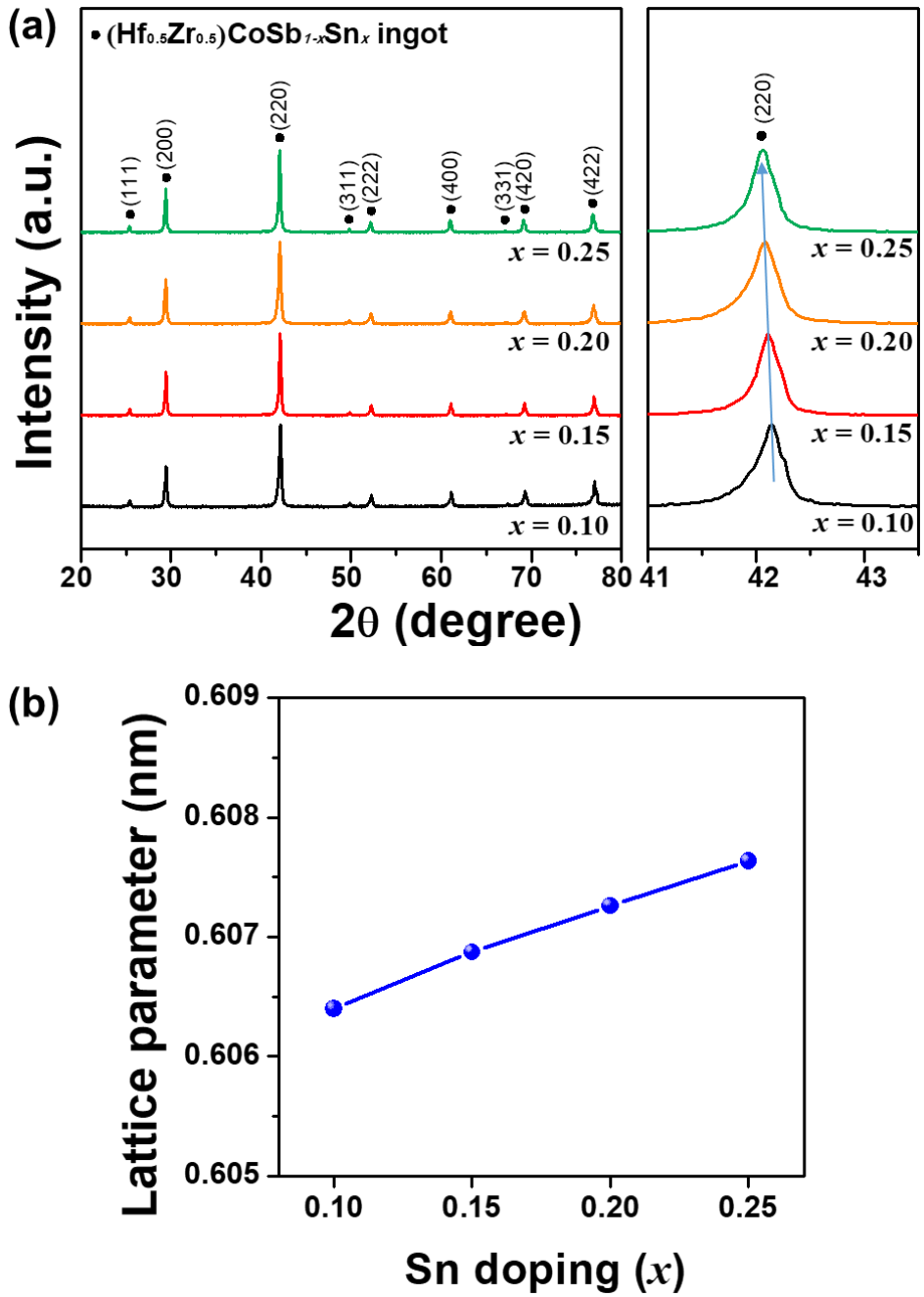

Figure 4.1 (a) XRD results as a function of Sn doping (x = 0.1, 0.15, 0.2, and 0.25) in *p*-type $(Hf_{0.5}Zr_{0.5})CoSb_{1-x}Sn_x$. and (b) the calculated lattice constant from the XRD.

Table 4.1 Room temperature carrier (hole) concentration and mobility of $(Hf_{0.5}Zr_{0.5})CoSb_{1-x}Sn_x$ compounds versus tin doping level

Sn doping (*x*)	σ (S/cm)	Carrier Concentration ($x10^{19}cm^{-3}$)	Carrier Mobility ($cm^2V^{-1}s^{-1}$)
0.10	668	79.8	5.23
0.15	748	92.2	5.04
0.20	1130	148.8	4.76
0.25	1390	194.9	4.54

As described earlier, the substitutional doping creates point defects and strain field fluctuation in the crystal that can influence the phonon transport behavior. Yuan *et al.* [74] demonstrated dramatic reduction in lattice thermal conductivity by Sn substitution in $ZrCoSb_{1-x}Sn_x$ compound. The induced strain field fluctuation effectively suppresses the lattice thermal conductivity. **Figure 4.2d** shows the significant influence of Sn doping on the thermal conductivity. The total thermal conductivity comprises of the electronic contribution and the phonon contribution (**Equation 1.11**). The presence of point defect can scatter the heat-carrying phonon and reduce the lattice thermal conductivity. Therefore, the lattice thermal conductivity is decreased by increasing Sn fraction as shown in **Figure 4e**. The electronic contribution of thermal conductivity is proportional to the electrical conductivity by Wiedemann–Franz law ($\kappa_e = L\sigma T$, **Equation 1.12**). Thus the higher tin concentration induces higher electronic thermal conductivity in opposition to the lattice thermal conductivity. As a result, the intermediate tin concentration presents the lowest total thermal conductivity (**Fig. 4.2d**). Finally, the highest zT of 0.87 was achieved in the tin content of 0.15 at 900 K as displayed in **Figure 4.2f**.

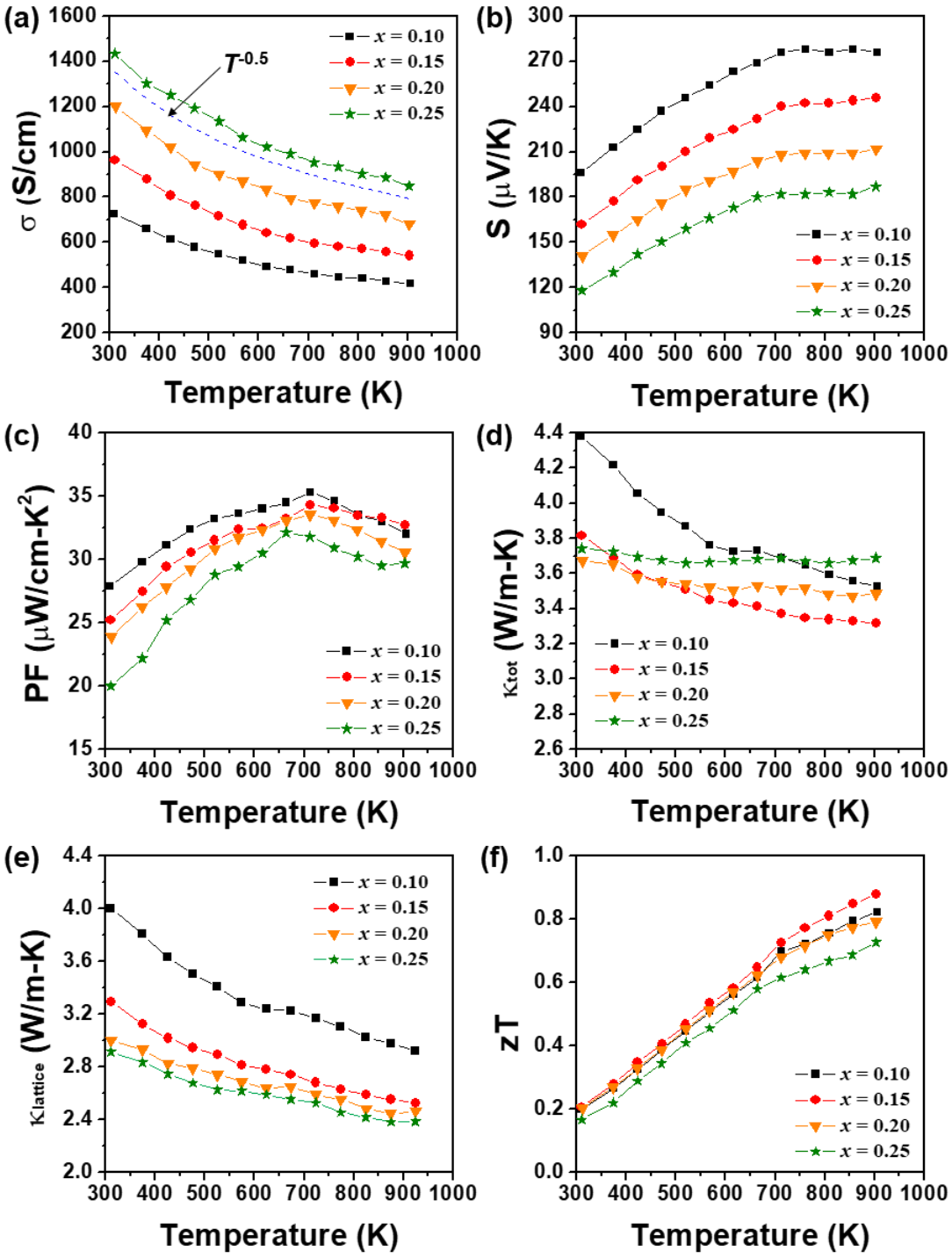

Figure 4.2 Thermoelectric properties of post annealed *p*-type $(Hf_{0.5}Zr_{0.5})CoSb_{1-x}Sn_x$ hH alloys depending upon Sn doping level (x = 0.1, 0.15, 0.2, and 0.25). (a) electrical conductivity, (b) Seebeck coefficient, (c) power factor, (d) total thermal conductivity, (e) lattice thermal conductivity, and (f) figure of merit (zT).

4.3 Reduced thermal conductivity through strong point defect scattering

Another effective method for tuning the TE properties is the substitution by larger atoms from the same group of elements in order to reduce lattice thermal conductivity. **Table 4.2** presents some of the possible group 4 elements that can occupy M site. Hafnium and zirconium have a similar atomic radius but different speed of sound and atomic weight. Titanium exhibits relatively larger difference in atomic size and mass compared to others. Therefore, the substitution of Ti on Hf/Zr site is likely to have more significant impact on the phonon transport. **Figure 4.3** displays the XRD patterns of $(Hf_{0.5}Zr_{0.5})_{1-x}Ti_xCoSb_{0.8}Sn_{0.2}$ compounds (x = 0.0, 0.1, and 0.2). The titanium atoms successfully replace Hf/Zr atoms without any impurity phase formation. The peak shift towards larger angle is observed with increasing titanium concentration. The substitution of Hf/Zr atoms by smaller size of titanium atom results in reduction of the lattice parameter and shrinkage of the unit cell.

Figure 4.4 represents the effects of Ti-substitution on TE performance in $(Hf_{0.5}Zr_{0.5})_{1-x}Ti_xCoSb_{0.8}Sn_{0.2}$ compositions. In comparison to Sn doping, there are much smaller changes in the electrical conductivity and the Seebeck coefficient with Ti doping. Basically Ti, Zr, and Hf belong to the same group in the periodic table, thus the substitution of element between them does not

Table 4.2 List of basic properties (atomic radius, weight, and speed of sound) for the selective elements in group 4 of periodic table

Atom	Atomic radius (nm)	Atomic weight	Speed of sound ($m \cdot s^{-1}$)
Titanium	0.147	47.867	4140
Zirconium	0.160	91.224	3800
Hafnium	0.159	178.490	3010

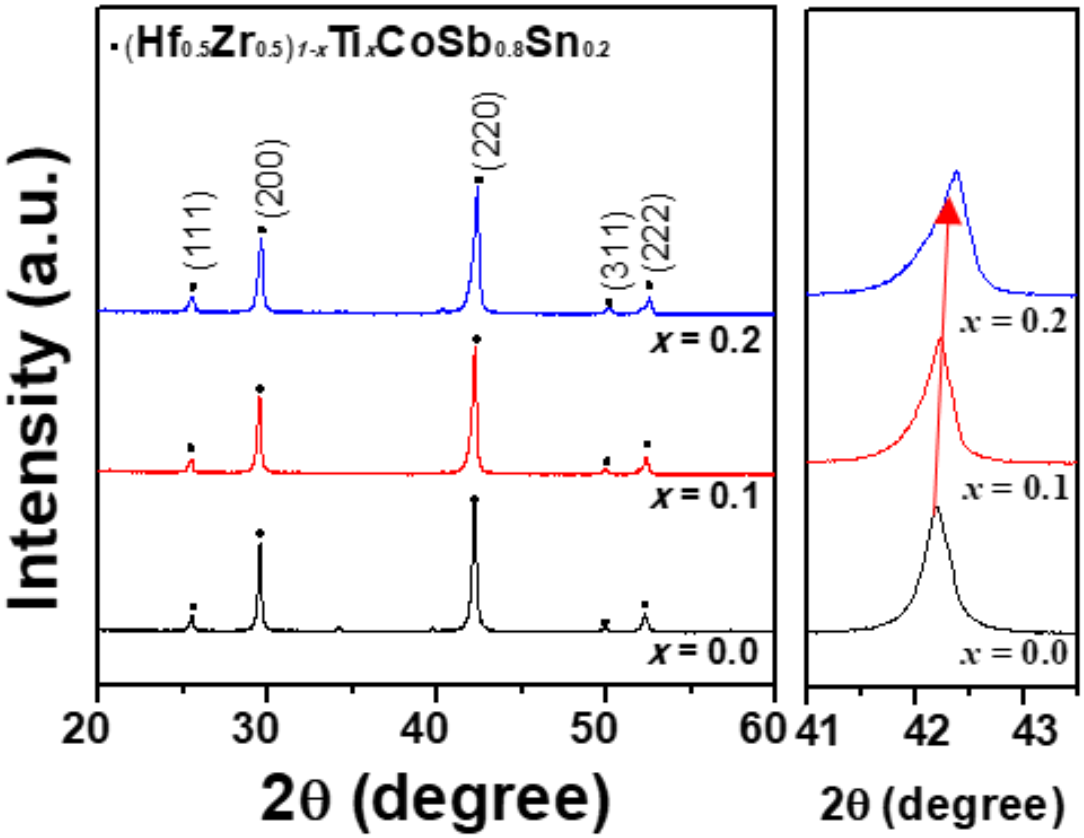

Figure 4.3 XRD results of $(Hf_{0.5}Zr_{0.5})_{1-x}Ti_xCoSb_{0.8}Sn_{0.2}$ compounds according to the titanium concentration (x = 0.0, 0.1, and 0.2).

create the additional charge carrier contrary to Sn doping. Instead, it is likely to impact carrier mobility through the presence of point defects and large mass fluctuation between Ti and Hf (or Zr). Higher Ti concentration slightly decreases the electrical conductivity and increases the Seebeck coefficient (**Fig. 4.4a and b**). Consequently, only small difference is observed in the power factor as shown in **Figure 4.4c**. Similar results were reported by He *et al.* [75] in $Hf_x(Zr,Ti)_{1-x}CoSb_{0.8}Sn_{0.2}$ system. Here, the biggest impact of Ti substitution is the reduction of thermal conductivity. **Figure 4.4d** shows that the replacement of 0.2 at% of titanium on Hf/Zr sites reduces the total thermal conductivity by 20 %. It is attributed to the enhanced phonon scattering by

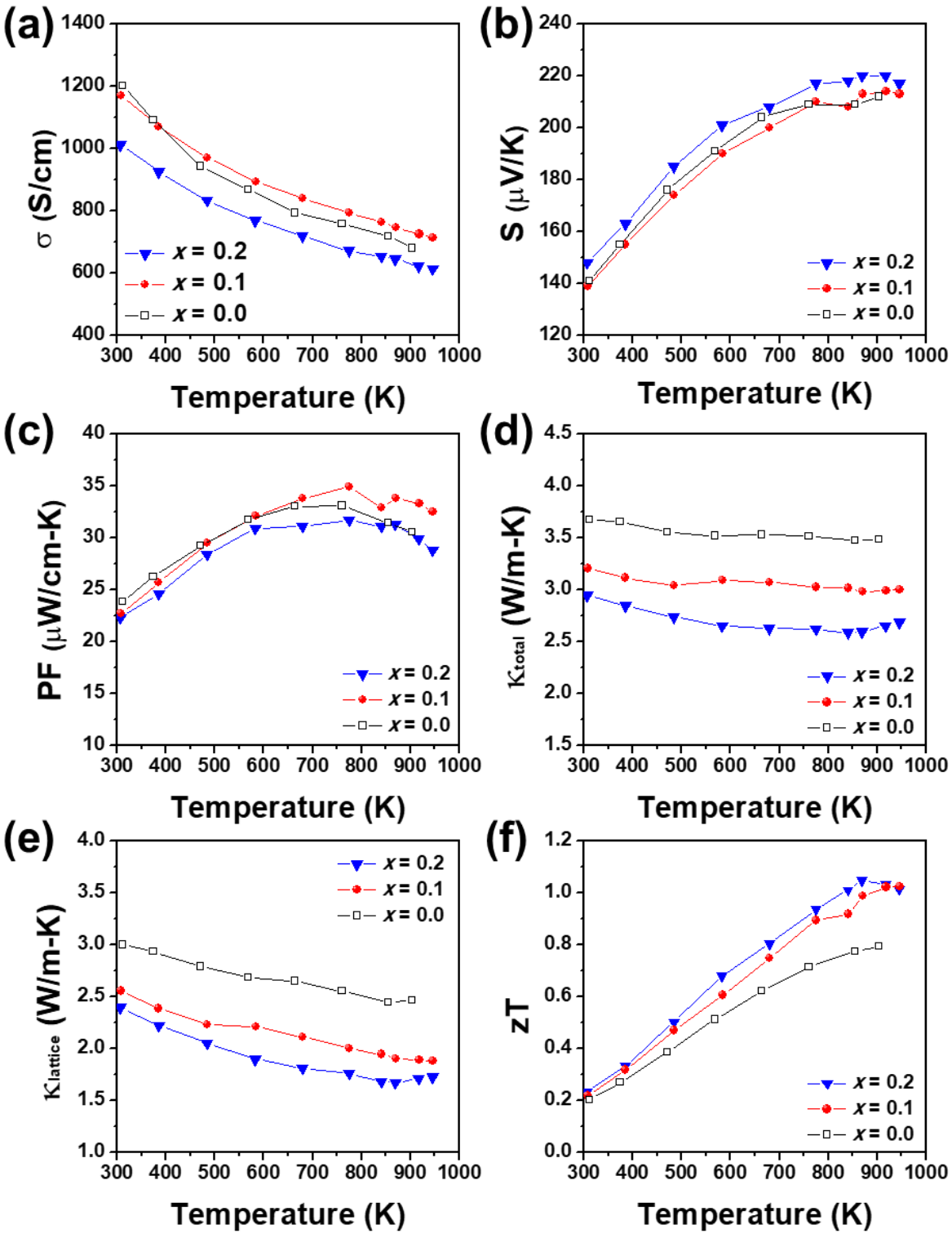

Figure 4.4 TE properties of *p*-type $(Hf_{0.5}Zr_{0.5})_{1-x}Ti_xCoSb_{0.8}Sn_{0.2}$ hH alloys (x = 0.0, 0.1, and 0.2). (a) electrical conductivity, (b) Seebeck coefficient, (c) power factor, (d) total thermal conductivity, (e) lattice thermal conductivity, and (f) figure of merit (zT).

stronger point defect scattering. Yan *et al.* [14] demonstrated an effective reduction in the lattice thermal conductivity by using larger difference in the atomic mass and size of Hf and Ti. Similar mechanism and impact were investigated in (Zr,Hf)NiSn and (Nb,Ta)FeSb alloys by Liu *et al.* [47]. As displayed in the **Table 4.2**, titanium has a large difference in atomic mass and speed of sound with zirconium and hafnium, thus, it introduces strong point defect scattering through the large mass and strain fluctuation in the crystal structure. The enhanced phonon scattering results in suppressing lattice thermal conductivity as shown in **Figure 4.4e**. As the final outcome, the zT of *p*-type hH was further improved by 25% in the overall temperature range and the maximum zT of ~1.0 was achieved at 873 K in $(Hf_{0.5}Zr_{0.5})_{0.8}Ti_{0.2}CoSb_{0.8}Sb_{0.2}$ compound as presented i**n Figure 4.4f**.

4.4 Conclusion

In this chapter, the optimization of TE properties in *p*-type hH alloys was investigated by dopant engineering. The electronic transport properties were controlled by Sn doping on Sb sites. The substitution of Sb atoms by Sn dopant creates additional hole-charge carriers, resulting in increase of electrical conductivity and decrease of Seebeck coefficient. Moreover, it suppresses lattice thermal conductivity by introducing point defect scattering. Another effective method for reducing thermal conductivity was studied by M-site substitution with an ion that has larger difference in atomic mass, size and speed of sound. Titanium replacement on Hf/Zr sites was found to an important role in suppressing lattice thermal conductivity through stronger point defect scattering. As a result, high zT of 1.0 was achieved at 873 K which is 25 % improvement for *p*-type $(Hf_{0.5}Zr_{0.5})_{0.8}Ti_{0.2}CoSb_{0.8}Sb_{0.2}$ compound.

Chapter 5 Decoupled heat-charge carrier transport in multi-phase *n*-type half-Heusler nanocomposites

5.1 Introduction

One promising approach towards suppressing lattice thermal conductivity is through incorporation of nanoscale inclusions into TE materials that enhances phonon scattering. Interestingly, it has been demonstrated that the new interface creation by nanoinclusions simultaneously contributes to improved power factor ($S^2\sigma$) and decreased lattice thermal conductivity through energy filtering. Faleev *et al.* [76] and Zebardaji *et al.*[77,78] predicted that a metal-semiconductor interface can provide an adequate potential barrier which can selectively block electrons depending on their energy, resulting in a higher Seebeck coefficient for a given carrier concentration. This effect has been experimentally demonstrated in many TE material systems. Heremans *et al.* [79] reported that Pb precipitates in PbTe compounds lead to the thermopower (S) enhancement by increasing the energy dependence of the relaxation time. Sumithra *et al.* [80] have demonstrated simultaneous reduction in the lattice thermal conductivity and enhancement in power factor by incorporating Bi nanoparticles into the Bi_2Te_3 matrix. Although the effect of nanoinclusions has been demonstrated in hH system as well, the reported figure of merit for the nanocomposites was much lower than that of unmodified hH compounds (zT ~1) [81-84] . Makongo *et al.* [83] revealed large increases in both electrical conductivity and Seebeck coefficient and moderate reduction of thermal conductivity by developing coherent internal phase boundaries in *n*-type full-Heusler/half-Heusler nanocomposites. In this case, the maximum zT of the best nanocomposite was ~0.7 at 775 K. Xie *et al.*[84] have shown similar effects through InSb nanoinclusions and reported that *n*-type (Ti.Zr,Hf)(CoNi)Sb nanocomposites

exhibit maximum zT of ~0.5 at 820 K. The nanocomposite strategies for hH system work on certain level, but overall they are not effective as much as in other TE materials. This is due to poor TE performance of base hH matrix and compatibility and stability problem of inclusions within hH alloys at high temperatures.

In this chapter, we simultaneously demonstrate the multi-scale phonon scattering and energy filtering of hot electrons in *n*-type $(Hf_{0.6}Zr_{0.4})NiSn_{0.99}Sb_{0.01}$ nanocomposites through introduction of tungsten nanoinclusions and nanoprecipitation. High melting point of the tungsten assists in suppressing undesirable reaction with hH matrix and grain growth at high synthesis temperatures. Our results show that the tungsten nanoparticles play a key role in effectively decreasing the thermal conductivity of the composite by boosting phonon scattering that is attributed to both interfacial phonon scattering between hH and tungsten due to large difference in acoustic impedence and integrated phonon scattering in broad length scale by forming multi-scale nanostructure. In addition, the tungsten nanoinclusions simultaneously enhance the electrical conductivity and Seebeck coefficient by creating a potential barrier at the metal/semiconductor interface, which creates an electron energy filtering effect. Owing to these favorable changes in electrical and thermal properties, we achieved a noticeably high figure of merit (zT_{max} ~1.37 at 873K and zT_{avg} ~0.91 in the range from 300K to 973K) for the optimum level of tungsten concentration of 5 wt% in *n*-hH/W nanocomposites.

5.2 Multiple phase nanocomposites through tungsten inclusions

Figure 5.1a illustrates the multi-scale structure in *n*-type hH nanocomposite with tungsten inclusions and nanoprecipitates. First, we designed the pristine hH matrix to optimize TE performance through compositional tuning and combination of RF inductive melting and spark plasma sintering. At the atomic level, multicomponent alloying of Hf and Zr at *M* sites facilitates lower thermal conductivity by strong phonon scattering at point defects in the lattice [44]. In addition, the rapid fabrication process introduces nano-sized hafnium precipitates in the hH matrix, which contributes towards improvement of TE performance [85,86]. The pristine *n*-type hH compound exhibits comparable TE performance with the state-of-art zT as shown in **Figure 5.1b** [17,46,47,87]. Next, metallic nanoparticles are incorporated in the base hH matrix as depicted in **Figure 5.1a**. Several parameters were considered in determining the inclusion material: i) stability and compatibility with the matrix at elevated temperatures, ii) large acoustic impedance mismatch between a metal (inclusions) and a semiconductor (TE materials), which is beneficial for increasing the phonon scattering effect at the metal-semiconductor interface, iii) low heat capacity, and iv) a multi-length scale architectural design with the nanoprecipitates, which efficiently scatters heat-carrying phonons. Tungsten nanoparticles were found to meet all these criterions and thus were selected as an inclusion material. The tungsten inclusions play important role in not only reducing thermal conductivity but also enhancing electronic transport properties. The best composition for the W/hH nanocomposite shows record high figure of merit in the overall temperature region up to 973 K (**Fig. 5.1b**).

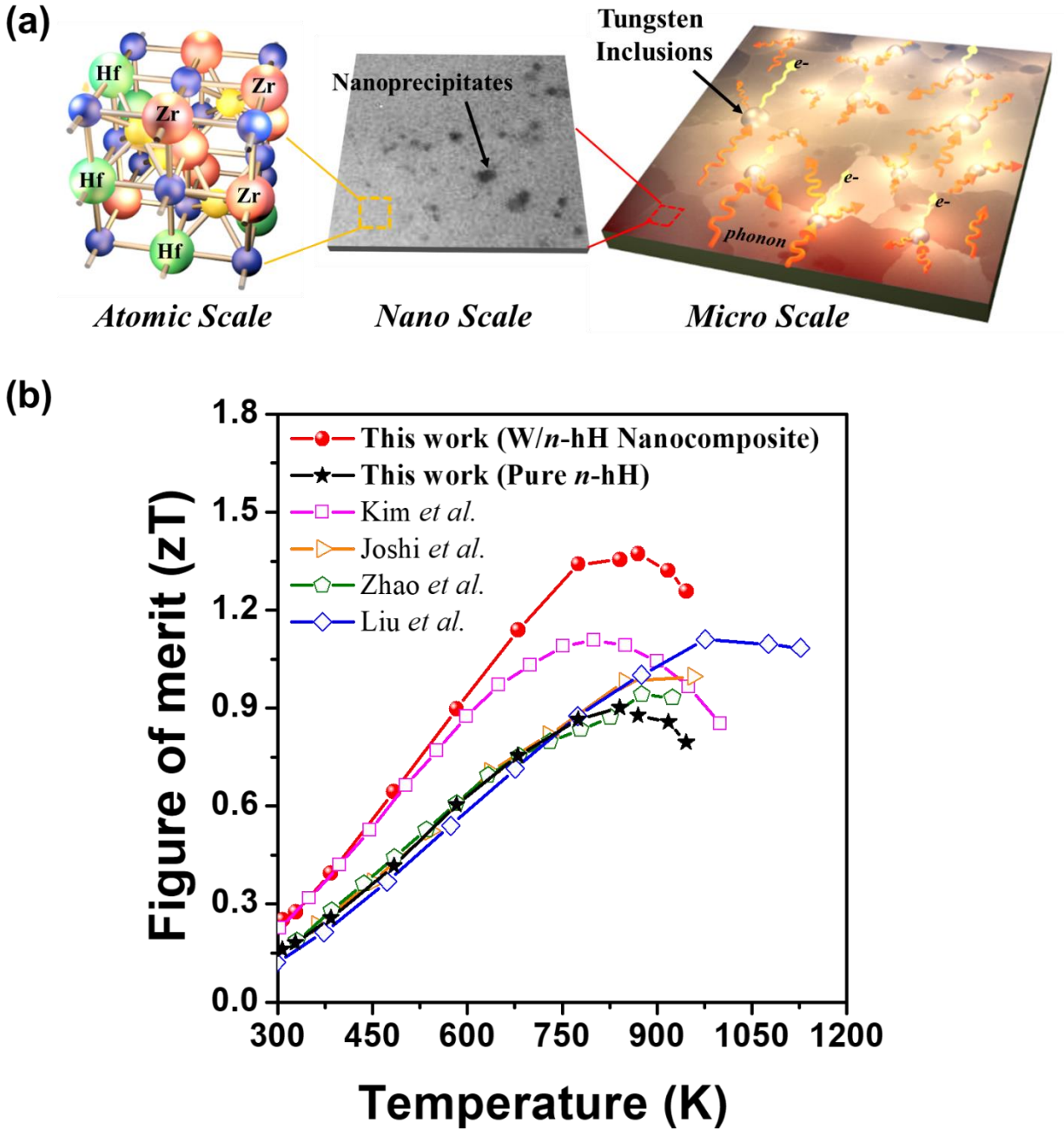

Figure 5.1 Schematic illustration of the nanocomposite and figure of merit comparison. (a) The structure of multi-scale *n*-type hH nanocomposite with tungsten inclusions. (b) The comparison of thermoelectric performance of the pure *n*-hH and the nanocomposites developed in this work with other literatures[1][17,46,47,87].

The desired phase formation for $(Hf_{0.6}Zr_{0.4})NiSn_{0.99}Sb_{0.01}$ + *x* wt% tungsten (W) nanocomposites (*x* = 0, 2, 5, and 10) was confirmed from X-ray diffraction analysis (**Fig. 5.2**). All samples exhibited hH phase without any secondary phases. Tungsten phase (JC-PDS, 00-004-0806) was observed in the diffraction patterns and the intensity of tungsten peaks increased at higher concentration of tungsten nanoparticles. We verified the distribution of tungsten nanoparticles by scanning electron microscopy (**Fig. 5.3**). The backscattered electron diffraction (BSED) image and corresponding energy-dispersive X-ray spectroscopy (EDS) demonstrated that tungsten nanoparticles are homogeneously and widely dispersed in the hH matrix. Tungsten has a high melting point (3695 K) which restricts grain growth of tungsten nanoparticles even under high sintering temperature of 1323 K. This advantage provides stable distribution of nanoinclusions in the hH matrix as represented in EDS mapping. The grain size is not dependent on the concentration of tungsten inclusions and the average grain size of the hH matrix is 1.39 μm.

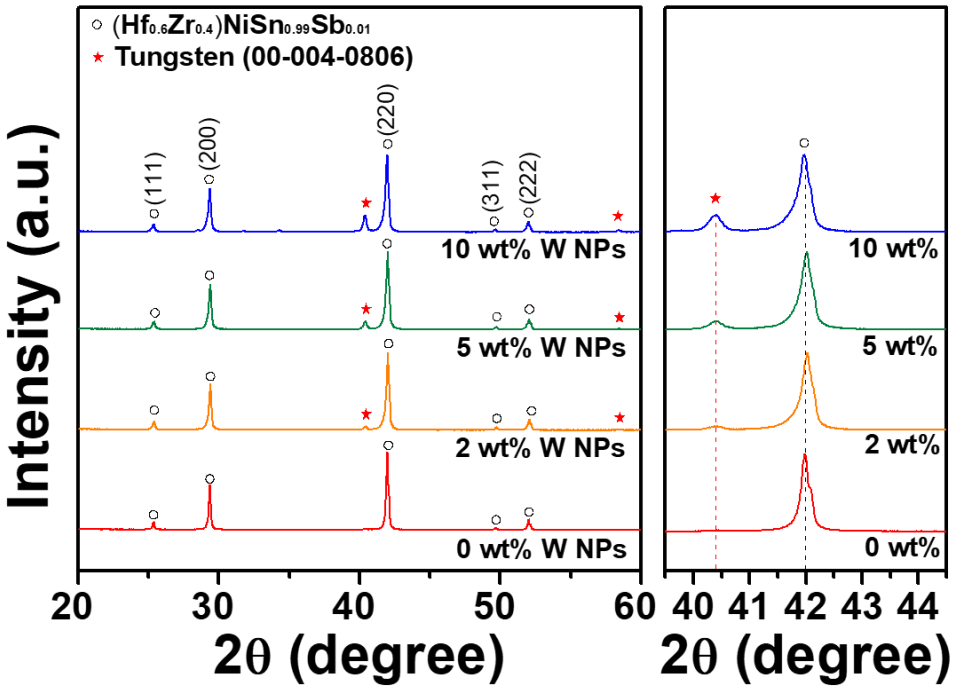

Figure 5.2 X-ray diffraction patterns of $(Hf_{0.6}Zr_{0.4})NiSn_{0.99}Sb_{0.01}$ + *x* wt% W nanocomposite.

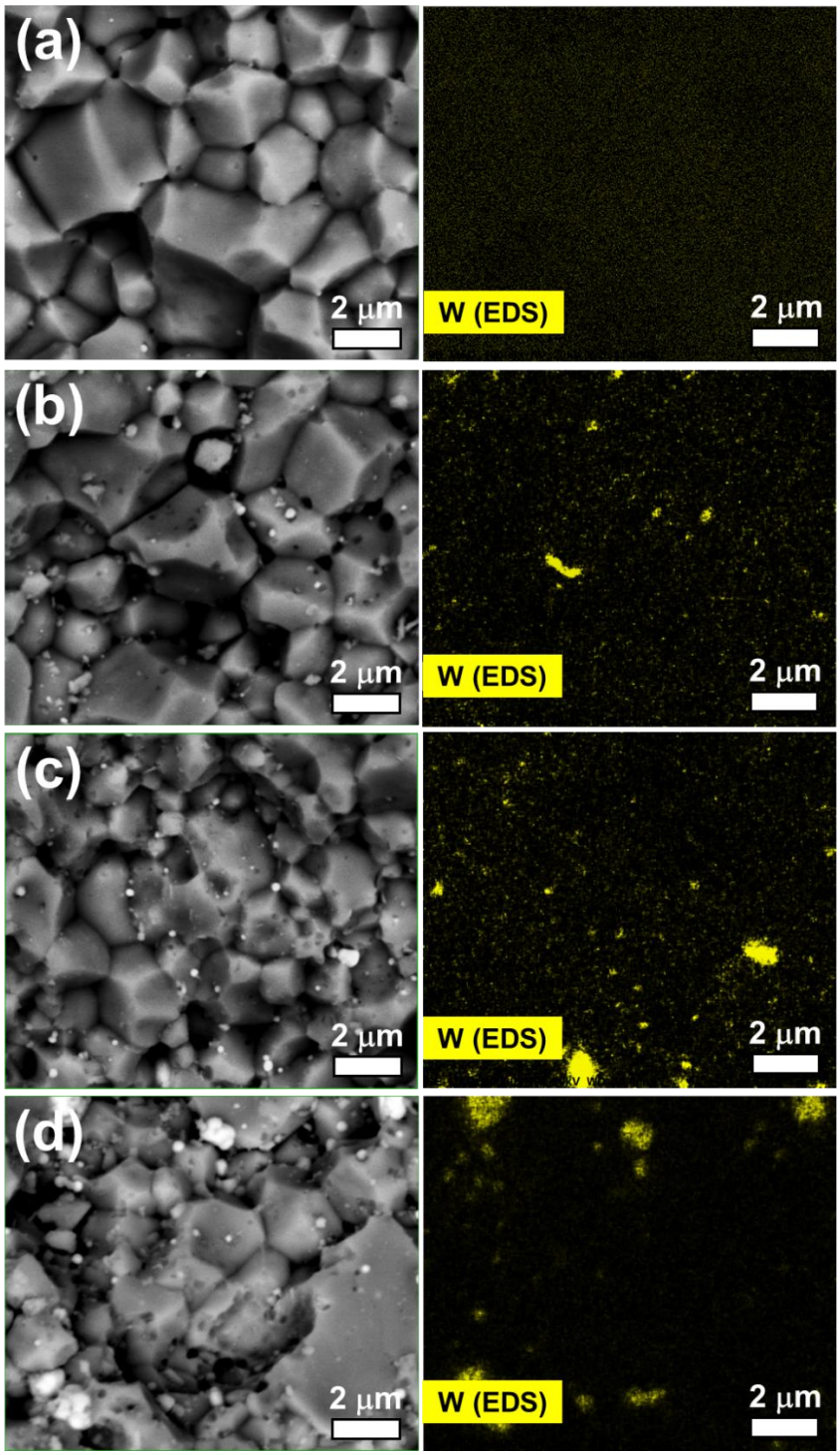

Figure 5.3 SEM Analysis of hH/W nanocomposites. Backscattered electron detector (BSD) for scanning electron microscopy (SEM) (left) and corresponding energy-dispersive X-ray spectroscopy (EDS) of tungsten element (right) of $(Hf_{0.6}Zr_{0.4})NiSn_{0.99}Sb_{0.01}$ + *x* wt% W nanocomposite. (a) *x* = 0 wt%, (b) 2 wt%, (c) 5 wt%, and (d) 10 wt%, respectively.

To probe the nanoscale distribution of tungsten inclusions in the hH matrix, we have performed transmission electron microscopy on a representative sample of $(Hf_{0.6}Zr_{0.4})NiSn_{0.99}Sb_{0.01}$ + 5 wt% W nanocomposite as shown in **Figure 5.4**. The inclusions are mostly located at the vicinity of the grain boundary, which is the preferred site for the precipitation of new phase. The microscopic EDS mapping clearly demonstrates distribution of tungsten nanoparticles in hH matrix (**Fig. 5.4b and c**). The pristine hH matrix has an intrinsic hafnium and hafnium oxide (HfO_2) precipitates resulting from a supersaturation of high melting point of hafnium during the rapid cooling process (**Fig 5.5**). The EDS mapping of pure hH sample in **Figure 5.5** reveals that the nano-sized precipitates (~20 nm) are widely dispersed within the grain and at the grain boundary. It has been reported that the nano-scale Hf-phase precipitates and phase separation are spontaneously induced in the *n*-type hH compounds under rapid cooling/heating condition. A small concentration of oxygen absorbed on the surface of precursors and partial solubility of hafnium in the alloys due to high melting point of the hafnium results in the formation of hafnium and hafnium oxide precipitates during the cooling process [85,86,88,89]. The nanoscale hafnium and HfO_2 precipitates were also observed around the tungsten nanoinclusions (green dots) in the TEM images. The size of Hf-phase is in the range of tens of nanometer as shown in **Figure 5.4c** (green circles). The dimension of the tungsten inclusions is observed in the range from 30 nm to 274 nm and the average inclusion size is found to be 98 nm (**Inset of Fig 5.4c**). The size of Hf-phase precipitates is much smaller than the tungsten inclusions, and the average value is found to be 18 nm. Consequently, we found that the tungsten/*n*-hH nanocomposite comprises of multiple phases with dimensions ranging from tens of nanometer (hafnium/HfO_2) to several hundreds of nanometer (tungsten). This results in enhanced phonon scattering and thereby lower thermal conductivity [42].

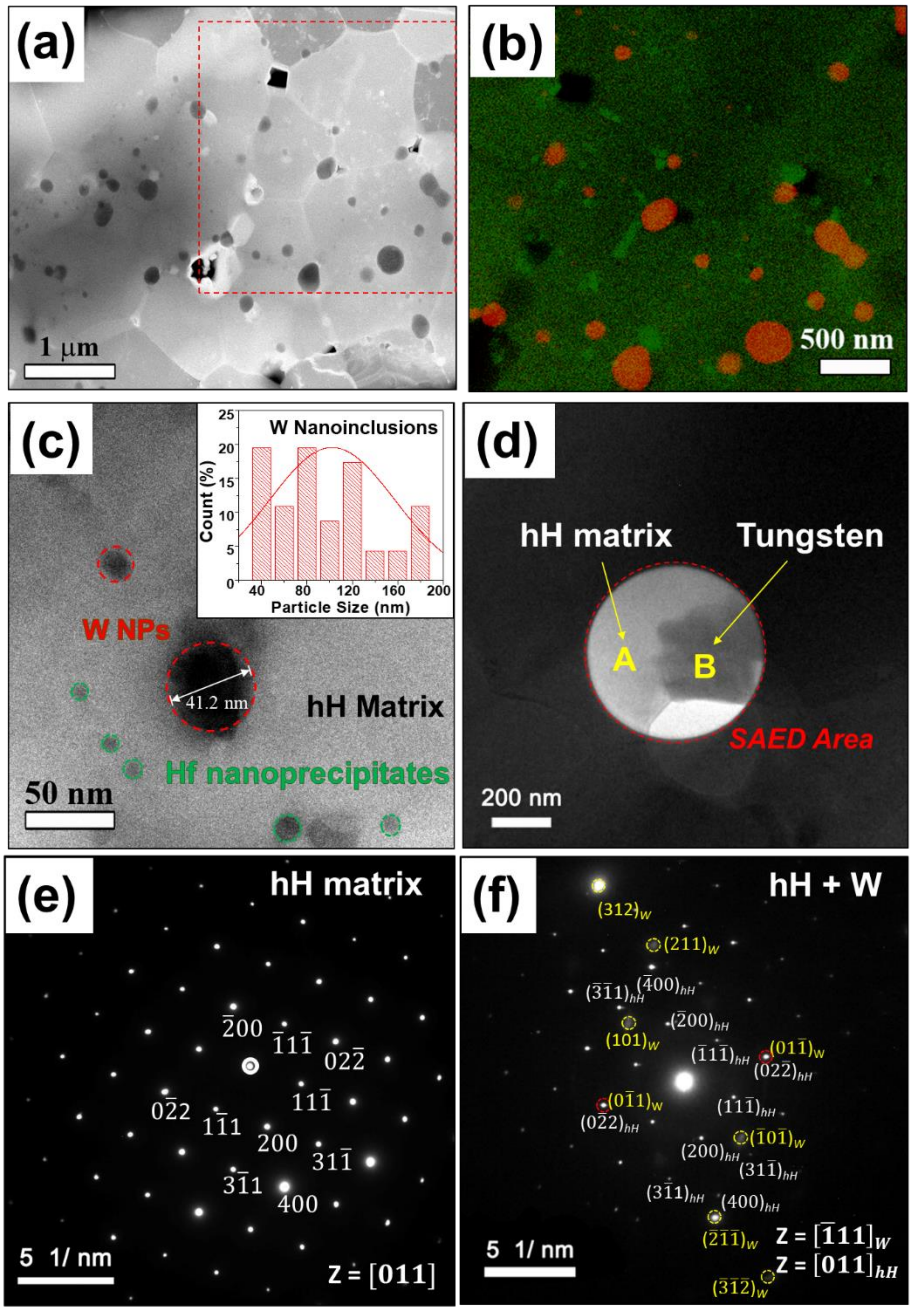

Figure 5.4 Structural characterizations of the hH/W nanocomposites. **(**a) Transmission electron micrograph (TEM) of $(Hf_{0.6}Zr_{0.4})NiSn_{0.99}Sb_{0.01}$ + 5 wt% W nanocomposite. (b) Elemental mapping on the selective area. Red color indicates a tungsten element and green color shows a hafnium element. (c) Enlarged TEM image of the tungsten nanoparticles and histogram of tungsten particle size distribution (inset). (d) The spot of selective area electron diffraction (SAED) for *n*-hH + 5 wt% W nanocomposite. (e and f) SAED patterns of the region A (hH matrix, e), and the region B, respectively (hH matrix and tungsten, f).

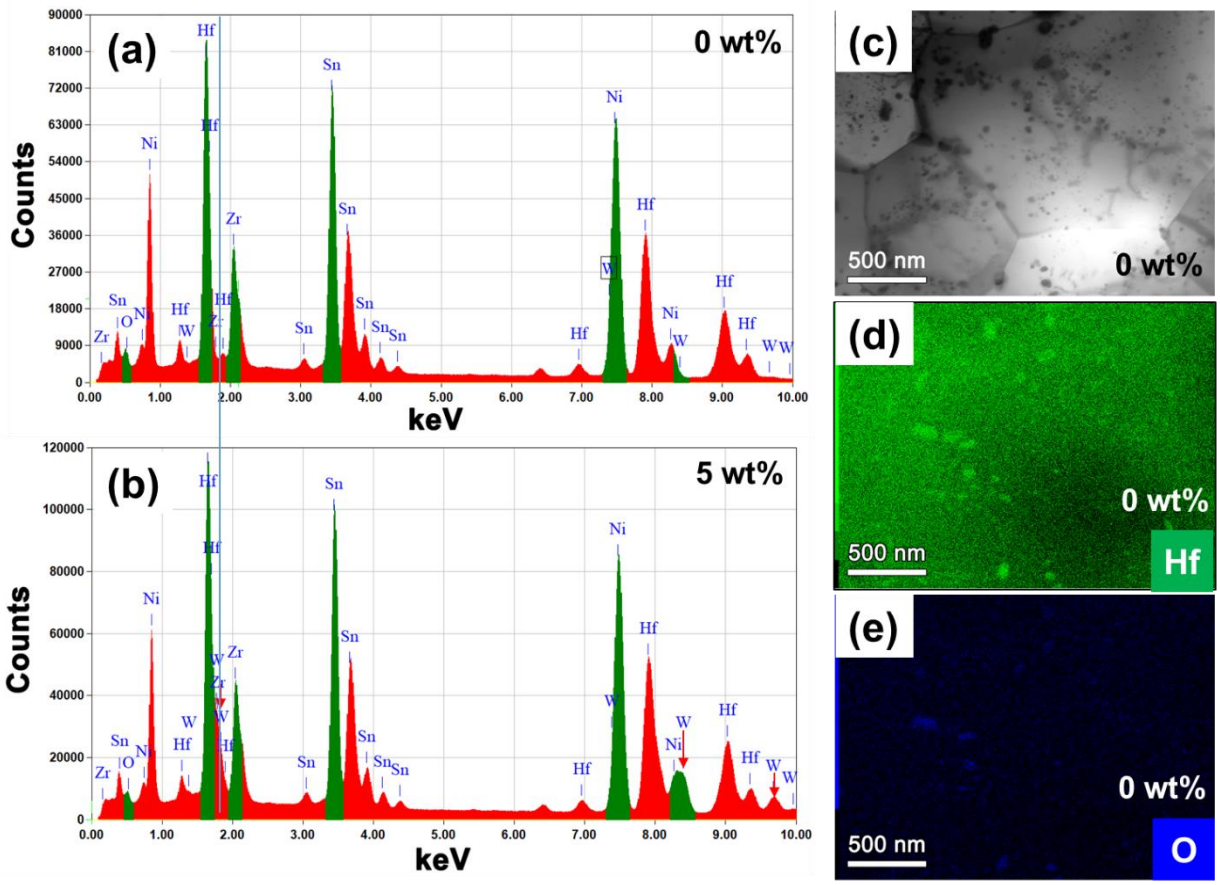

Figure 5.5 TEM EDS analysis in pure hH and nanocomposite. **(**a and b) TEM EDS spectrum of (a) pure hH and (b) 5 wt% W nanocomposite, respectively. Red line indicates the energy spectrum region for tungsten element. (c) TEM bright field image and (d and e) corresponding elemental mapping of pure hH sample. (d) Green color shows a hafnium element and (e) blue color indicates an oxygen content (no detectable spot for a tungsten element in pure hH sample).

Table 5.1 *d*-value mismatch (%) along possible matching planes between hH and tungsten

Matching Plane	*d*-value mismatch (%)	Matching Plane	*d*-value mismatch (%)	Matching Plane	*d*-value mismatch (%)
$(111)_{hH}/(110)_{W}$	57.1	$(200)_{hH}/(110)_{W}$	36.1	$(220)_{hH}/(110)_{W}$	-3.67
$(111)_{hH}/(200)_{W}$	122.0	$(200)_{hH}/(200)_{W}$	92.3	$(220)_{hH}/(200)_{W}$	36.1
$(111)_{hH}/(211)_{W}$	171.8	$(200)_{hH}/(211)_{W}$	135.5	$(220)_{hH}/(211)_{W}$	66.7

The interfacial relationship between hH matrix and tungsten inclusion was investigated using selective area electron diffraction (SAED) as shown in **Figure 5.4d**. We selected two regions that are associated with the pure hH matrix and tungsten nanoinclusions for structural analysis using EDS (marked as A and B in **Fig. 5.4d**). The SAED patterns from each region are shown in **Figure 5.4e and f**, respectively. The hH matrix shows face-centered cubic diffraction pattern (**Fig. 5.4e**) and additional diffraction spots with body-centered cubic symmetry corresponding to tungsten inclusion (**Fig. 5.4f**), which are marked as yellow circle. The $(Hf_{0.6}Zr_{0.4})NiSn_{0.99}Sb_{0.01}$ hH alloy has a space group of $F\bar{4}3m$ with a lattice constant of 6.077 Å. Tungsten has a space group of $Im\bar{3}m$ with a lattice constant of 3.165 Å. Thus, the new phase tends to form a partially coherent interface with matrix with a specific crystallographic orientation relationship that minimizes misfit energy of the system. For hH (*fcc* structure), there are three close-packed planes, $(111)_{hH}$, $(200)_{hH}$, and $(220)_{hH}$. The close-packed plane for tungsten (*bcc* structure) are $(110)_W$, $(200)_W$, and $(211)_W$, opening nine possibilities for presence of matching interface between hH and tungsten [90]. The *d*-value mismatch ($\delta = (d_\beta - d_\alpha)/d_\alpha$) between the nine possible plane pairs are listed in **Table 5.1**. The pair corresponding to $(220)_{hH}$ and $(110)_W$ plane shows the smallest mismatch of -3.67 % and the *d*-value mismatch in all the other plane pairs is greater than a critical mismatch of 6 % [90]. The SAED pattern reveals the matching along $(0\bar{1}1)_W$ and $(0\bar{2}2)_{hH}$ planes marked as red circle in Figure **5.4f**. This indicates that tungsten inclusions are incorporated in the hH matrix with a semi-coherent interface that results in lowering of the Gibbs energy.

5.3 Outstanding improvement in PF with electron injection and energy filtering effect

The temperature dependence of electronic transport properties of all the nanocomposites are shown in **Figure 5.6**. The electrical conductivity of hH alloy varied as a function of tungsten concentration. It gradually increased from 1.18×10^5 S·m^{-1} for *n*-hH to 1.51×10^5 S·m^{-1} for *n*-hH/5 wt% W composites and reached to 1.96×10^5 S·m^{-1} for *n*-hH/10 wt% W composite at 300 K, resulting in 65% enhancement. This enhancement is caused by the increase in carrier concentration due to the presence of metallic tungsten nanoparticles. It has been demonstrated that metallic nanoparticle inclusions can be more effective in adding electrons to the conduction band in *n*-type semiconductor compared to dopants [80]. **Table 5.2** shows that the carrier concentration and mobility vary with tungsten inclusions. The Hall resistivity used to obtain the data in **Table 5.2** also indicates single-carrier electronic conduction. The carrier concentration almost doubles with 10 wt% tungsten inclusion compared to pure *n*-hH. This provides evidence of the electron injection from metallic tungsten nanoparticles in to the semiconductor hH matrix, resulting in increased electrical conductivity. Interestingly, only minor changes are observed in the Seebeck coefficient with relatively low concentration of tungsten inclusions of 2 and 5 wt%. On the contrary a large drop is present at a high concentration of 10 wt% tungsten inclusion as represented in **Figure 5.6b**. The Seebeck coefficient can be defined by Mott formula as [41,91]:

$$S = \frac{\pi^2}{3}\frac{k_B}{q}k_B T\left\{\frac{1}{n}\frac{dn(E)}{dE} + \frac{1}{\mu}\frac{d\mu(E)}{dE}\right\}_{E=E_F} \quad (5.1)$$

where k_B is Boltzmann's constant, q is the carrier charge, E_F is the Fermi energy, $n(E)$ and $\mu(E)$ are the density and mobility of carrier at energy E, respectively.

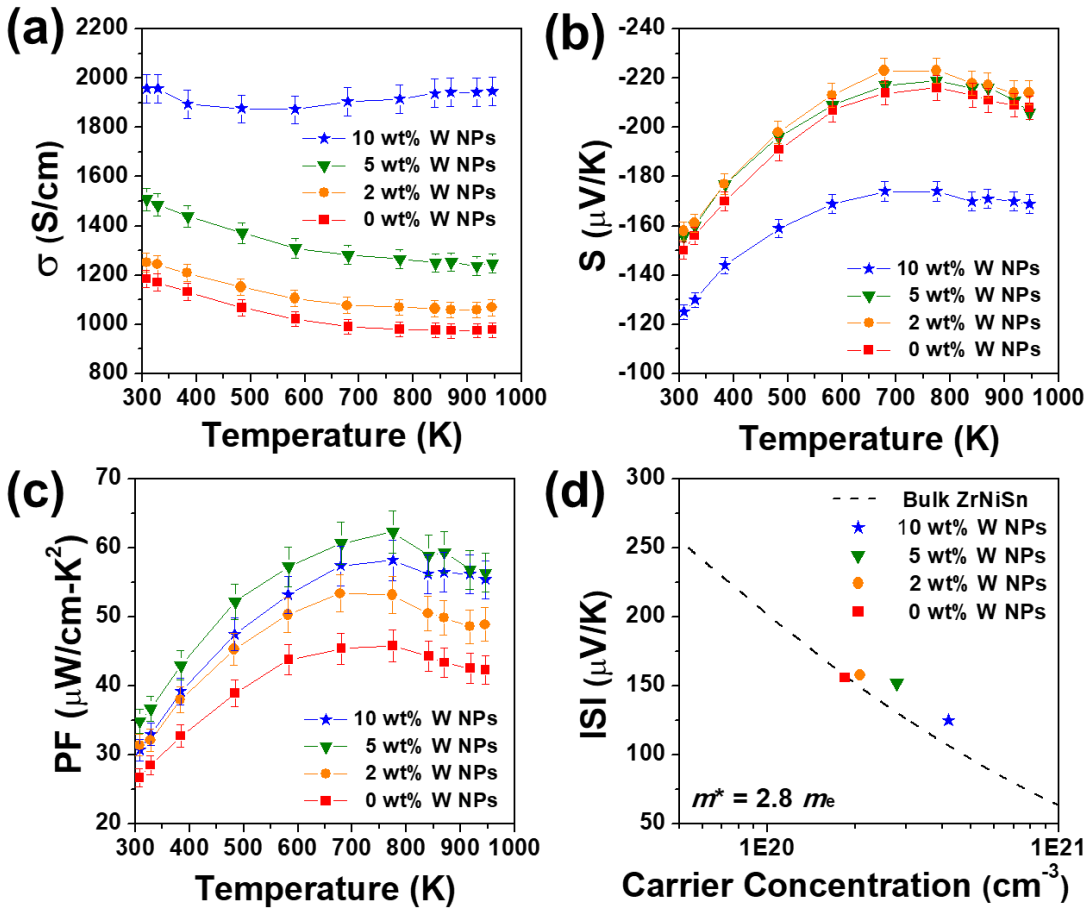

Figure 5.6 Electronic transport properties of hH/W nanocomposites. (a) Temperature dependence of electrical conductivity, (b) Seebeck coefficient, and (c) power factor as a function of tungsten concentration, respectively. (d) Carrier concentration dependence of Seebeck coefficient at room temperature.

Table 5.2 Room temperature carrier (electron) concentration and mobility of $(Hf_{0.6}Zr_{0.4})NiSn_{0.99}Sb_{0.01}$ + *x* wt% W nanocomposites

Samples	S (μV/K)	Carrier Concentration ($x10^{19}cm^{-3}$)	Carrier Mobility ($cm^2V^{-1}s^{-1}$)
***x* = 0 wt%**	-156	18.52	40.60
***x* = 2 wt%**	-158	20.79	36.70
***x* = 5 wt%**	-152	27.85	28.87
***x* = 10 wt%**	-125	41.82	26.83

From the **Equation 5.1**, the Seebeck coefficient depends on the energy derivative of carrier density and mobility. It indicates that higher Seebeck coefficient can be achieved by both a sharp modulation in the carrier density of states (DOS) near E_F (increase in $dn(E)/dE$) and the energy filtering effect that selectively scatters low energy charge carriers (higher $d\mu(E)/dE$) [6,41]. **Figure 5.6d** shows the carrier concentration dependence of the Seebeck coefficient at room temperature. The dashed line represents the calculated Seebeck coefficient of bulk ZrNiSn alloy, derived from a single Kane band (SKB) model with the DOS effective mass $m^* = 2.8\ m_e$ [12]. Our *n*-type hH alloy shows good agreement with the calculated value on the dashed line. It is noteworthy that the introduction of nanoinclusions in hH matrix results in deviation from the calculated bulk ZrNiSn values, showing higher Seebeck coefficient at a given carrier concentration. This provides strong evidence of the energy filtering effect that results in enhanced Seebeck coefficient by increasing $d\mu(E)/dE$ in the **Equation 5.1**. The power factor ($S^2\sigma$) was significantly enhanced by introducing tungsten nanoinclusions into the hH matrix (**Fig. 5.6c**). The maximum power factor reached 62.3 $\mu W \cdot cm^{-1}K^{-1}$ at 773 K for 5 wt% W/*n*-hH nanocomposite, which is a 36% improvement compared to pure *n*-hH. It is attributed to both an increase of the electrical conductivity by charge carrier injection from metallic tungsten nanoinclusions, and the relatively higher Seebeck coefficient at the given carrier concentration by energy filtering effect.

5.4 Thermal conductivity reduction in *n*-hH/W nanocomposite

The thermal conductivity (κ) of the nanocomposite was calculated from the measured density (ρ), specific heat capacity (C_P), and thermal diffusivity using equation $\kappa = \rho\ C_P\ \alpha$. As shown in **Figure 5.7a**, the specific heat capacity of the nanocomposites decreases on increasing tungsten concentration, due to the contribution of lower specific heat capacity of tungsten ($0.132\ J \cdot g^{-1}K^{-1}$).

In the case of an isotropic composite with no local stress or strain, the specific heat capacity of the composite can be expressed using mixing rule:

$$C_p = x_1 C_{p1} + x_2 C_{p2} + \cdots + x_n C_{pn} = \sum x_k C_{pk} \quad (5.2)$$

where $x_k = m_k/m$ is mass fraction, and C_{pk} is a specific heat capacity of component *k*.

The calculated C_p values for each sample of *n*-hH/W nanocomposites are illustrated as dotted line in **Figure 5.7a**. The measured specific heat capacity shows a good correlation according to **Equation 5.2** except in the lower temperature region. Thus, the intrinsic low specific heat capacity of tungsten can contribute towards decrement of thermal conductivity of the composite, independent of the scattering effect of the inclusions. The total thermal conductivity of *n*-hH/W nanocomposites was effectively reduced by adding tungsten nanoparticles as shown in **Figure 5.7b**. It should be noted that high concentration of tungsten inclusions is not beneficial in decreasing thermal conductivity because a large contribution of electrical thermal conductivity arising from higher carrier concentration offsets the effect of enhanced phonon scattering by nanoinclusions. To clarify the influence of nanoinclusions on the thermal transport by phonon scattering, we derived lattice thermal conductivity (κ_{lat}) by subtracting the electronic component κ_e from the total thermal conductivity κ_{tot} ($\kappa_{lat} = \kappa_e - \kappa_{tot}$). The electronic contribution (κ_e) can be estimated by Wiedemann-Franz law as **Equation (1.12)**. Here the Lorenz number is calculated by the SKB model incorporating multiple scattering mechanisms of ZrNiSn based hH alloys [12,24].

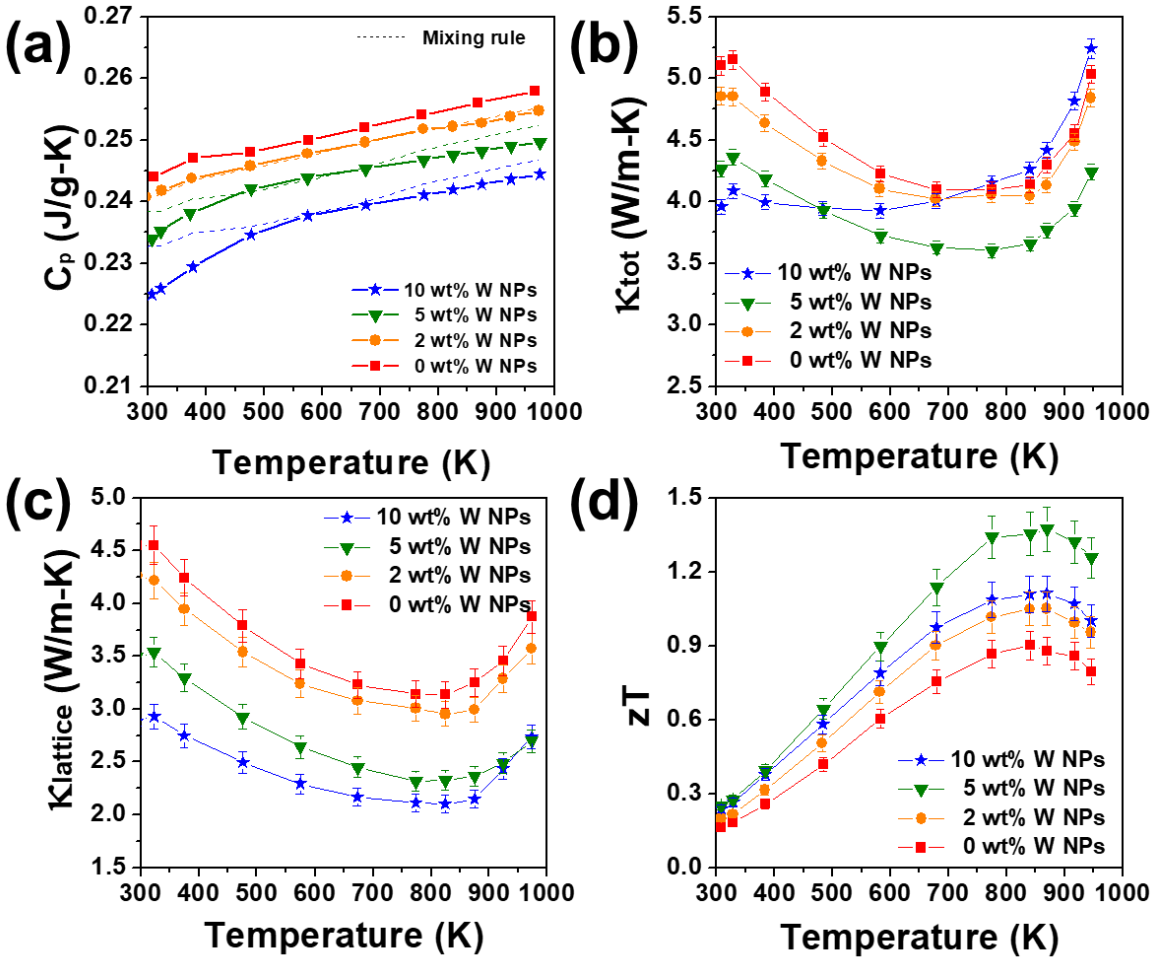

Figure 5.7 Thermal transport properties of hH/W nanocomposites. (a) Temperature dependence of total thermal conductivity, (b) lattice thermal conductivity ($\kappa_{lattice}$) derived by subtracting an electronic component (κ_e) from the κ_{tot}, (c) specific heat capacity and (d) figure of merit zT, respectively.

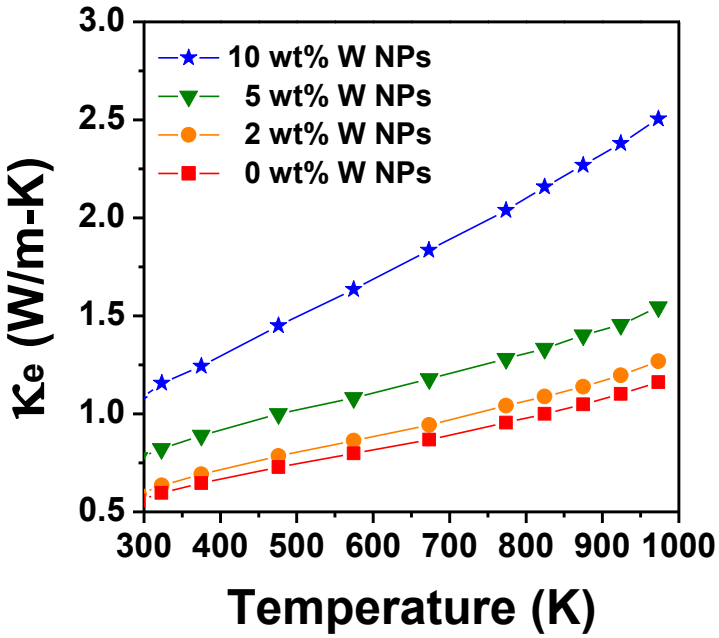

Figure 5.8 Electronic component of thermal conductivity. Temperature dependence of electronic thermal conductivity. The values are calculated by Wiedemann-Franz law.

The electronic contribution of the thermal conductivity becomes comparable with the lattice thermal conductivity when the tungsten fraction is sufficiently high (**Fig. 5.8**). **Figure 5.7c** presents the temperature dependence of the lattice thermal conductivity of *n*-hH/W nanocomposites. The lattice thermal conductivity was effectively suppressed by the addition of tungsten nanoparticles. Higher concentrations of tungsten inclusions showed lower lattice thermal conductivity, indicating the increase of phonon scattering. For example, a room temperature value of $\kappa_{lat} \approx 4.55$ W·m^{-1}K^{-1} was greatly decreased to 2.93 W·m^{-1}K^{-1} in the 10 wt% tungsten inclusion sample, a change of 35%. The reduction of lattice thermal conductivity via tungsten inclusions was observed over a wide temperature range. Next, we discuss mechanisms that contribute to the lower lattice thermal conductivity in the presence of tungsten inclusions.

Table 5.3 Comparison of the acoustic impedance in three mediums of $(Hf_{0.6}Zr_{0.4})NiSn_{0.99}Sb_{0.01}$ (*n*-hH), hafnium, hafnium oxide (HfO_2) and tungsten according to their density and speed of sound

Materials	**Density ($g \cdot cm^{-3}$)**	**Speed of sound ($m \cdot s^{-1}$)**	**Acoustic Impedance ($10^7\ kg \cdot m^{-2}s^{-1}$)**
n-hH	9.37	3367	3.16
Hafnium	13.31	3010	4.01
HfO_2	9.68	5405	5.23
Tungsten	19.3	5174	9.99

A large acoustic impedance mismatch between a semiconductor and a metal leads to a high effective interface phonon scattering [92]. The acoustic impedance (Z) of a material is defined as the product of the density (ρ) and the speed (c) of the sound waves traveling in the medium:

$$Z = \rho c \tag{5.3}$$

Since the hH semiconductor matrix and the tungsten metal particles have a significant difference in both the density (ρ_{hH} = 9.37 $g \cdot cm^{-3}$and ρ_W = 19.3 $g \cdot cm^{-3}$) and the speed of sound (c_{hH} = 3367 $m \cdot s^{-1}$ [93], and c_W = 5174 $m \cdot s^{-1}$), there is a large acoustic impedance mismatch between $Z_{hH} = 3.16 \times 10^7\ kg \cdot m^{-2}s^{-1}$ and $Z_W = 9.99 \times 10^7\ kg \cdot m^{-2}s\text{-}^{1}$. However, hafnium shows similar acoustic impedance ($Z_{Hf} = 4.01x10^7\ kg \cdot m^{-2}s^{-1}$) as that of hH matrix. Further, hafnium oxide has relatively small difference in acoustic impedance ($Z_{HfO2} = 5.23x10^7\ kg \cdot m^{-2}s^{-1}$) as shown in **Table 5.3**. This indicates that the interfacial phonon scattering can be more predominant for tungsten inclusions rather than hafnium or hafnium oxide, and thus the lattice thermal conductivity is substantially decreased by increasing the interfaces with tungsten.

A multiphase nanostructure with varying length-scales was developed through mixture of hafnium/HfO_2 precipitates, tungsten inclusions, and mesoscale grains of hH matrix. This type of microstructure can further contribute to an additional reduction in lattice thermal conductivity by

inducing integrated phonon scattering across multiple length scales. For example, phonons with short and medium mean free paths of less than 100 nm can be scattered by both hafnium/HfO_2 precipitates and tungsten inclusions. Mesoscale grain structure can contribute to scattering of heat-carrying phonons with longer mean free path. Biswas *et al.* [42] have shown that phonon scattering is more effective by designing hierarchical architectures in *p*-type PbTe-SrTe doped with 2 mol% sodium. Jian *et al.* [94] have also reported outstanding thermoelectric performance in *n*-type PbTe by inducing a multiphase nanostructure via In, Sb, Pb, and InSb nanoprecipitates. These prior results match our findings and confirm the effectiveness of multiphase multi-length microstructures.

5.5 Outstanding figure-of-merit (zT) in nanocomposite

Simultaneous improvement in the power factor and reduction in thermal conductivity boost the figure of merit (zT) in entire temperature region, as represented in **Figure 5.7d**. The maximum zT value reached to ~1.4 at 873 K with 5 wt% tungsten inclusion into the *n*-type hH matrix, 55% improvement compared to hH sample (zT_{max} ~0.9 at 823K). More importantly, the results show that the zT value is improved over a broad temperature range from 773 K to 923 K. The average zT in the temperature range of 573 K to 973 K increases from ~0.78 to ~1.20 through incorporation of 5 wt% tungsten inclusions. As shown in **Figure 5.1b**, this is a remarkable improvement compared to current state-of-art *n*-type hH alloys, such as the $Ti_{0.5}Hf_{0.5}NiSn_{0.98}Sb_{0.02}$ alloy with atomic-scale defect disorders (zT= 1.09 ± 0.12 at 800K) [46], the Hf and Nb alloying in $(Hf_{0.25}Zr_{0.75})NiSn_{0.99}Sb_{0.01}$ and $(Zr_{0.4}Hf_{0.6})_{0.88}Nb_{0.12}CoSb$ compounds with zT of ~1.0 at 1000 K [44,47], and nanostructured $(Hf_{0.75}Zr_{0.25})NiSn_{0.99}Sb_{0.01}$ compounds (zT ~ 1.0 at 873 K) [17]. It is noteworthy that the zT improvement in our multi-phase nanocomposites is attributed to a supplementary advantage of tungsten nanoinclusion in addition to the various strategies

demonstrate for the hH alloys. This implies that the multi-scale nanocomposite technique demonstrated here can be extended to other thermoelectric materials that have been optimized by atomic and nanoscale modifications to further enhance TE performance.

5.6 Conclusion

We demonstrate high thermoelectric performance of *n*-type hH alloy through incorporation of tungsten nanoinclusions. A multiphase multi-length-scale microstructure comprising of hafnium/HfO_2 nanoprecipitates, tungsten nanoinclusions, and mesoscale hH grains was found to be highly effective in enhancing the phonon scattering. Reduction in lattice thermal conductivity was induced by large acoustic impedance mismatch between the tungsten and hH matrix and multiple nanophase architecture. The metallic tungsten injects electrons in to the host hH semiconductor which increases electrical conductivity. Higher Seebeck coefficient was achieved for given carrier concentration by energy filtering effect at the interfaces between metal inclusions and semiconductor matrix. As a result, an outstanding maximum zT of ~1.4 at 873 K and average zT of ~1.2 in the temperature range of 573-973 K were achieved for hH alloy with 5 wt% tungsten nanoinclusions.

Chapter 6 High temperature air stability of half-Heusler alloys for thermoelectric energy harvesting

6.1 Introduction

In an exergy content (Carnot's potential) estimation, high temperature heat provides greater work potential due to higher quality of the thermal energy [5]. However, utilization of the high temperature thermal energy has been challenging due to concerns related to stability and sustainability of materials under the intense thermal stress. The elevated temperature leads to higher reactivity of materials and makes them fragile and sensitive to the environment. In particular, it is critical for a TE power generator to sustain the output performance for a long period of time.

Most of the high performance TE materials are metallic alloys that become more air sensitive at higher temperatures. Thus, a TE device generally requires vacuum sealing and packaging to protect materials from oxidation. The weak thermal stability of TE material in air at higher temperatures often limits their application. While half-Heusler alloy has been gaining attention for medium to high temperature application, there is a lack of systematic study in evaluating its thermal stability under realistic operating temperatures. Prior to applying the hH materials into practical TEG device, a basic understanding of the material stability is required to determine the safe working conditions.

In this chapter, we have investigated the high temperature thermal stability of hH compounds in air condition using dynamic and steady state thermal analysis. Four different compositions were examined to identify most stable and sustainable ones. The results provided in this chapter will guide the design of hH alloy based thermoelectric generator and its output performance.

6.2 Dynamic thermal analysis for hH alloys at elevated temperatures

The overview of thermal stability for hH compounds was demonstrated by a dynamic thermal analysis. Here, *n*-type $(Hf_{0.6}Zr_{0.4})NiSn_{0.99}Sb_{0.01}$ (labeled as "*n*-hH") and *p*-type first generation $(Hf_{0.5}Zr_{0.5})CoSb_{0.8}Sn_{0.2}$ compounds (labeled as "*p*-hH 1G") were selected to study the durability of the materials under high temperatures with a high heating rate of 10 K/min. **Figure 6.1** shows thermogravimetry (TGA) and differential scanning calorimetry (DSC) results on *n*-hH and *p*-hH 1G alloys under the inert gas (argon) atmosphere and air environment. Under the argon atmosphere (black lines), both hH alloys exhibit no mass change in TGA curves and no distinct exothermic peaks in DSC curves with increase of temperature. It indicates that the hH alloys do not undergo any phase transformation and thermal decomposition in the argon atmosphere up to 923 K. Moreover, *n*-type hH displays almost identical trends in TGA and DSC under the ambient air condition in contrast to *p*-hH 1G alloy. The weight of *p*-type 1G hH alloy increases above 723 K in air condition as shown in **Figure 6.1b** (blue solid line). The weight gain continues to occur with the increase of temperature and reaches 0.1 % at 923 K. The absolute weight gain is quite small because the dynamic measurement with the high heating rate can limit a diffusion-controlled oxidation reaction, resulting in partial surface oxidation of the material. There is a striking contrast with the inert gas condition, which indicates that a reasonable amount of oxidation has occurred at the surface. The local oxidation that only takes place at the surface level implies minimization of the surface contact and the diffusion process would be effective way to reduce the oxidation rate and improve the material stability at the given temperature.

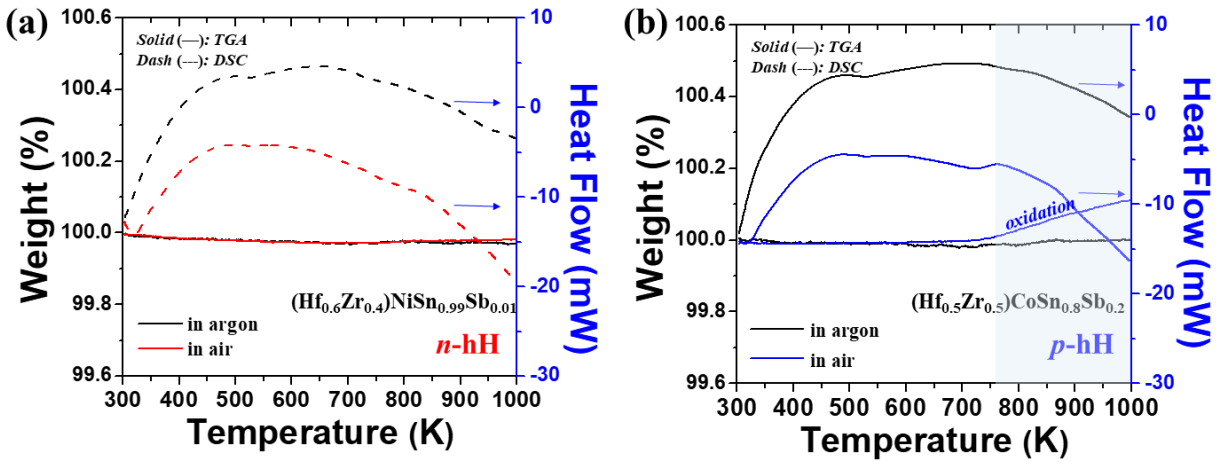

Figure 6.1 TGA-DSC plots of (a) *n*-hH and (b) *p*-hH 1G compounds under two different environments of inert gas (argon) and air.

In order to further verify the oxide phase formation at elevated temperature, in-situ XRD with isothermal heating was conducted on two samples as represented in **Figure 6.2**. The diffraction patterns were collected at eight different temperatures (T = 300, 573, 673, 773, 798, 823, 848, and 873 K) while applying isothermal temperature on the sample. The set temperature was held for 40 minutes while taking the in-situ *X*-ray diffraction. Data was continuously recorded up to 873 K. Both hH alloys are stable below 673 K in air, but a distinct difference in thermal stability occurs above 773 K. In contrast to *n*-hH compound, *p*-hH 1G shows a stronger secondary phase formation involving HfO_2, ZrO_2, SnO_2, $Sb2O_5$, and CoSb phases. The diffraction intensity of hH phase is significantly decreased by increasing temperature, indicating that there is a thicker oxide layer forming at surface. In case of *n*-hH phase, diffraction pattern is maintained up to 873 K although the intensity decreases with the increase of temperature. This implies that the oxidation of *n*-hH at the surface is weaker than that of *p*-hH 1G alloy under the same condition. Overall, *n*-hH alloy illustrates better air stability compared to that of *p*-hH 1G alloy at high temperature.

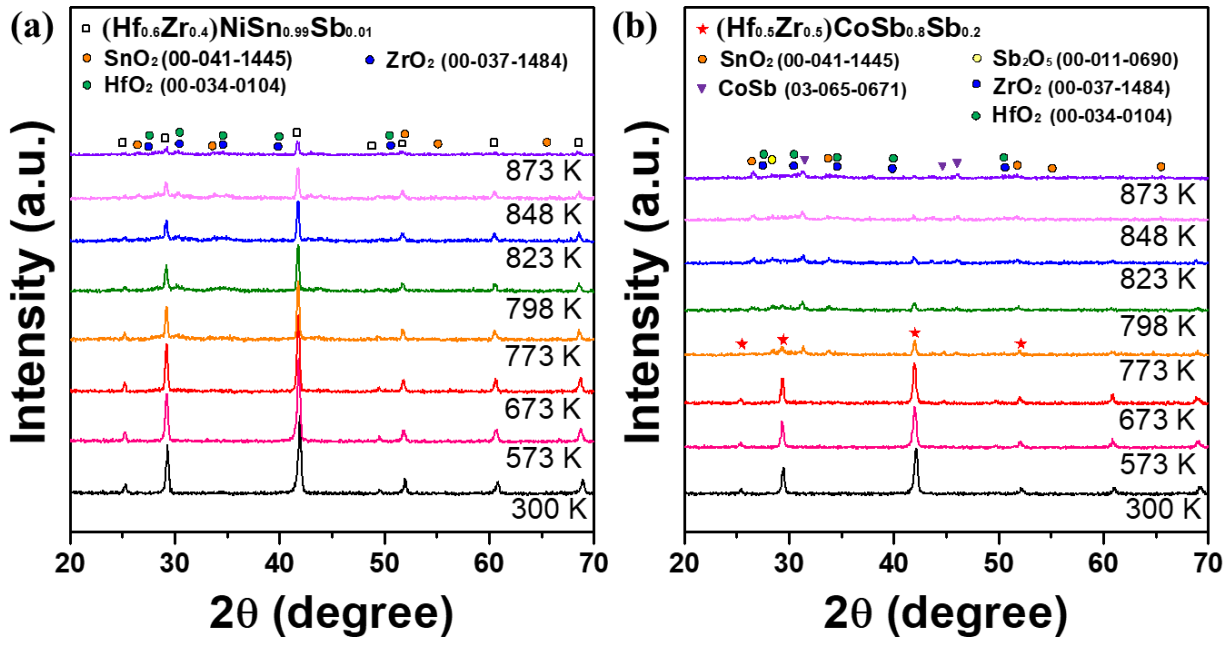

Figure 6.2 In-situ XRD with isothermal heating at eight different temperature (300, 573, 673, 773, 798, 823, 848, and 873 K) for (a) *n*-hH and (b) *p*-hH 1G alloys in air.

6.3 Steady state thermal analysis for hH alloys under isothermal temperature

In the dynamic thermal analysis, kinetic control of reaction is somewhat restricted due to the short duration time of heating. Therefore, a steady-state thermal analysis was conducted that applies isothermal heating for a long time. This provides deeper understanding of the oxidation reaction in hH alloys at high temperatures in air. The experimental procedure for this analysis is described in *section 2.3* and **Figure 2.3**.

Figure 6.3 shows XRD results on the annealed *n*-type and *p*-type 1G hH compounds at 823 K for 24 and 72 hours in air. For both compositions, no visible hH phase can be observed indicating that the oxide layer is thick enough to block the *X*-ray penetration into the bulk level. Two samples display a similar oxide phase formation involving major peaks of SnO_2 with HfO_2 and ZrO_2.

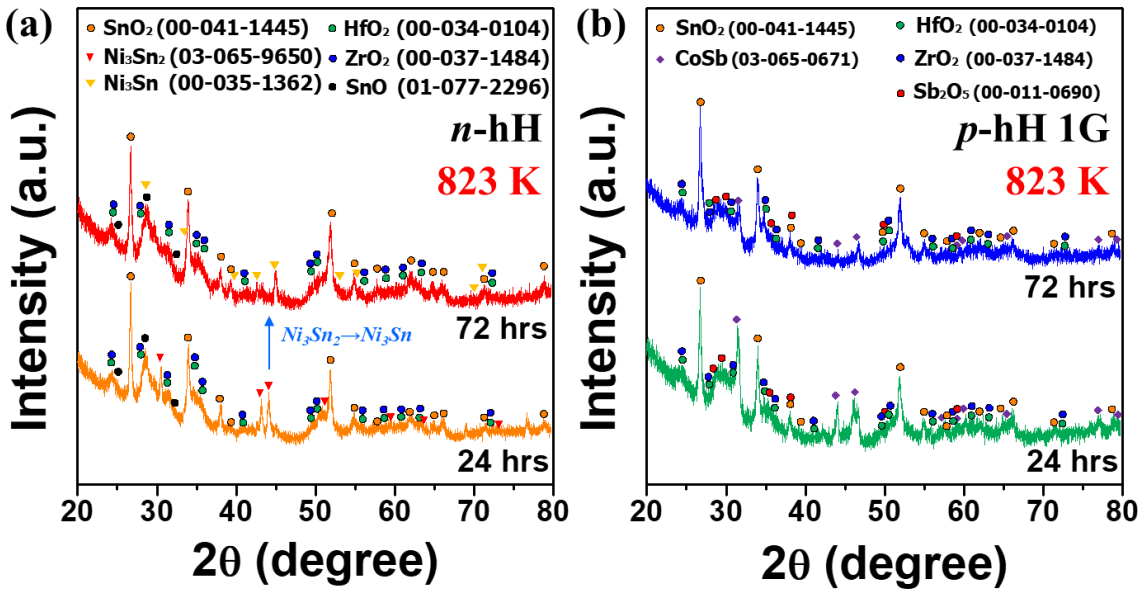

Figure 6.3 X-ray diffraction patterns of (a) *n*-type hH and (b) *p*-type hH 1G annealed at 823 K for 24 hours and 72 hours.

The oxide phase formation leads to other secondary phase such as Ni_3Sn and Ni_3Sn_2 for *n*-hH and CoSb for *p*-hH 1G. Based on theoretical calculation by Berche and Juned [95], an incorporation of oxygen into hH TiNiSn matrix partially decomposes the hH phase into Ti_2O_3 and Ni_3Sn phases. This implies that a partial oxidation of M-site element in MNiSn system induces the Ni-Sn secondary phase formation such as Ni_3Sn, Ni_3Sn_2, and Ni_3Sn_4 by thermodynamic control. Here the coexistence of HfO_2/ZrO_2 phases and nickel stannides (Ni_3Sn and Ni_3Sn_2) can be observed in the annealed *n*-hH sample at 823 K. By increasing time, the Ni_3Sn_2 phase was transformed to Ni_3Sn phase possibly due to the SnO_2 phase formation. **Figure 6.4** represents the cross-sectional BSED-SEM images of annealed *n*-hH samples with EDS mapping of elements. It is clear that the oxide phase such as HfO_2, ZrO_2, and SnO_2 are formed on the outer sides and Ni-Sn phase is observed just below the oxide layers, which is accordance with the reported results by Galazka *et al.* [96]. The longer annealing time increases the oxide thickness from ~10 μm to ~20 μm as shown in **Figure 6.4a and b**.

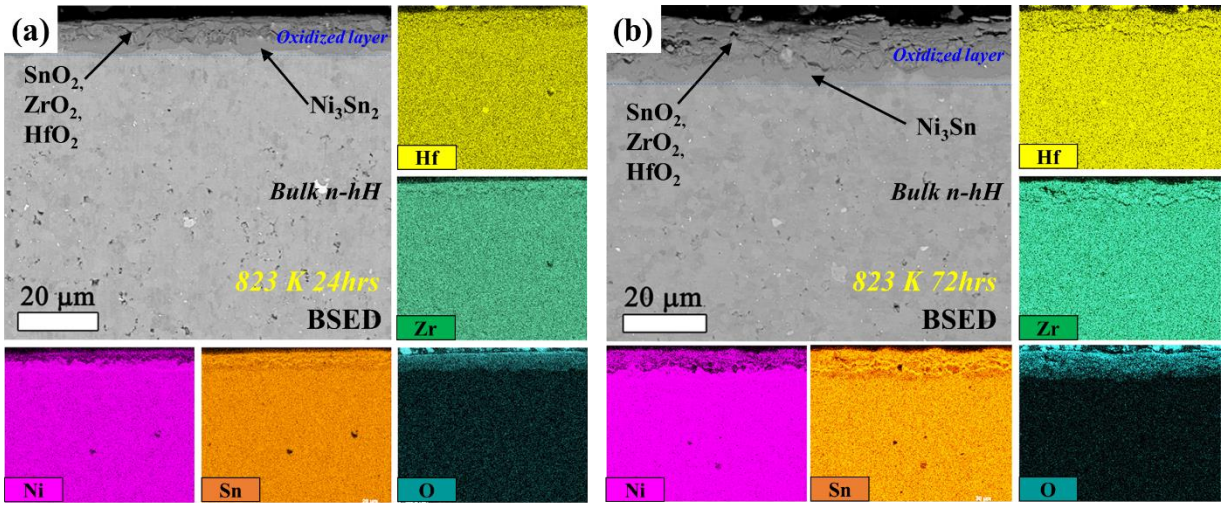

Figure 6.4 Cross-sectional BSED-SEM images of annealed *n*-type hH samples at 823 K with elemental EDS mapping according to the annealing time (a) 24 hours, and (b) 72 hours.

Interestingly, *p*-type 1G hH also presents similar phase formation involving the oxide phases of HfO_2, ZrO_2, SnO_2, Sb_2O_5, and CoSb secondary phase. However, the oxidation reaction is more severe than that of *n*-hH as shown in **Figure 6.5**. In shorter duration of 24 hours (**Fig. 6.5a**), the oxide thickness is comparably small (~10 μm). However, the thickness of oxide layer notably increases to ~65 μm by increasing time to 72 hours as displayed in **Figure 6.5b**. Despite relatively small fraction of Sn (0.2 at%), SnO_2 phase peak is observed in XRD and strong elemental concentration of Sn beneath the surface is observed. It is attributed to Sn segregation on the surface. Basically surface segregation and atomic ordering in alloy is driven by minimizing the surface energy [97,98]. **Table 7.1** lists the surface energy of the elements that comprise of the hH alloys. Tin and antimony have considerably lower surface energy (~0.7 and ~0.6 $J \cdot m^{-2}$) than other elements (>2.0 $J \cdot m^{-2}$) which can be one of driving force for the segregation by heating [98]. Moreover, Sn has much lower ionization energy (708.6 kJ/mol) compared to that of Sb (834 kJ/mol), resulting in a preferable oxidation reaction.

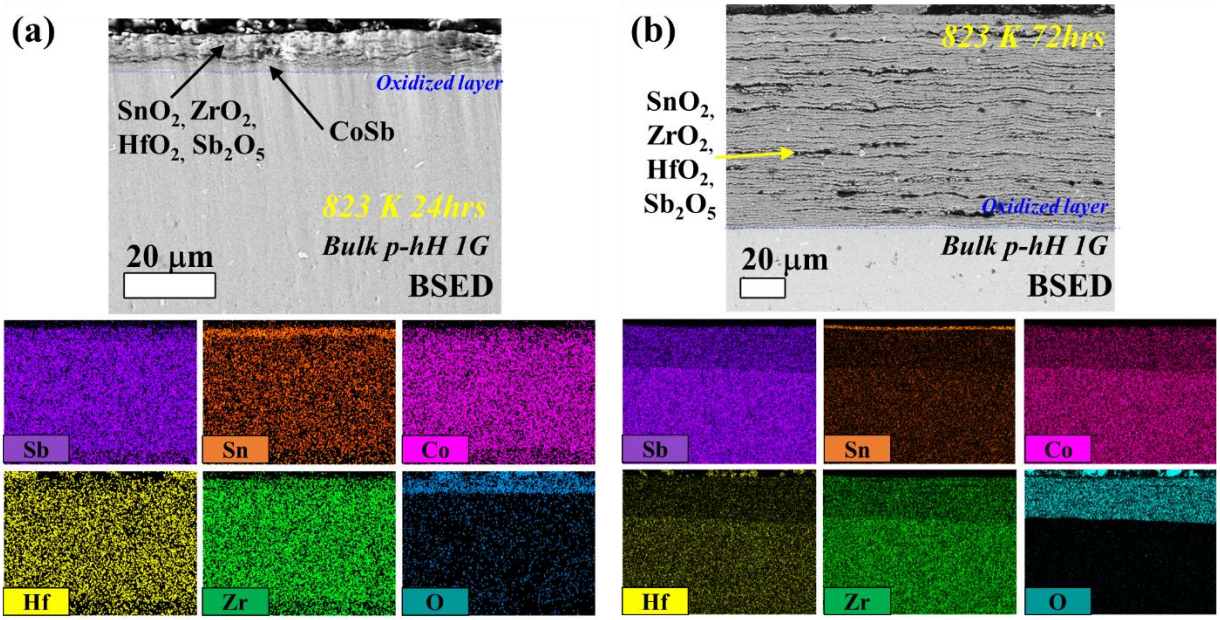

Figure 6.5 Cross-sectional BSED-SEM images of annealed *p*-type 1G hH samples at 823 K with elemental EDS mappings according to the annealing time (a) 24 hours, and (b) 72 hours.

Table 6.1 List of surface energy and first ionization energy for different elements present in the hH MNiSn and MCoSb compounds [99]

Elements	**Hf**	**Zr**	**Ti**	**Ni**	**Co**	**Sn**	**Sb**
Surface energy ($J \cdot m^{-2}$)	2.193, 2.150	1.909, 2.000	1.989, 2.100	2.380, 2.450	2.552, 2.550	0.709, 0.675	0.597, 0.535
1st ionization energy ($kJ \cdot mol^{-1}$)	658.5	640.1	658.8	737.1	760.4	708.6	834

The surface oxidation can affect thermoelectric properties of hH alloys. **Figure 6.6** displays the electrical property variation in long-term annealed *n*-hH and *p*-hH 1G compounds. As shown in the SEM images of **Figure 6.4 and 6.5**, the oxidation basically occurs at the surface. The overall electrical property does not change significantly when the penetration of oxidized layer is limited (<20 μm). The long-time annealed *n*-hH samples show stable performance in both electrical resistivity and Seebeck coefficient. On the contrary, 72 hours annealed *p*-hH 1G alloy

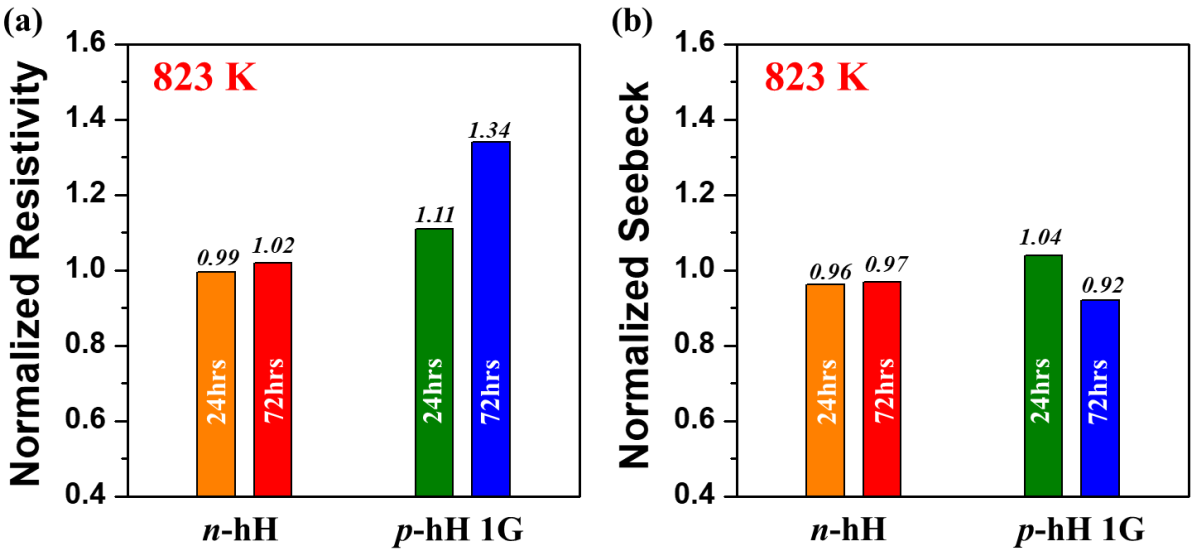

Figure 6.6 Electrical resistivity and Seebeck coefficient variation in two different compositions of *n*-hH and *p*-hH 1G. (a) resistivity change and (b) Seebeck coefficient change at 823 K as a function of duration time.

shows more than 30% of increase in electrical resistivity and 10% degradation in Seebeck coefficient due to the severe oxidation and loss of Sn dopants at the surface.

6.4 Thermal stability improvement in *p*-type hH through compositional modification

Compared to *n*-type hH composition, *p*-type 1G hH exhibited a significant degradation at 823 K in air. In order to overcome this problem, the Ti-substituted MCoSb (discussed in chapter 4) and new *p*-type NbFeSb composition was investigated. Here, the Ti-substituted $(Hf_{0.4}Zr_{0.4}Ti_{0.2})CoSb_{0.8}Sn_{0.2}$ compound is named as a second generation (labeled as "*p*-hH 2G") and new *p*-type $(Nb_{0.6}Ti_{0.4})FeSb_{0.95}Sn_{0.05}$ composition is named as a third generation (labeled as "*p*-hH 3G").

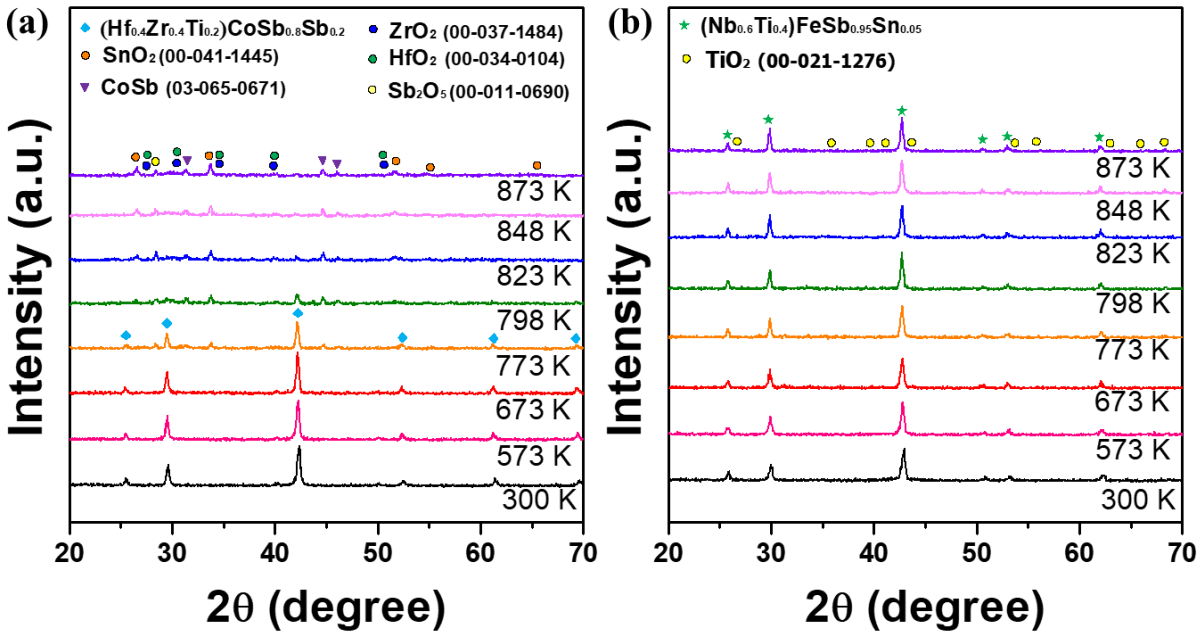

Figure 6.7 In-situ XRD with isothermal heating at eight different temperatures (300, 573, 673, 773, 798, 823, 848, and 873 K) for (a) *p*-hH 2G and (b) *p*-hH 3G alloys in air.

Figure 6.7 shows in-situ XRD results of *p*-hH 2G and 3G alloys from room temperature to 873 K. Compared to *p*-hH 1G alloys, Ti-substituted MCoSb composition show improved thermal stability up to 773 K. However, this composition is also sensitive to the oxidation at higher temperatures above 823 K as shown in **Figure 6.7a**. Surprisingly, NbFeSb-based composition presents remarkably stable XRD results over the whole high temperature region in the air. Strong and predominant hH phase is observed up to 873 K. It can be noted that pure NbFeSb compound reported by Silpawilawan *et al.* [100] exhibits worse stability compared to other composition. It is probably attributed to high fraction of titanium element in M-site (40 at%). The effects of titanium on the high temperature stability in hH structure needs to be further investigated by more controlled experiments.

Steady-state thermal stability at high temperature of 873 K was examined to understand operating temperature limit encouraged by the result of excellent stability of *p*-hH 3G compound.

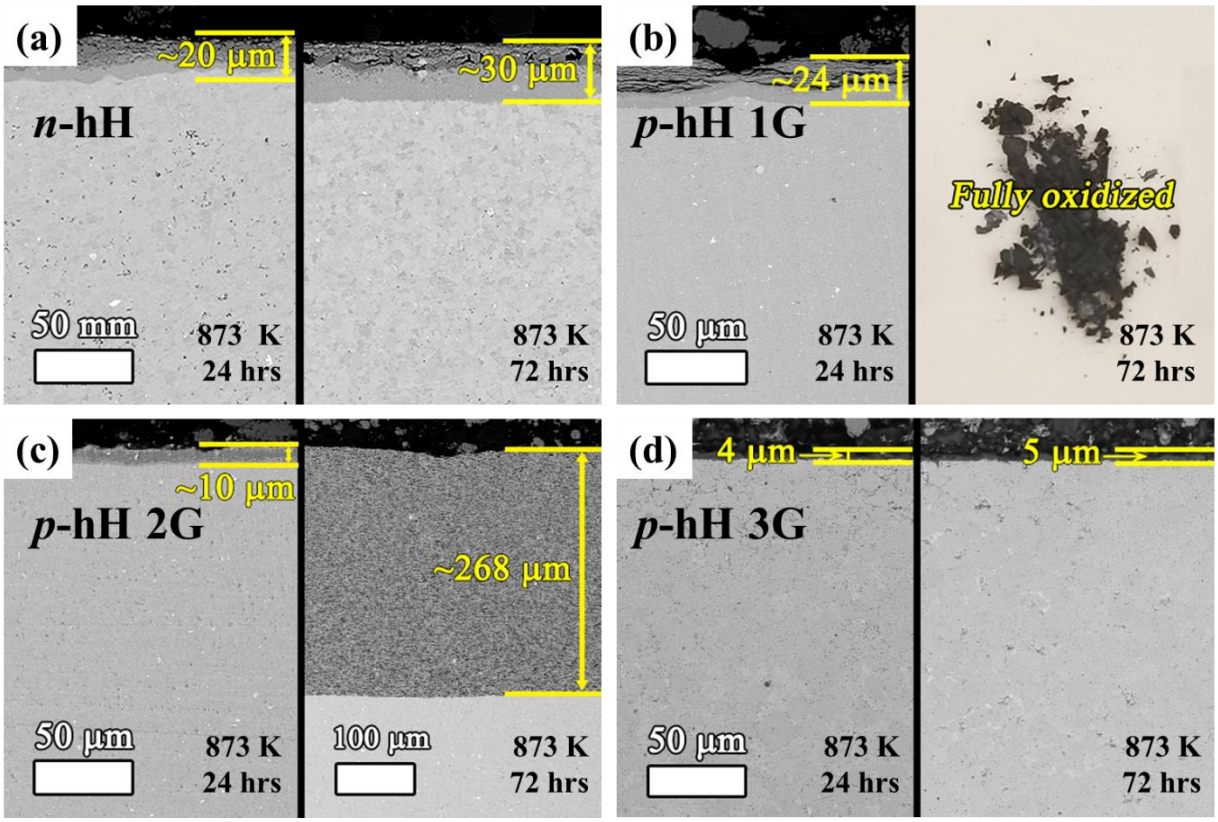

Figure 6.8 Comparison of BSED-SEM images in four different hH compositions with different annealing condition. (a) *n*-hH, (b) *p*-hH 1G, (c) *p*-hH 2G, and (d) *p*-hH 3G at 873 K for 24 and 72 hours.

Figure 6.8 shows BSED-SEM images of four different compositions of *n*-hH, *p*-hH 1G, 2G, and 3G alloys after long-term annealing at 873 K. Despite the formation of oxide layer at surface, *n*-hH alloy presents relatively small change in the oxidation layer thickness (~30 µm) at higher temperatures after 72 hours. A mass change of less than 1 % was observed as shown in **Figure 6.8a and 6.9a**. **Figure 6.10a** indicates relevant XRD results for the 873 K annealed *n*-hH alloy for two different annealing times. It has almost identical diffraction pattern with that for 823 K-24 hours annealed sample (**Fig. 6.3**). **Figure 6.10b** shows more clear Ni_3Sn intermediate phase formation beneath the oxide layer. Nickel stannides are well known for excellent protection of metals by restriction of carbon diffusion [101,102]. Thus the slower

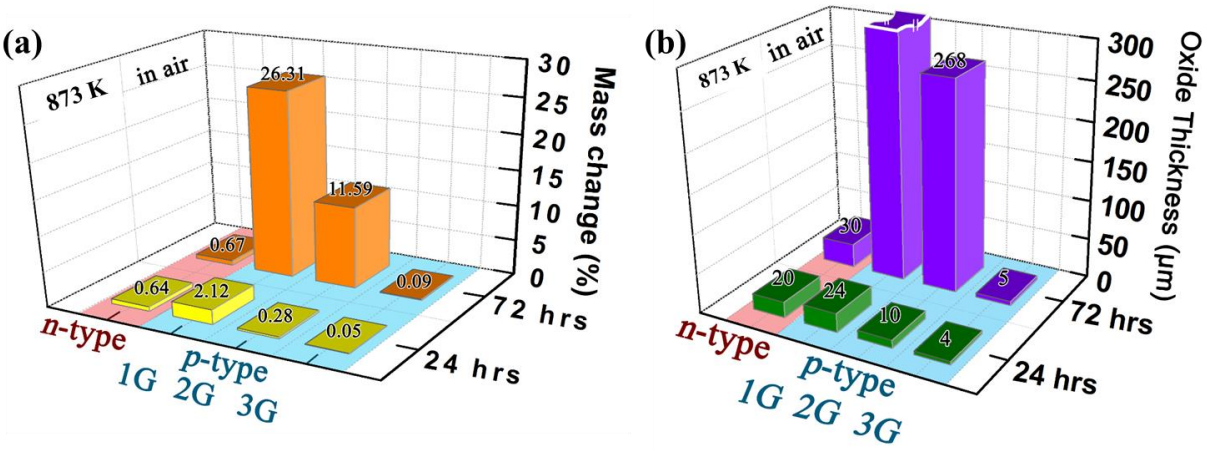

Figure 6.9 Summary of (a) mass change and (b) oxide thickness of four hH compounds depending on duration time at 873 K annealing.

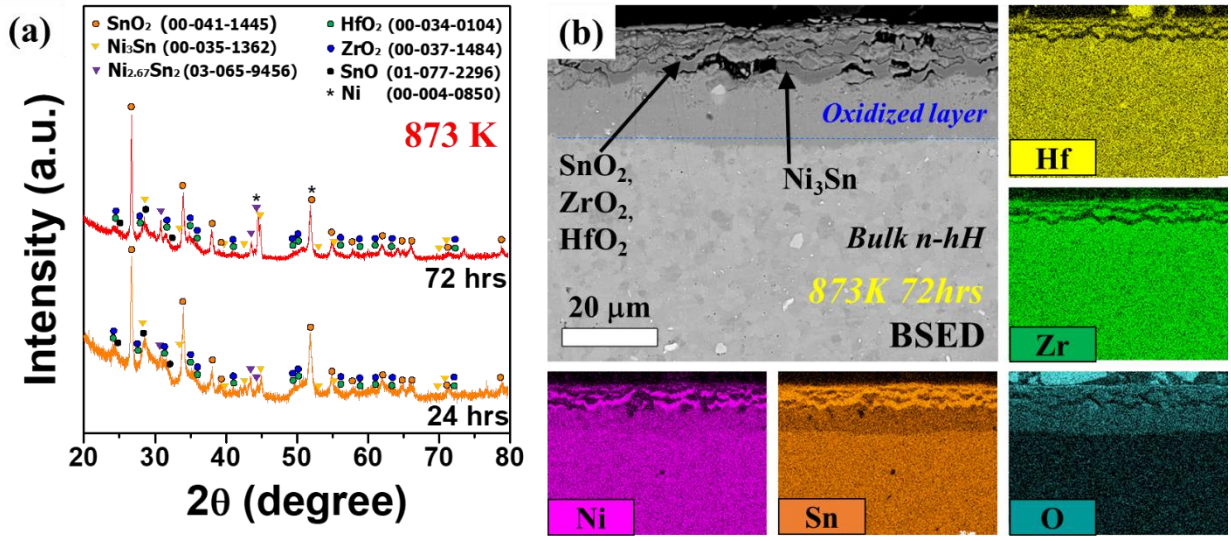

Figure 6.10 (a) XRD patterns of annealed *n*-type hH alloy at 873 K for 24 and 72 hours. (b) the corresponding BSED-SEM image of longer time annealed *n*-hH with EDS mapping.

propagation of oxide phase in *n*-hH alloy can be related to the Ni-Sn intermediate phase formation.

Unfortunately, *p*-hH 1G alloy was fully oxidized and pulverized after annealing at 873 K for 72 hours with 26 % of a mass gain. On the other hand, *p*-hH 2G compound can survive under the same condition by simply replacing Hf/Zr atoms to 20 at% of titanium, which is in accordance

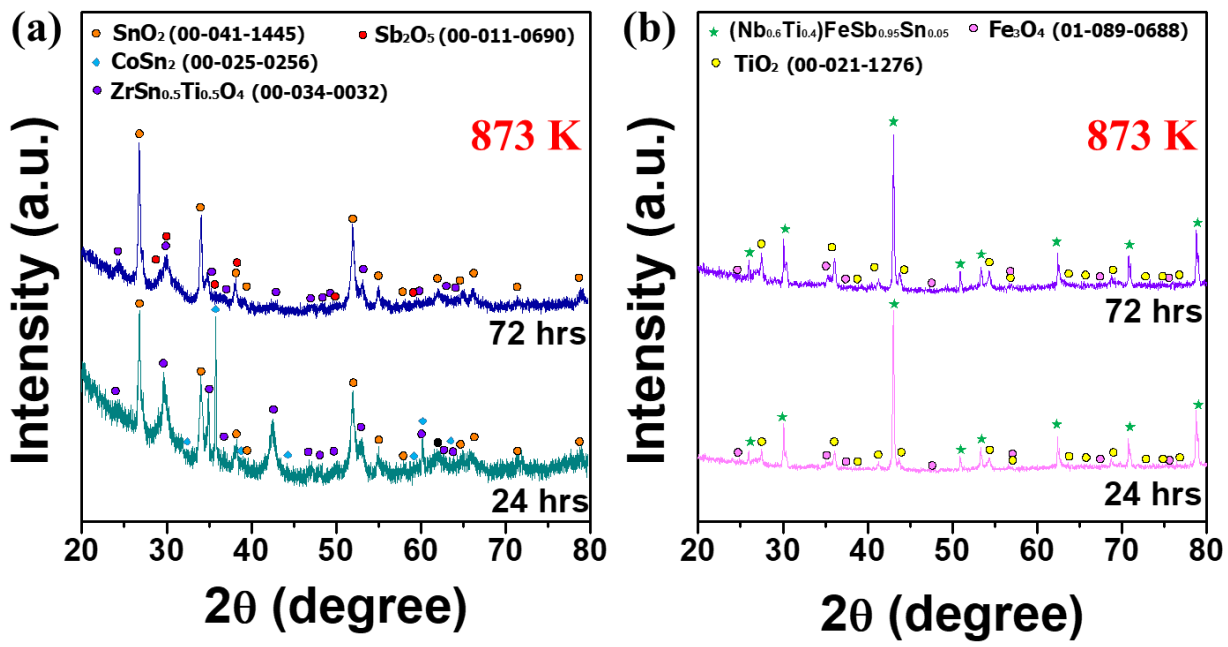

Figure 6.11 X-ray diffraction patterns of (a) *p*-type 2G and (b) 3G hH compounds that annealed at 873 K for 24 hours and 72 hours.

with a dynamic thermal analysis of in-situ XRD as a better thermal stability under the heating. However, it is still susceptible to oxidation at higher temperature, exhibiting a mass gain of 11.6% and thick oxidation layer of 268 μm after 72 hours annealing as displayed in **Figure 6.8c, 6.9, and 6.12a**. It involves only oxide phases, such as SnO_2, Sb_2O_5, and $ZrSn_{0.5}Ti_{0.5}O_4$ as presented in X-ray diffraction and EDS mapping (**Fig. 6.11a and Fig. 6.12a)**.

The most noticeable change in high temperature thermal stability has been found in *p*-type 3G hH alloy as shown in **Figure 6.8d, 6.9, 6.11b, and 6.12b**. The *p*-type NbFeSb-based hH alloy shows exceptional thermal stability at higher temperature of 873 K for 72 hours. Very thin oxide layer (<5 μm) is formed at the surface of *p*-hH 3G alloy which is further identified as TiO_2 phase in XRD and EDS mapping (**Fig. 6.11b and 6.12b**, respectively).

As a result, both of *n*-type hH and *p*-type 3G hH compounds represent excellent high temperature thermal stability in terms of electrical transport properties as shown in **Figure 6.13**.

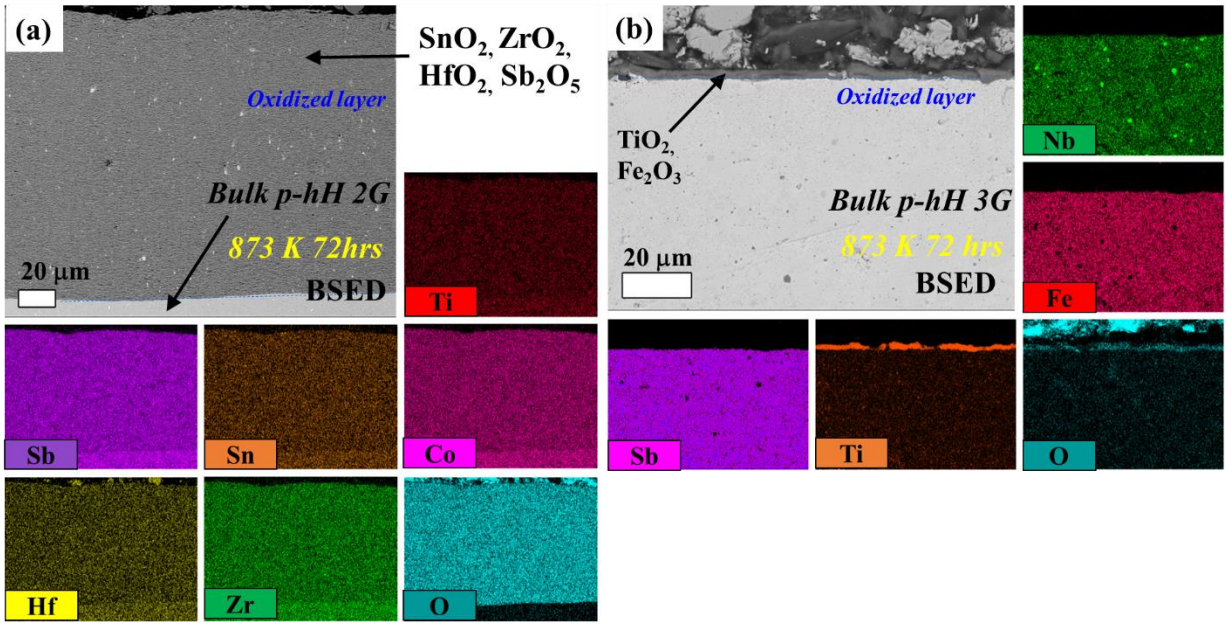

Figure 6.12 Cross-sectional BSED-SEM images of the annealed (a) *p*-type 2G and (b) 3G hH samples at 873 K for 72 hours with elemental EDS mappings.

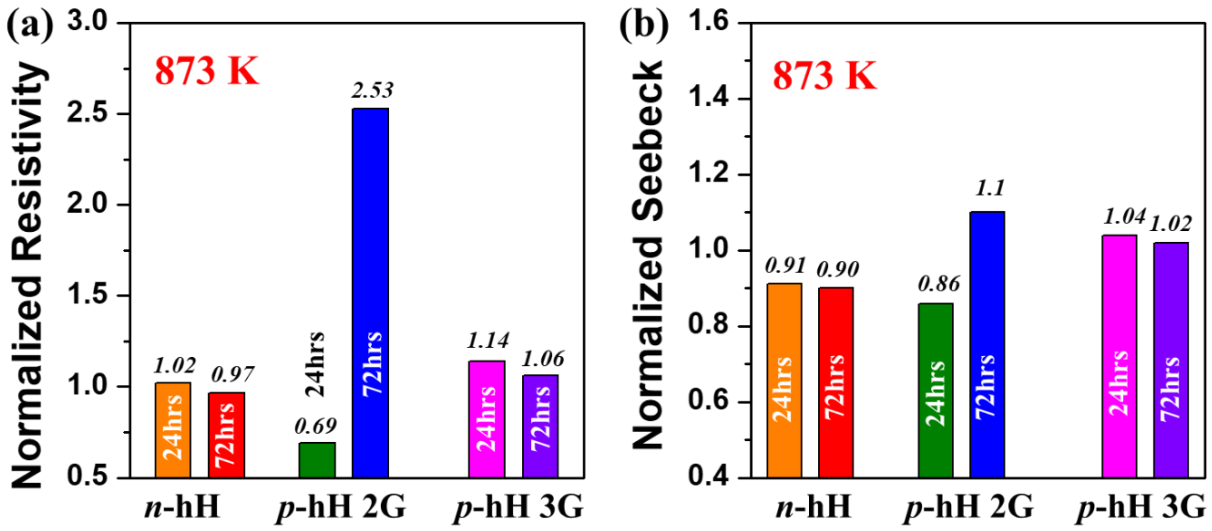

Figure 6.13 Electrical resistivity and Seebeck coefficient variation in three different compositions of *n*-hH, *p*-hH 2G and *p*-hH 3G. (a) resistivity change and (b) Seebeck coefficient change at 873 K as a function of duration time.

The electrical resistivity and Seebeck coefficient of *n*-hH and *p*-hH 3G remains almost constant in contrast to *p*-hH 2G compound. The *p*-hH 2G alloy shows a significant increase in electrical resistivity and Seebeck coefficient due to the formation and penetration of oxide layers.

6.4 Conclusion

In this chapter, a high temperature thermal stability of various hH compositions is studied by dynamic and steady-state thermal analysis. All the hH compositions are stable up to 673 K in air, but above 773 K the thermal stability turns to be very sensitive to their chemical composition. The *n*-type hH alloy generally shows stable TE performance after heat treatment with slower rate of the oxidation reaction at high temperature and for long duration time. This is related to semi-metallic nickel stannide phase formation. The *p*-type hH series displays dramatic change in the high temperature thermal stability according to their chemical compositions. The $(Nb_{0.6}Ti_{0.4})FeSb_{0.95}Sn_{0.05}$ compound exhibits outstanding high temperature stability in TE properties and phase transformation. More investigations are required in order to fully understand the mechanism behind these variations.

Chapter 7 Half-Heusler based thermoelectric generator

7.1 Introduction

In thermoelectric community, it has been one of the biggest challenge to translate high TE performance of materials into excellent TE devices. There has been a lot of outstanding progress and innovation in material zT improvement through band engineering [31,62,63,103-105], nanostructuring [26,27,39,40,44,69,87,106-110], phonon scattering control [13-15,30,46,47,71,111-113], nanocomposite [25,43,82,83,85,114], and multi-scale hierarchical architecture [42,94,115,116]. However, the corresponding TE devices and their performance have not seen similar advances. Commercially, only few companies such as TECTEG, Thermo-Gen, Tellurex and Gentherm Inc. have been successful in fabricating medium temperature modules. In order to achieve TE-based power generators, it is essential to achieve more than 10% of conversion efficiency (η) at the device level with reliable and sustainable operation over a broad temperature range. Therefore, the "performance" and the "stability" should be considered in parallel to provide a major step forward. TE material's performance and stability have been addressed in the previous chapters as a step towards design of high output performance TE device. Here, a successful translation of outstanding material property into excellent TEG performance is achieved by minimizing parasitic loss in the device. As a result, the high power density and the conversion efficiency of hH based TEG is obtained along with excellent long-term air stability of device at high temperatures.

7.2 Fabrication of uni-couple half-Heusler TEG

In general, a thermoelectric generator comprises of two different *n*-and *p*-type of TE semiconductors. Since the TE device will undergo a high temperature heat cycling to generate

electricity, similarity of thermal property between two materials is very important to avoid mechanical failure of the materials during the operation. For example, a large difference in the coefficient of linear thermal expansion (CTE) between two TE materials may give rise to a serious problem of cracking or delamination in the materials by applying a large temperature gradient into small size of the TE legs. Interestingly, *n*-type (Hf,Zr)NiSn and *p*-type (Hf,Zr)CoSb compounds exhibit analogous CTE between them as shown in **Figure 7.1**. There is only 3 % difference between *n*-type and *p*-type hH up to 1000 K, which is in a good agreement with the literature [7,117].

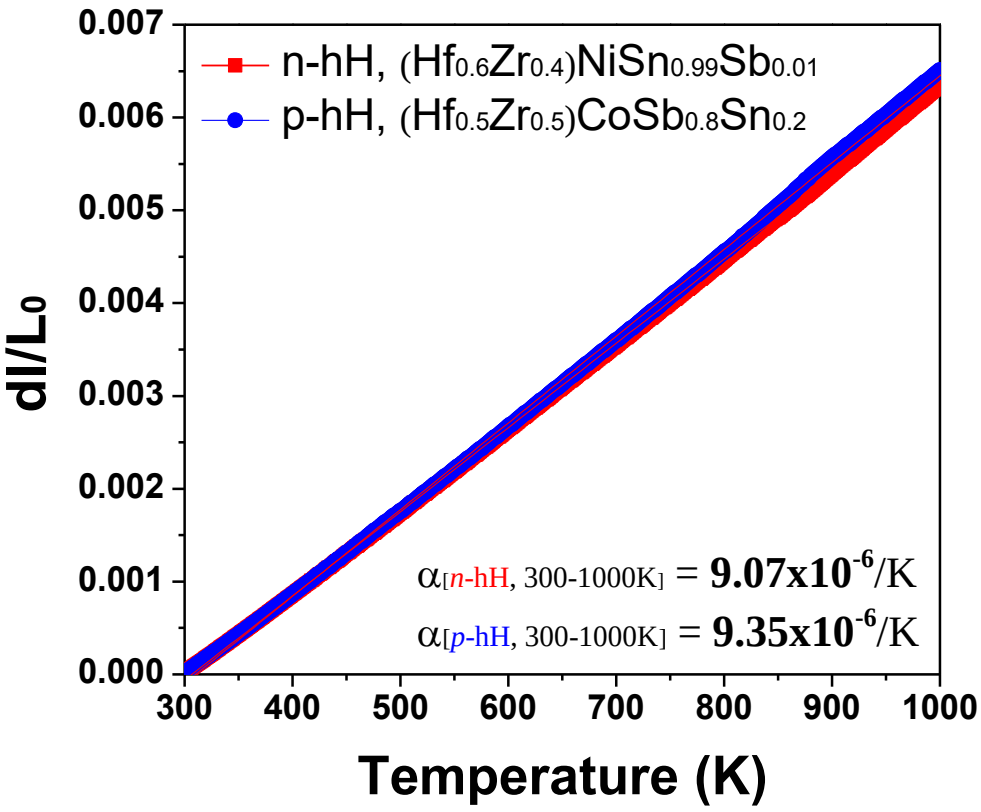

Figure 7.1 The coefficient of linear thermal expansion for *n*-type $(Hf_{0.6}Zr_{0.4})NiSn_{0.99}Sb_{0.01}$ (red square) and *p*-type $(Hf_{0.5}Zr_{0.5})CoSb_{0.8}Sn_{0.2}$ (blue circle) alloys.

Figure 7.2 displays the overall fabrication process for high quality uni-couple TEG. In order to produce a massive number of TEG legs for device fabrication, the hH wafer size was enlarged to 30 mm diameter by modifying sintering condition (**Fig. 7.2a**) and material's uniformity over the extensive area was examined as shown in **Figure 7.2c**. It shows almost identical electrical resistivity over the five different TEG legs with less than 4 % of standard deviation. Next, accurate wafer dicing was conducted using MA-1006 micro automation dicing saw. Low cutting speed (1.27 $mm \cdot s^{-1}$) and spindle rpm (16 krpm) were applied to avoid cracking problem considering high hardness and brittleness of hH alloys. **Figure 7.2b** represents the diced hH wafers with the micro control program cutting steps. The size of the legs was determined from theoretical calculation of module design by considering thermal loss and device efficiency [118]. The fabricated *n*-type and *p*-type hH legs were assembled electrically in series and thermally in parallel using the Cu-based high-temperature brazing material as shown in **Figure 7.2d**.

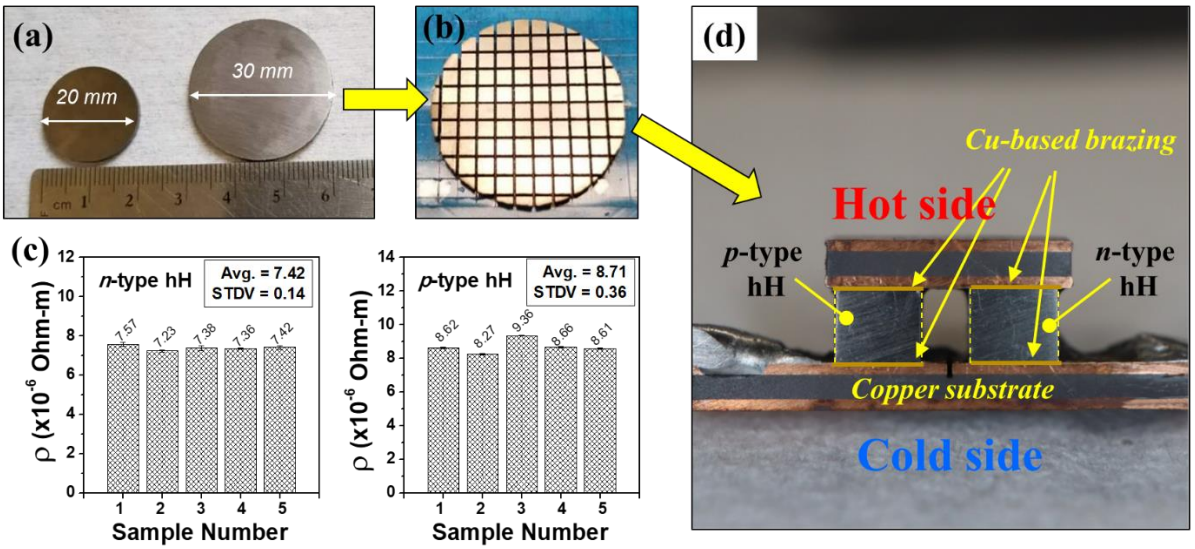

Figure 7.2 (a) Enlarged size of hH wafers for TEG fabrication, (b) diced hH wafer with high accuracy of 0.01 mm, (c) the electrical resistivity uniformity of *n*-type and *p*-type TEG legs, and (d) the structure of uni-coupled TEG.

In order to effectively translate the TE material's performance to the device output, it is essential to minimize the parasitic losses due to the contact resistance between the TEG legs and electrodes [118]. The effective ZT of the thermoelectric device is given by the following equation [119,120],

$$(ZT)_D = \frac{l}{l + 2\sigma r_c}(ZT)_M \qquad (7.1)$$

where l is the length of the thermoelectric leg, r_c is the contact resistance, σ is the electrical conductivity and $(ZT)_M$ is the effective ZT of the thermoelectric material between the hot-side and the cold-side. The electrical conductivity for (Hf,Zr)NiSn and (Hf,Zr)CoSb based materials is about ~10^5 S·m^{-1} at room temperature, which means a very low r_c plays a prominent role in controlling the TE device performance according to **Equation 7.1**. For power generation applications, *p*-type and *n*-type materials are connected in series by brazing onto a conductive substrate as shown in **Figure 1.4** and **Figure 7.2**. The brazing material should have high electrical and thermal conductivity, possess similar thermal expansion as that of TE material, exhibit high wetting capability with the material surface and avoid interfacial reactions [119]. Here, we connected the thermoelectric legs with the copper interconnect high-temperature brazing material. Next, the contact resistance of both TE legs was measured by a four-probe technique as represented in **Figure 7.3**. **Figure 7.3a** illustrates the working mechanism of the four probe measurement. The probe scans the surface of TE leg in the direction of bottom electrode → brazing Cu-alloy → TE legs → brazing Cu-alloy → top electrode as shown in **Figure 7.3b**. The contact resistance (r_c) of *p*- and *n*-type legs with the brazing material were measured to be < ~1 μΩ·cm^2, showing ultra-low values compared to other hH based modules in the literature [31,121]. **Figure 7.3c and d** displays the four-probe scan data for both TE legs. It is clear that there is a negligible contact resistance for both TE legs.

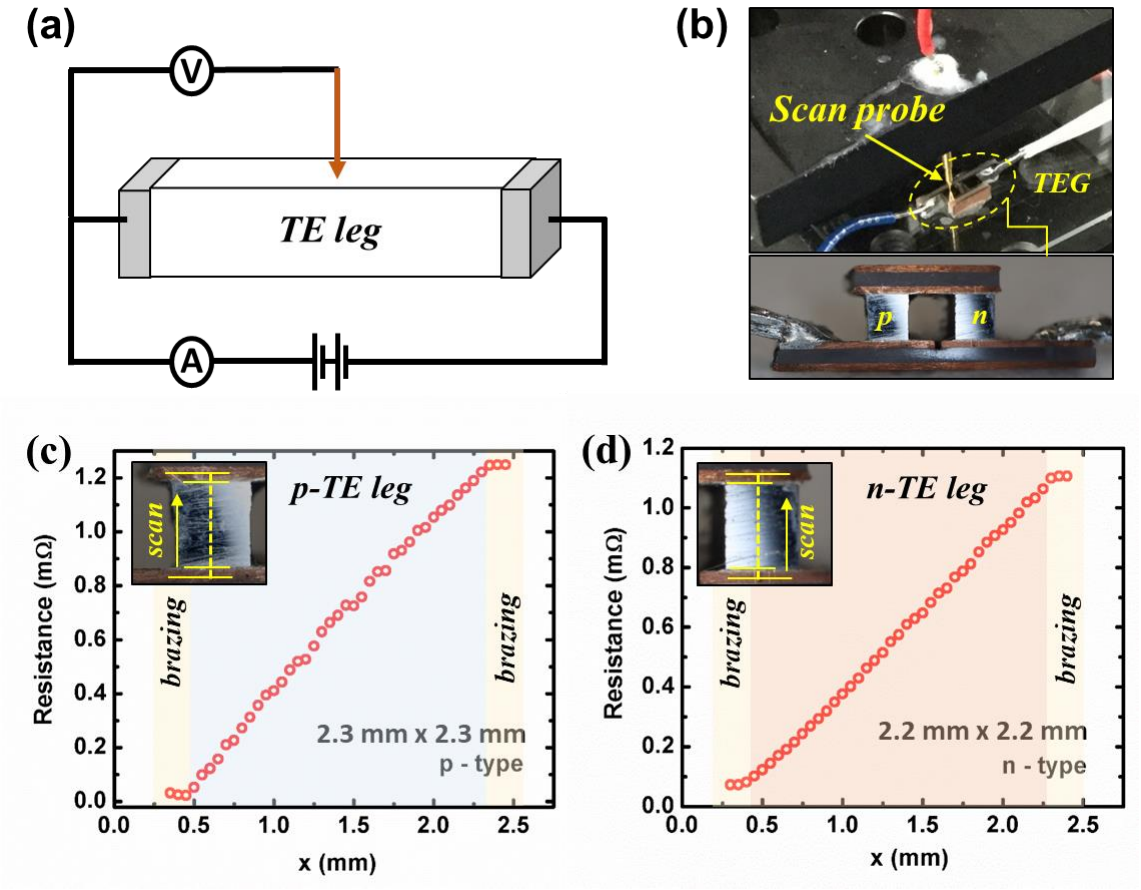

Figure 7.3 (a) The schematic illustration of contact resistance measurement, (b) picture of home-made contact resistance measurement system and TEG, (c) contact resistance of *p*-type TE leg and, (d) *n*-type TE leg.

7.3 High power density and efficiency TEG based on nanocomposite

Figure 2.5 shows uni-couple hH TEG and test set up for the power output and conversion efficiency measurement of the TEG. Internal resistance (r_i), short circuit current (I_{SC}), and peak output power (P_{max}) for the device can be evaluated using the expressions:

$$r_i = \frac{V_{oc} - V_d}{I_d} \tag{7.2}$$

$$I_{SC} = \frac{V_{oc}}{2r_i} \tag{7.3}$$

$$P_{max} = \frac{V_{oc}^2}{4r_i} \tag{7.4}$$

where, V_d is the device voltage and I_d is the device current.

We measured the open circuit voltage (V_{oc}), device voltage (V_d), calculated the internal resistance (r_i) and the peak power output (P_{max}) by varying hot-side temperature from 473 K to 873 K under nearly constant cold-side temperature of 293 K.

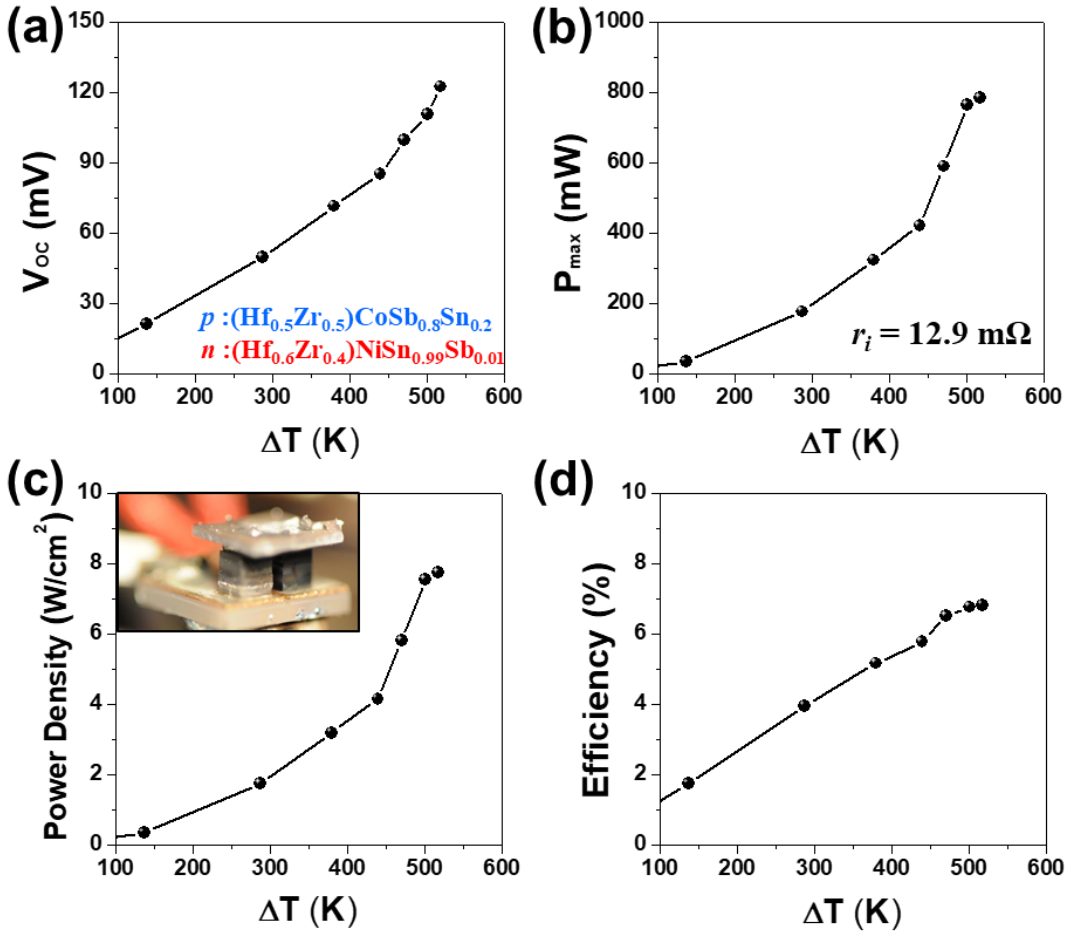

Figure 7.4 The output performance of uni-couple 1G hH TEG. (a) open circuit voltage, (b) maximum peak output power, (c) power density, and (d) conversion efficiency as a function of the temperature difference.

Figure 7.4 indicates the output performance of uni-couple hH TEG based on the first generation (1G) compounds of *n*-type $(Hf_{0.6}Zr_{0.4})NiSn_{0.99}Sb_{0.01}$ and *p*-type $(Hf_{0.5}Zr_{0.5})CoSb_{0.8}Sn_{0.2}$. At the highest temperature of 873 K (ΔT = 520 K), the uni-couple 1G hH TEG represented the output voltage of 122.5 mV, the peak power of 784 mW with the resistance of 12.9 mΩ as shown in **Figure 7.4a and b**. This results in high power density of 7.73 $W \cdot cm^{-2}$ and conversion efficiency of 6.83 % under the input heat flux (Q_{in}) of 11.4 W (Fig. 7.4c and d).

In order to further improve the TEG output performance, higher zT hH alloys called as second generation (2G), were applied as the replacement of 1G TE legs. The *n*-type tungsten/hH nanocomposite and Ti-substituted *p*-type $(Hf_{0.4}Zr_{0.4})Ti_{0.2}CoSb_{0.8}Sn_{0.2}$ compound were used for the uni-coupled 2G hH TEG. The temperature dependence of output voltage (V_{oc}) and maximum peak power (P_{max}) for the 2G hH TEG is shown in **Figure 7.5a and b**, respectively. At temperature difference (ΔT) of 674 K, the uni-couple TEG showed V_{oc} ~230.31 mV, I_{SC} ~12.25 A and the P_{max} ~1410.7 mW. The uni-couple resistance (r_i) is ~9.4 mΩ at the highest temperature.

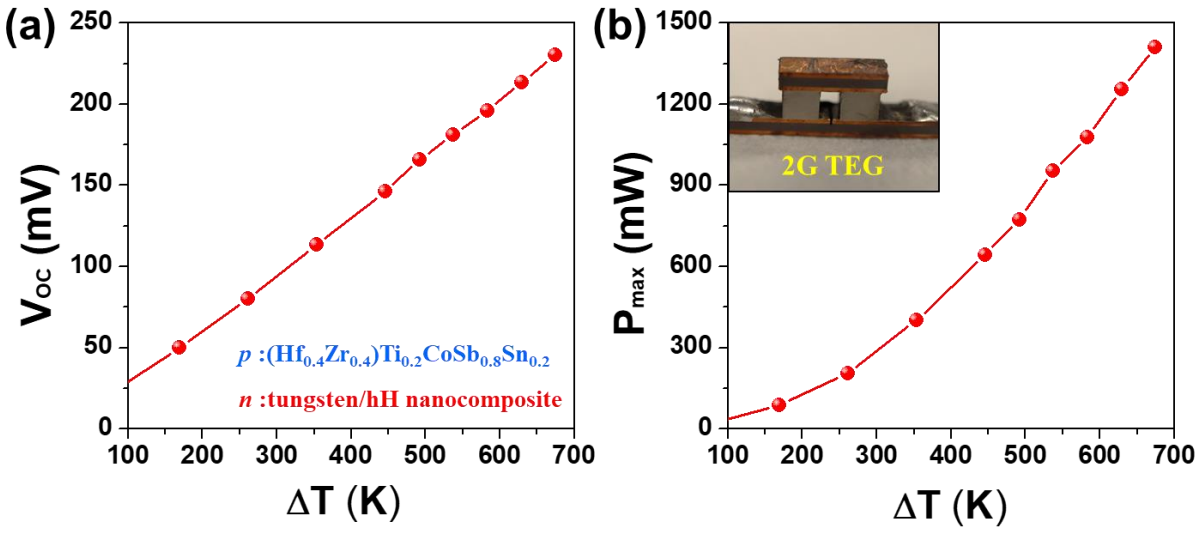

Figure 7.5 The output performance of uni-couple 2G hH TEG. (a) Open circuit voltage (V_{oc}). (b) Maximum peak output power as a function of the temperature difference (ΔT).

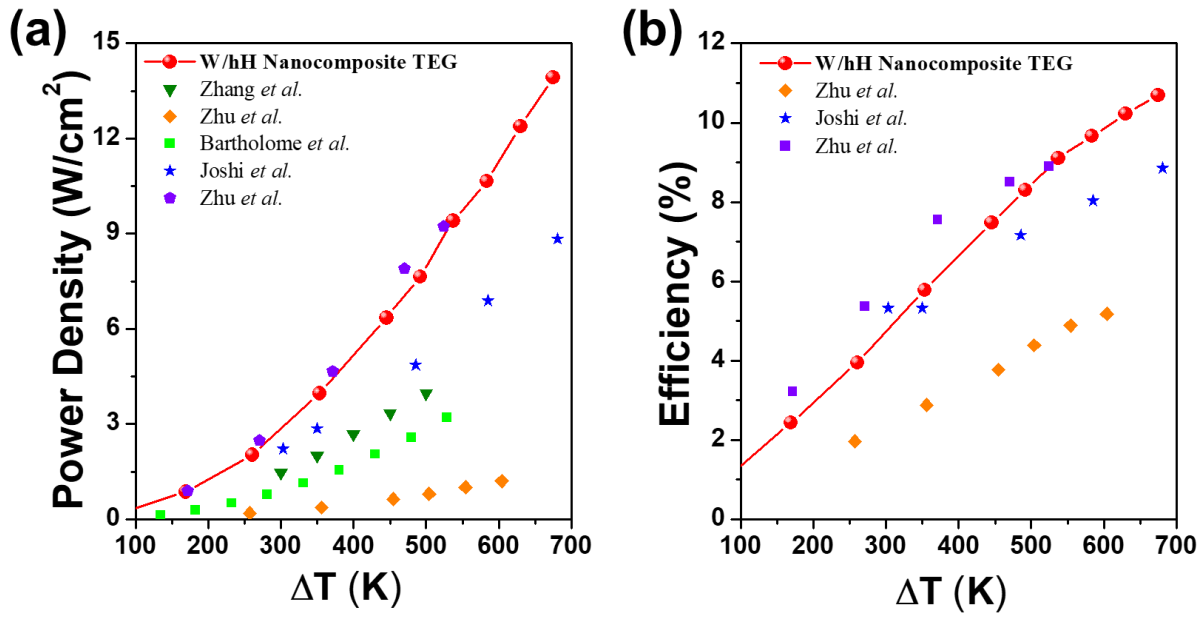

Figure 7.6 Comparison of (a) power density, and (b) conversion efficiency of the nanocomposite TEG developed in this work and other hH based TEGs [50,61,64,121,122] reported in previous studies as a function of temperature difference (ΔT).

Compared to the output performance of 1G hH TEG at the same temperature gradient, the output voltage was increased by 47.7 % and the maximum power was improved by 21.5 % in 2G hH TEG. The power density of uni-couple 2G hH TEG is also calculated from the peak power output and the activation area of TEG as shown in **Figure 7.6a**. The power density of this device was measured to be ~13.93 W·cm^{-2} across a temperature difference of 674 K. **Figure 7.6b** shows the conversion efficiency of 2G hH TEG corresponding to the output performance. The outstanding conversion efficiency of 10.7 % was achieved at ΔT = 674 K.

We compare our output performance with other hH-based TEGs reported in the literature [50,61,64,121,122]. Zhang *et al*. [122] developed a 1kW TEG system comprising of 400 TEG modules under a temperature difference of 339 K, where the TEG module produces a power density of 4 W·cm^{-2} across a temperature difference of 500 K. Zhu *et al.* [61] demonstrated a power

density of 1.2 $W \cdot cm^{-2}$ under ΔT = 603 K from a hH module based on *n*-type ZrNiSn alloys and *p*-type $FeNb_{0.8}Ti_{0.2}Sb$ compounds. Seven pairs of uni-couple hH module were demonstrated by Bartholome *et al.* [121] that exhibited power density of 3.2 $W \cdot cm^{-2}$ under ΔT = 527 K. Joshi *et al.* [64] reported the power density of ~8.9 $W \cdot cm^{-2}$ with a high conversion efficiency of 8.9 % across a temperature difference of 678 K. Zhu *et al.* [50] recently demonstrated a good transition of the record high zT into outstanding TEG performances in *p*-type $ZrCoBi_{0.65}Sb_{0.15}Sn_{0.20}$. The single leg TEG for ZrCoBi shows the peak power density of ~9.3 $W \cdot cm^{-2}$ and the conversion efficiency of ~9 % at the hot-side temperature of 823K [50]. As represented in **Figure 7.6**, our TEG compares favorably with the record high TEG performance over a wide temperature range and exhibits highest power density of ~13.93 $W \cdot cm^{-2}$ and conversion efficiency of ~10.7 % at the ΔT = 674 K. This result confirms that the significant improvement obtained in material performance can be translated into excellent TEG device performance through an optimized manufacturing process that results in reduced contact resistance.

7.4 Long-term TEG performance under high temperature heat cycling

Based on the thermal stability study in *chapter 6*, two different types of uni-coupled TEG were fabricated using the pair of W/*n*-hH nanocomposite (*n*-hH) and $(Hf_{0.4}Zr_{0.4}Ti_{0.2})CoSb_{0.8}Sn_{0.2}$ (*p*-hH 2G) and another pair of *n*-hH and $(Nb_{0.6}Ti_{0.2})FeSb_{0.95}Sn_{0.05}$ (*p*-hH 3G). **Figure 7.7a** shows the operation time dependence of the output TEG performance in two TEGs at hot side temperature of 823 K in air. The cold side temperature was kept constant at 294 K by cooling water and the output power of the devices was normalized for a comparison. There is a distinct difference between two TEG devices in the output power durability over the time. The MNiSn/MCoSb-based TEG exhibits a rapid degradation after 12 hours of operation. The output power of MNiSn/MCoSb-based TEG was decreased by about half after a long time operation for 5 days in air.

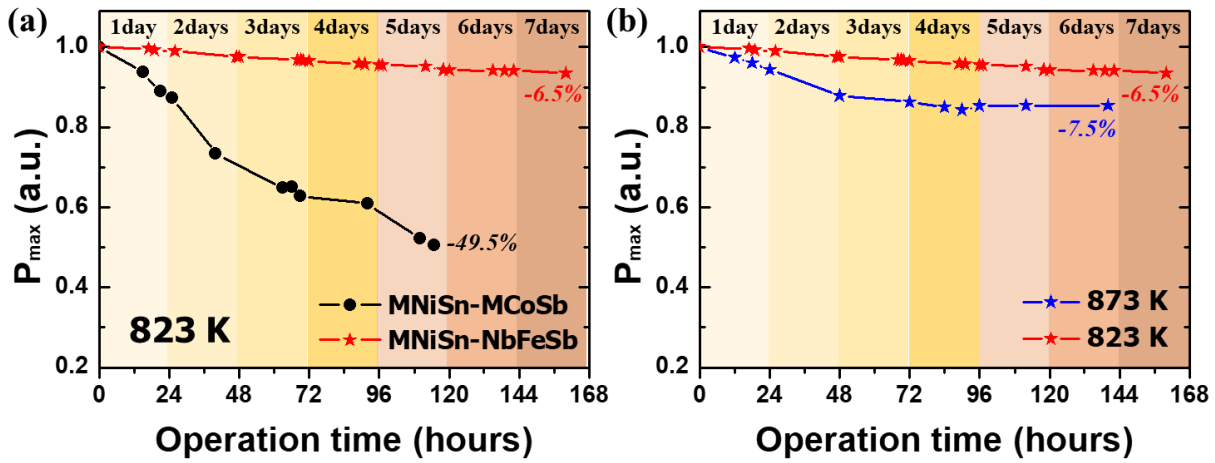

Figure 7.7 TEG performance as a function of operation time. (a) Long-term output power comparison between two different uni-coupled TEG types (*n*-hH/*p*-hH 2G and *n*-hH/*p*-hH 3G) at 823 K in air, and (b) output performance of MNiSn-NbFeSb uni-coupled TEG at 823 and 873 K in air.

In contrast, MNiSn/NbFeSb-based TEG displays very stable output performance in the long time operation for 7 days in air. It was only degraded by 6.5 % from the initial output power. The long-term durability results of two TEG devices are in agreement with our earlier study on the material stability in *chapter 6*. The $(Nb_{0.6}Ti_{0.4})FeSb_{0.95}Sn_{0.05}$ composition showed excellent in-air thermal stability at high temperature in contrast to the MCoSb compositions. Since *n*-type MNiSn hH composition also exhibited good stability in electrical properties under the heat treatment, the big difference in the durability of the devices is mainly attributed to the material's stability of *p*-type hH compositions. Further higher hot side temperature was applied in the stable MNiSn/NbFeSb-based TEG as shown in **Figure 7.7b**. Although the output power was degraded a little bit more (-1%) at higher temperature, the output power still remained as a pretty high number of 92.5 %. It is noted that increasing the hot side temperature by 50 K provides 25 % conversion efficiency improvement from the theoretical calculation using **Equation 1.19** as represented in **Figure 1.5**.

Therefore, the 1 % drop by elevating temperature can be amply compensated by higher output power generation.

7.5 Conclusions

In this chapter, high output performance of hH-based TEG module was demonstrated with the durable TEG performance under the long time operation in air. High quality uni-coupled hH TEGs were fabricated by adjusting extremely low contact resistance of ~1 $\mu\Omega\cdot cm^2$. The output TEG performance can be improved by applying higher quality hH nanocomposite material. The outstanding TE material properties were successfully translated into the TEG module output. The hH nanocomposite based TEG showed a record-high power density of ~13.93 $W\cdot cm^{-2}$ and conversion efficiency of ~10.7 % at ΔT = 674 K. Further, excellent output performance durability of TEG device was demonstrated under the long time operation at 873 K in air by replacing *p*-type TE legs from vulnerable MCoSb alloy to stable NbFeSb alloy that discovered in *chapter 6*. The durable MNiSn/NbFeSb based TEG device represents very stable output power with only 7.5 % decrease for 7 days of operation in air. This study establishes a connection between the material's properties and the device's performance in terms of the output power generation and the durability of the device.

Chapter 8 Summary and Outlook

8.1 Summary

The overarching objective in this dissertation was to design high performance hH materials and demonstrate their performance in TEG modules. Comprehensive studies were conducted to understand the mechanisms controlling the material property over a wide range of temperatures. Previous chapters provide fundamental guidelines for tuning of TE property, strategies for decoupling of heat-charge carrier transport, and design principles for realizing thermally stable hH composition at high temperature in air condition. Extensive efforts were dedicated towards design, synthesis and characterization of novel nanocomposite architectures. Thermal stability of synthesized materials was characterized under realistic operating environments. Using the optimized compositions, high performance TEG modules were developed with low contact resistances.

In *chapter 3 and 4* of this dissertation, TE properties of *n*-type MNiSn and *p*-type MCoSb are explored through synthesis process optimization and composition modification. The combination of RF induction melting, high energy ball milling, and spark plasma sintering techniques resulted in a high-quality single phase hH alloy with small grain sizes and high density. The control of sintering temperature provided variation in grain sizes of the hH alloys from sub-micron to nanoscale. Post annealing treatment of sintered materials provided additional tuning of the charge carrier concentration and mobility. Dopant engineering was found to be effective way to tailor electrical and thermal transport properties in *p*-type hH alloys. As a result, a high peak zT of ~1.0 was achieved in both *n*- and *p*-type hH alloys.

In *chapter 5*, novel multi-phase nanocomposite was developed by incorporation of tungsten nanoparticles into *n*-type hH alloy. The novel nanocomposite design played a critical role in

realizing a record-high zT for *n*-type hH alloys by providing simultaneous improvement of the power factor ($S^2\sigma$) and reduction in thermal conductivity (κ). This unique microstructure facilitates multi-length-scale phonon scattering and electron injection/energy filtering that efficiently decouples electronic and thermal transports.

High temperature thermal stability of hH materials was investigated in *chapter 6*. Four different hH compositions were studied by dynamic and steady-state thermal analysis. The *n*-type MNiSn and *p*-type NbFeSb compounds showed excellent thermal stability at high temperature up to 873 K in air condition. On the other hand, *p*-type MCoSb compounds were only stable up to 673 K and had a serious degradation above the temperature of 773 K in air due to significant surface oxidation.

Building upon the hH material studies, high output hH TEGs were fabricated that exhibited extremely low contact resistance of ~1 μΩ, as described in *chapter 7*. The outstanding material figure of merit was successfully translated into module performance. The TEG module was found to exhibit ultra-high power density and conversion efficiency. The excellent thermal stability of *n*-type MNiSn and *p*-type NbFeSb compounds was translated into stable and sustainable TEG operation in air at high temperatures.

Major achievements of this study are:

(i) A fundamental understanding of material design methodology for thermoelectric materials that provides the ability to tailor electronic transport and phonon scattering beyond the commonly demonstrated regimes (*chapter 3, 4, and 5*).

(ii) Realizing simultaneous improvement in power factor (20 %) and reduction in thermal conductivity (16 %) compared to the state-of-the-art *n*-type hH materials through synergistic impacts created by multi-phase nanostructure. This resulted in highest

thermoelectric performance among reported *n*-type hH materials with 25 % improvement in figure of merit (*chapter 5*).

(iii) Development of fundamental knowledge for high temperature in-air thermal stability in different compositions of hH alloys. Results provide insight into the compositional design for higher durability hH materials.

(iv) Realizing the highest power density (13.93 %) and conversion efficiency (10.7 %) in hH material based TEG module through very low contact resistance and high figure of merit hH materials.

(v) Successful translation of material's properties into the TEG module performance in terms of the output power and stability.

These findings will create tremendous excitement in thermoelectric community and advance the thermoelectric applications for waste heat recovery systems. Further, the material design approach demonstrated in this study will be of interest to broader community in tailoring the electrical and thermal behavior and material's stability to further realize high output device performance.

8.2 Outlook

The analysis and design principles presented in this dissertation can be further expanded to other material systems in order to improve the material performance and obtain better understanding of the mechanisms. Several suggestions are given below.

Even though the effect of post heat treatment is clear at the macroscopic scale, additional analysis involving NMR spectroscopy, XPS, and TEM is required to provide a deeper understanding of post annealing effects. In addition, the impact of post annealing on *p*-type hH materials and the best conditions for heat treatment were not fully determined. The fundamental

understanding of the mechanisms will give an advantage in introducing effective post treatment technology for TEs.

There are more opportunities in the nanocomposite design by controlling variety of microstructural parameters. Different types of nanoinclusions can be introduced in the hH matrix following the concept nanocomposite design proposed in this dissertation. Basic requirements for the metallic inclusions are that it should be non-reactive and stable at temperatures above 1273 K. The difference between sound speed of nanoinclusion and hH matrix, crystal structure, work function, band structure, and specific heat capacity are the other intrinsic parameters that should be considered. The nanoparticle size, concentration, grain size of matrix, charge carrier concentration of matrix are extrinsic control parameters. Finding the interrelationship between intrinsic/extrinsic parameters and TE properties can provide a breakthrough in the nanocomposite design that can be extended to all the TE materials. The theoretical modeling of the band structure and correlation between inclusions and hH matrix can elucidate better understanding of the mechanisms.

The thermal stability study provides insight into high temperature stable material design. The function and effectiveness of Ni-Sn phase on high temperature thermal stability needs to be systematically studied by external Ni-Sn film surface coating. This dissertation provides experimental results on the thermal stability of materials. Thus, it can be extended to more systematic and precise modeling/experimental study that involves control of oxygen partial pressure, and dependence on Ti (or Nb) concentration. It would allow us to find the best composition having excellent thermal stability.

Reference

[1] J.L. Pellegrino, N. M., M. Justiniano, M. Miller, A. Thedki. (2004). *Energy Use, Loss and Opportunities Analysis: US Manufacturing & Mining*. Retrieved from www.eere.energy.gov/industry/energy_systems

[2] Blaney, B. L. (1984). *Industrial waste heat recovery and the potential for emissions reduction*.

[3] Viswanathan, V. V., Davies, R. W., & Holbery, J. D. (2006). *Opportunity analysis for recovering energy from industrial waste heat and emissions*.

[4] Johnson, I., Choate, W. T., & Davidson, A. (2008). *Waste heat recovery. Technology and opportunities in US industry*.

[5] Forman, C., Muritala, I. K., Pardemann, R., & Meyer, B. (2016). Estimating the global waste heat potential. *Renew. Sust. Energ. Rev., 57*, 1568-1579.

[6] Chen, S., & Ren, Z. F. (2013). Recent progress of half-Heusler for moderate temperature thermoelectric applications. *Mater. Today, 16*(10), 387-395.

[7] Rogl, G., Grytsiv, A., Gürth, M., Tavassoli, A., Ebner, C., Wünschek, A., . . . Rogl, P. (2016). Mechanical properties of half-Heusler alloys. *Acta Mater., 107*, 178-195.

[8] He, R., Gahlawat, S., Guo, C. F., Chen, S., Dahal, T., Zhang, H., . . . Ren, Z. F. (2015). Studies on mechanical properties of thermoelectric materials by nanoindentation. *Phys. Status Solidi A, 212*(10), 2191-2195.

[9] Yang, J., Li, H., Wu, T., Zhang, W., Chen, L., & Yang, J. (2008). Evaluation of Half-Heusler Compounds as Thermoelectric Materials Based on the Calculated Electrical Transport Properties. *Adv. Funct. Mater., 18*(19), 2880-2888.

[10] Galanakis, I., Dederichs, P. H., & Papanikolaou, N. (2002). Origin and properties of the gap in the half-ferromagnetic Heusler alloys. *Phys. Rev. B, 66*(13), 134428.

[11] Uher, C., Yang, J., Hu, S., Morelli, D. T., & Meisner, G. P. (1999). Transport properties of pure and doped MNiSn (M=Zr, Hf). *Phys. Rev. B, 59*(13), 8615-8621. doi:10.1103/PhysRevB.59.8615

[12] Xie, H., Wang, H., Fu, C., Liu, Y., Snyder, G. J., Zhao, X., & Zhu, T. (2014). The intrinsic disorder related alloy scattering in ZrNiSn half-Heusler thermoelectric materials. *Sci. Rep., 4*, 6888.

[13] Yang, J., Meisner, G. P., & Chen, L. (2004). Strain field fluctuation effects on lattice thermal conductivity of ZrNiSn-based thermoelectric compounds. *Appl. Phys. Lett., 85*(7), 1140-1142.

[14] Yan, X., Liu, W., Wang, H., Chen, S., Shiomi, J., Esfarjani, K., . . . Ren, Z. (2012). Stronger phonon scattering by larger differences in atomic mass and size in p-type half-Heuslers $Hf_{1-x}Ti_xCoSb_{0.8}Sn_{0.2}$. *Energy Environ. Sci., 5*(6), 7543.

[15] Bhattacharya, S., Skove, M. J., Russell, M., Tritt, T. M., Xia, Y., Ponnambalam, V., . . . Thadhani, N. (2008). Effect of boundary scattering on the thermal conductivity of TiNiSn-based half-Heusler alloys. *Phys. Rev. B, 77*(18), 184203.

[16] Yan, X. A., Joshi, G., Liu, W. S., Lan, Y. C., Wang, H., Lee, S., . . . Ren, Z. F. (2011). Enhanced Thermoelectric Figure of Merit of *p*-Type Half-Heuslers. *Nano Lett., 11*(2), 556-560.

[17] Joshi, G., Yan, X., Wang, H. Z., Liu, W. S., Chen, G., & Ren, Z. F. (2011). Enhancement in Thermoelectric Figure-Of-Merit of an N-Type Half-Heusler Compound by the Nanocomposite Approach. *Adv. Energy Mater., 1*(4), 643-647.

[18] Bhattacharya, S., Tritt, T. M., Xia, Y., Ponnambalam, V., Poon, S. J., & Thadhani, N. (2002). Grain structure effects on the lattice thermal conductivity of Ti-based half-Heusler alloys. *Appl. Phys. Lett., 81*(1), 43-45.

[19] Greenwood, D. A. (1958). The Boltzmann Equation in the Theory of Electrical Conduction in Metals. *Proc. Phys. Soc., 71*(4), 585-596. doi:10.1088/0370-1328/71/4/306

[20] Cutler, M., & Mott, N. F. (1969). Observation of Anderson Localization in an Electron Gas. *Phys. Rev., 181*(3), 1336-&. doi:DOI 10.1103/PhysRev.181.1336

[21] Cutler, M., Leavy, J. F., & Fitzpatrick, R. L. (1964). Electronic Transport in Semimetallic Cerium Sulfide. *Phys. Rev., 133*(4a), 1143-+. doi:DOI 10.1103/PhysRev.133.A1143

[22] Snyder, G. J., & Toberer, E. S. (2008). Complex thermoelectric materials. *Nat. Mater., 7*(2), 105-114.

[23] Franz, R., & Wiedemann, G. (1853). Ueber die Wärme-Leitungsfähigkeit der Metalle. *Annalen der Physik, 165*(8), 497-531.

[24] Kim, H.-S., Gibbs, Z. M., Tang, Y., Wang, H., & Snyder, G. J. (2015). Characterization of Lorenz number with Seebeck coefficient measurement. *APL Mater., 3*(4), 041506.

[25] Liu, W. S., Zhang, Q., Lan, Y., Chen, S., Yan, X., Zhang, Q., . . . Ren, Z. (2011). Thermoelectric Property Studies on Cu-Doped n-type $Cu_xBi_2Te_{2.7}Se_{0.3}$ Nanocomposites. *Adv. Energy Mater., 1*(4), 577-587. doi:10.1002/aenm.201100149

[26] Poudel, B., Hao, Q., Ma, Y., Lan, Y., Minnich, A., Yu, B., . . . Ren, Z. (2008). High-Thermoelectric Performance of Nanostructured Bismuth Antimony Telluride Bulk Alloys. *Science, 320*(5876), 634-638. doi:10.1126/science.1156446

[27] Hu, X., Jood, P., Ohta, M., Kunii, M., Nagase, K., Nishiate, H., . . . Yamamoto, A. (2016). Power generation from nanostructured PbTe-based thermoelectrics: comprehensive

development from materials to modules. *Energy Environ. Sci., 9*(2), 517-529. doi:10.1039/C5EE02979A

[28] Li, W. J., Wang, J., Xie, Y. T., Gray, J. L., Heremans, J. J., Kang, H. B., . . . Priya, S. (2019). Enhanced Thermoelectric Performance of Yb-Single-Filled Skutterudite by Ultralow Thermal Conductivity. *Chem. Mater., 31*(3), 862-872. doi:10.1021/acs.chemmater.8b03994

[29] Shi, X., Yang, J., Salvador, J. R., Chi, M., Cho, J. Y., Wang, H., . . . Chen, L. (2011). Multiple-Filled Skutterudites: High Thermoelectric Figure of Merit through Separately Optimizing Electrical and Thermal Transports. *J. Am. Chem. Soc, 133*(20), 7837-7846. doi:10.1021/ja111199y

[30] Liu, Y., Xie, H., Fu, C., Snyder, G. J., Zhao, X., & Zhu, T. (2015). Demonstration of a phonon-glass electron-crystal strategy in (Hf,Zr)NiSn half-Heusler thermoelectric materials by alloying. *J. Mater. Chem. A, 3*(45), 22716-22722. doi:10.1039/C5TA04418A

[31] Fu, C. G., Bai, S. Q., Liu, Y. T., Tang, Y. S., Chen, L. D., Zhao, X. B., & Zhu, T. J. (2015). Realizing high figure of merit in heavy-band p-type half-Heusler thermoelectric materials. *Nat. Commun., 6*, 8144. doi:10.1038/ncomms9144

[32] Yu, B., Zebarjadi, M., Wang, H., Lukas, K., Wang, H., Wang, D., . . . Ren, Z. (2012). Enhancement of Thermoelectric Properties by Modulation-Doping in Silicon Germanium Alloy Nanocomposites. *Nano Lett., 12*(4), 2077-2082. doi:10.1021/nl3003045

[33] Zebarjadi, M., Joshi, G., Zhu, G., Yu, B., Minnich, A., Lan, Y., . . . Chen, G. (2011). Power Factor Enhancement by Modulation Doping in Bulk Nanocomposites. *Nano Lett., 11*(6), 2225-2230. doi:10.1021/nl201206d

[34] Fleurial, J.-P. (2009). Thermoelectric power generation materials: Technology and application opportunities. *JOM, 61*(4), 79-85. doi:10.1007/s11837-009-0057-z

[35] Heusler, F. (1903). Ü ber magnetische manganlegierungen. *Verhandlungen der Deutschen Physikalischen Gesellschaft, 5*, 219.

[36] Bhattacharya, S., Pope, A. L., Littleton, R. T., Tritt, T. M., Ponnambalam, V., Xia, Y., & Poon, S. J. (2000). Effect of Sb doping on the thermoelectric properties of Ti-based half-Heusler compounds, $TiNiSn_{1-x}Sb_x$. *Appl. Phys. Lett., 77*(16), 2476-2478. doi:10.1063/1.1318237

[37] Lee, M.-S., Poudeu, F. P., & Mahanti, S. D. (2011). Electronic structure and thermoelectric properties of Sb-based semiconducting half-Heusler compounds. *Phys. Rev. B, 83*(8), 085204. doi:10.1103/PhysRevB.83.085204

[38] Larson, P., Mahanti, S. D., Sportouch, S., & Kanatzidis, M. G. (1999). Electronic structure of rare-earth nickel pnictides: Narrow-gap thermoelectric materials. *Phys. Rev. B, 59*(24), 15660-15668. doi:10.1103/PhysRevB.59.15660

[39] Wang, X. W., Lee, H., Lan, Y. C., Zhu, G. H., Joshi, G., Wang, D. Z., . . . Ren, Z. F. (2008). Enhanced thermoelectric figure of merit in nanostructured n-type silicon germanium bulk alloy. *Appl. Phys. Lett., 93*(19), 193121. doi:Artn 19312110.1063/1.3027060

[40] Joshi, G., Lee, H., Lan, Y., Wang, X., Zhu, G., Wang, D., . . . Ren, Z. (2008). Enhanced thermoelectric figure-of-merit in nanostructured p-type silicon germanium bulk alloys. *Nano Lett, 8*(12), 4670-4674. doi:10.1021/nl8026795

[41] Heremans, J. P., Jovovic, V., Toberer, E. S., Saramat, A., Kurosaki, K., Charoenphakdee, A., . . . Snyder, G. J. (2008). Enhancement of Thermoelectric Efficiency in PbTe by Distortion of the Electronic Density of States. *Science, 321*(5888), 554-557.

[42] Biswas, K., He, J. Q., Blum, I. D., Wu, C. I., Hogan, T. P., Seidman, D. N., . . . Kanatzidis, M. G. (2012). High-performance bulk thermoelectrics with all-scale hierarchical architectures. *Nature, 489*(7416), 414-418.

[43] Liu, W. S., Yan, X., Chen, G., & Ren, Z. F. (2012). Recent advances in thermoelectric nanocomposites. *Nano Energy, 1*(1), 42-56. doi:10.1016/j.nanoen.2011.10.001

[44] Chen, S., Lukas, K. C., Liu, W. S., Opeil, C. P., Chen, G., & Ren, Z. F. (2013). Effect of Hf Concentration on Thermoelectric Properties of Nanostructured N-Type Half-Heusler Materials $Hf_xZr_{1-x}NiSn_{0.99}Sb_{0.01}$. *Adv. Energy Mater., 3*(9), 1210-1214. doi:10.1002/aenm.201300336

[45] Chen, L., Gao, S., Zeng, X., Dehkordi, A. M., Tritt, T. M., & Poon, S. J. (2015). Uncovering high thermoelectric figure of merit in (Hf,Zr)NiSn half-Heusler alloys. *Appl. Phys. Lett., 107*(4), 041902. doi:10.1063/1.4927661

[46] Kim, K. S., Kim, Y.-M., Mun, H., Kim, J., Park, J., Borisevich, A. Y., . . . Kim, S. W. (2017). Direct Observation of Inherent Atomic-Scale Defect Disorders responsible for High-Performance $Ti_{1-x}Hf_xNiSn_{1-y}Sb_y$ Half-Heusler Thermoelectric Alloys. *Adv. Mater., 29*(36), 170209. doi:10.1002/adma.201702091

[47] Liu, Y. T., Fu, C. G., Xia, K. Y., Yu, J. J., Zhao, X. B., Pan, H. G., . . . Zhu, T. J. (2018). Lanthanide Contraction as a Design Factor for High-Performance Half-Heusler Thermoelectric Materials. *Adv. Mater., 30*(32), 1800881. doi:10.1002/adma.201800881

[48] Joshi, G., He, R., Engber, M., Samsonidze, G., Pantha, T., Dahal, E., . . . Ren, Z. (2014). NbFeSb-based p-type half-Heuslers for power generation applications. *Energy Environ. Sci., 7*(12), 4070-4076. doi:10.1039/C4EE02180K

[49] Rausch, E., Balke, B., Stahlhofen, J. M., Ouardi, S., Burkhardt, U., & Felser, C. (2015). Fine tuning of thermoelectric performance in phase-separated half-Heusler compounds. *J. Mater. Chem. C, 3*(40), 10409-10414. doi:10.1039/c5tc01196e

[50] Zhu, H. T., He, R., Mao, J., Zhu, Q., Li, C. H., Sun, J. F., . . . Ren, Z. F. (2018). Discovery of ZrCoBi based half Heuslers with high thermoelectric conversion efficiency. *Nature Communications, 9*, 9. doi:10.1038/s41467-018-04958-3

[51] Zhu, H., Mao, J., Li, Y., Sun, J., Wang, Y., Zhu, Q., . . . Ren, Z. (2019). Discovery of TaFeSb-based half-Heuslers with high thermoelectric performance. *Nat Commun, 10*(1), 270. doi:10.1038/s41467-018-08223-5

[52] Shen, Q., Chen, L., Goto, T., Hirai, T., Yang, J., Meisner, G. P., & Uher, C. (2001). Effects of partial substitution of Ni by Pd on the thermoelectric properties of ZrNiSn-based half-Heusler compounds. *Appl. Phys. Lett., 79*(25), 4165-4167. doi:10.1063/1.1425459

[53] Sakurada, S., & Shutoh, N. (2005). Effect of Ti substitution on the thermoelectric properties of (Zr,Hf)NiSn half-Heusler compounds. *Appl. Phys. Lett., 86*(8). doi:10.1063/1.1868063

[54] Culp, S. R., Poon, S. J., Hickman, N., Tritt, T. M., & Blumm, J. (2006). Effect of substitutions on the thermoelectric figure of merit of half-Heusler phases at 800 degrees C. *Appl. Phys. Lett., 88*(4), 042106. doi:10.1063/1.2168019

[55] Kouacou, M. A., Pierre, J., & Skolozdra, R. V. (1995). Semiconductor-metal transition and the onset of itinerant ferromagnetism in the Heusler phases TiCoSn-TiCoSb. *Journal of Physics: Condensed Matter, 7*(37), 7373-7385. doi:10.1088/0953-8984/7/37/010

[56] Xia, Y., Bhattacharya, S., Ponnambalam, V., Pope, A. L., Poon, S. J., & Tritt, T. M. (2000). Thermoelectric properties of semimetallic (Zr, Hf)CoSb half-Heusler phases. *J. Appl. Phys., 88*(4), 1952-1955. doi:10.1063/1.1305829

[57] Sekimoto, T., Kurosaki, K., Muta, H., & Yamanaka, S. (2006). Thermoelectric properties of Sn-doped TiCoSb half-Heusler compounds. *J. Alloy. Compd., 407*(1-2), 326-329. doi:10.1016/j.jallcom.2005.06.036

[58] Kawano, K., Kurosaki, K., Sekimoto, T., Muta, H., & Yamanaka, S. (2007). Effect of Sn doping on the thermoelectric properties of ErNiSb-based p-type half-Heusler compound. *Appl. Phys. Lett., 91*(6). doi:10.1063/1.2769398

[59] Sekimoto, T., Kurosaki, K., Muta, H., & Yamanaka, S. (2007). High-thermoelectric figure of merit realized in p-type half-Heusler compounds: $ZrCoSn_xSb_{1-x}$. *Japanese Journal of Applied Physics Part 2-Letters & Express Letters, 46*(25-28), L673-L675. doi:10.1143/Jjap.46.L673

[60] Ponnambalam, V., Alboni, P. N., Edwards, J., Tritt, T. M., Culp, S. R., & Poon, S. J. (2008). Thermoelectric properties of p-type half-Heusler alloys $Zr_{1-x}Ti_xCoSn_ySb_{1-y}$ ($0.0 < x < 0.5$; y=0.15 and 0.3). *J. Appl. Phys., 103*(6). doi:10.1063/1.2896591

[61] Zhu, T. J., Fu, C. G., Xie, H. H., Liu, Y. T., & Zhao, X. B. (2015). High Efficiency Half-Heusler Thermoelectric Materials for Energy Harvesting. *Adv. Energy Mater., 5*(19), 1500588.

[62] Fu, C., Zhu, T., Pei, Y., Xie, H., Wang, H., Snyder, G. J., . . . Zhao, X. (2014). High Band Degeneracy Contributes to High Thermoelectric Performance in p-Type Half-Heusler Compounds. *Adv. Energy Mater., 4*(18), n/a-n/a. doi:10.1002/aenm.201400600

[63] Fu, C. G., Zhu, T. J., Liu, Y. T., Xie, H. H., & Zhao, X. B. (2015). Band engineering of high performance p-type FeNbSb based half-Heusler thermoelectric materials for figure of merit zT > 1. *Energy Environ. Sci., 8*(1), 216-220. doi:10.1039/c4ee03042g

[64] Joshi, G., & Poudel, B. (2016). Efficient and robust thermoelectric power generation device using hot-pressed metal contacts on nanostructured half-Heusler alloys. *J. Electron. Mater., 45*(12), 6047-6051.

[65] He, R., Huang, L. H., Wang, Y. M., Samsonidze, G., Kozinsky, B., Zhang, Q. Y., & Ren, Z. F. (2016). Enhanced thermoelectric properties of n-type NbCoSn half-Heusler by improving phase purity. *APL Mater., 4*(10), 104804. doi:10.1063/1.4952994

[66] Rausch, E., Balke, B., Deschauer, T., Ouardi, S., & Felser, C. (2015). Charge carrier concentration optimization of thermoelectric p-type half-Heusler compounds. *APL Mater., 3*(4), 041516. doi:10.1063/1.4916526

[67] Douglas, J. E., Birkel, C. S., Verma, N., Miller, V. M., Miao, M. S., Stucky, G. D., . . . Seshadri, R. (2014). Phase stability and property evolution of biphasic Ti-Ni-Sn alloys for use in thermoelectric applications. *J. Appl. Phys., 115*(4), 043720. doi:10.1063/1.4862955

[68] Hazama, H., Matsubara, M., Asahi, R., & Takeuchi, T. (2011). Improvement of thermoelectric properties for half-Heusler TiNiSn by interstitial Ni defects. *J. Appl. Phys., 110*(6), 063710. doi:10.1063/1.3633518

[69] Minnich, A. J., Dresselhaus, M. S., Ren, Z. F., & Chen, G. (2009). Bulk nanostructured thermoelectric materials: current research and future prospects. *Energy Environ. Sci., 2*(5), 466-479. doi:10.1039/B822664B

[70] Sekimoto, T., Kurosaki, K., Muta, H., & Yamanaka, S. (2005). Annealing effect on thermoelectric properties of TiCoSb half-Heusler compound. *J. Alloy. Compd., 394*(1-2), 122-125. doi:10.1016/j.jallcom.2004.11.017

[71] Qiu, P. F., Yang, J., Huang, X. Y., Chen, X. H., & Chen, L. D. (2010). Effect of antisite defects on band structure and thermoelectric performance of ZrNiSn half-Heusler alloys. *Appl. Phys. Lett., 96*(15). doi:10.1063/1.3396981

[72] Xie, H.-H., Mi, J.-L., Hu, L.-P., Lock, N., Chirstensen, M., Fu, C.-G., . . . Zhu, T.-J. (2012). Interrelation between atomic switching disorder and thermoelectric properties of ZrNiSn half-Heusler compounds. *Cryst. Eng. Comm, 14*(13), 4467-4471. doi:10.1039/C2CE25119A

[73] Hu, C., Xia, K., Chen, X., Zhao, X., & Zhu, T. (2018). Transport mechanisms and property optimization of p-type (Zr, Hf) CoSb half-Heusler thermoelectric materials. *Mater. Today Phys., 7*, 69-76. doi:10.1016/j.mtphys.2018.11.002

[74] Yuan, B., Wang, B., Huang, L., Lei, X., Zhao, L., Wang, C., & Zhang, Q. (2017). Effects of Sb Substitution by Sn on the Thermoelectric Properties of ZrCoSb. *J. Electron. Mater., 46*(5), 3076-3082. doi:10.1007/s11664-016-5168-z

[75] He, R., Kim, H. S., Lan, Y., Wang, D., Chen, S., & Ren, Z. (2014). Investigating the thermoelectric properties of p-type half-Heusler $Hfx(ZrTi)_{1-x}CoSb_{0.8}Sn_{0.2}$ by reducing Hf concentration for power generation. *RSC Advances, 4*(110), 64711-64716. doi:10.1039/C4RA14343D

[76] Faleev, S. V., & Léonard, F. (2008). Theory of enhancement of thermoelectric properties of materials with nanoinclusions. *Phys. Rev. B, 77*(21), 214304.

[77] Zebarjadi, M., Esfarjani, K., Shakouri, A., Bahk, J.-H., Bian, Z., Zeng, G., . . . Gossard, A. (2009). Effect of nanoparticle scattering on thermoelectric power factor. *Appl. Phys. Lett., 94*(20), 202105.

[78] Zebarjadi, M., Esfarjani, K., Shakouri, A., Bian, Z., Bahk, J.-H., Zeng, G., . . . Gossard, A. (2009). Effect of Nanoparticles on Electron and Thermoelectric Transport. *J. Electron. Mater., 38*(7), 954-959.

[79] Heremans, J. P., Thrush, C. M., & Morelli, D. T. (2005). Thermopower enhancement in PbTe with Pb precipitates. *J. Appl. Phys., 98*(6), 063703.

[80] Sumithra, S., Takas, N. J., Misra, D. K., Nolting, W. M., Poudeu, P. F. P., & Stokes, K. L. (2011). Enhancement in Thermoelectric Figure of Merit in Nanostructured Bi_2Te_3 with Semimetal Nanoinclusions. *Adv. Energy Mater., 1*(6), 1141-1147.

[81] Sahoo, P., Liu, Y. F., & Poudeu, P. F. P. (2014). Nanometer-scale interface engineering boosts the thermoelectric performance of n-type $Ti_{0.4}Hf_{0.6}Ni_{1+z}Sn_{0.975}Sb_{0.025}$ alloys. *J. Mater. Chem. A, 2*(24), 9298-9305.

[82] Xie, W. J., Yan, Y. G., Zhu, S., Zhou, M., Populoh, S., Galazka, K., . . . Tritt, T. M. (2013). Significant ZT enhancement in p-type Ti(Co,Fe)Sb-InSb nanocomposites via a synergistic high-mobility electron injection, energy-filtering and boundary-scattering approach. *Acta Mater., 61*(6), 2087-2094.

[83] Makongo, J. P. A., Misra, D. K., Zhou, X., Pant, A., Shabetai, M. R., Su, X., . . . Poudeu, P. F. P. (2011). Simultaneous Large Enhancements in Thermopower and Electrical Conductivity of Bulk Nanostructured Half-Heusler Alloys. *J. Am. Chem. Soc, 133*(46), 18843-18852.

[84] Xie, W. J., He, J., Zhu, S., Su, X. L., Wang, S. Y., Holgate, T., . . . Tritt, T. M. (2010). Simultaneously optimizing the independent thermoelectric properties in (Ti,Zr,Hf)(Co,Ni)Sb alloy by in situ forming InSb nanoinclusions. *Acta Mater., 58*(14), 4705-4713.

[85] Hsu, C. C., Liu, Y. N., & Ma, H. K. (2014). Effect of the $Zr_{0.5}Hf_{0.5}CoSb_{1-x}Sn_x/HfO_2$ half-Heusler nanocomposites on the ZT value. *J. Alloy. Compd., 597*, 217-222. doi:10.1016/j.jallcom.2014.01.208

[86] Schwall, M., & Balke, B. (2013). Phase separation as a key to a thermoelectric high efficiency. *Phys. Chem. Chem. Phys., 15*(6), 1868-1872. doi:10.1039/c2cp43946h

[87] Zhao, H., Cao, B., Li, S., Liu, N., Shen, J., Li, S., . . . Chen, X. (2017). Engineering the Thermoelectric Transport in Half-Heusler Materials through a Bottom-Up Nanostructure Synthesis. *Adv. Energy Mater., 7*(18), 1700446. doi:10.1002/aenm.201700446

[88] Yu, C., Xie, H., Fu, C., Zhu, T., & Zhao, X. (2012). High performance half-Heusler thermoelectric materials with refined grains and nanoscale precipitates. *J. Mater. Res., 27*(19), 2457-2465. doi:10.1557/jmr.2012.171

[89] Visconti, A., Bernard-Granger, G., Navone, C., Leforestier, J., & Mingo, N. (2016). Microstructure investigations and thermoelectric properties of an N-type Half-Heusler alloy sintered by spark plasma sintering. *Scr. Mater., 123*, 100-104. doi:https://doi.org/10.1016/j.scriptamat.2016.05.045

[90] Zhang, M. X., & Kelly, P. M. (2005). Edge-to-edge matching model for predicting orientation relationships and habit planes—the improvements. *Scr. Mater., 52*(10), 963-968.

[91] Cutler, M., & Mott, N. F. (1969). Observation of Anderson Localization in an Electron Gas. *Phys. Rev., 181*(3), 1336-1340.

[92] Liu, Y., Cadavid, D., Ibáñez, M., Ortega, S., Martí-Sánchez, S., Dobrozhan, O., . . . Cabot, A. (2016). Thermoelectric properties of semiconductor-metal composites produced by particle blending. *APL Mater., 4*(10), 104813.

[93] Muta, H., Kanemitsu, T., Kurosaki, K., & Yamanaka, S. (2006). Substitution effect on thermoelectric properties of ZrNiSn based half-Heusler compounds. *Mater. Trans., 47*(6), 1453-1457.

[94] Zhang, J., Wu, D., He, D. S., Feng, D., Yin, M. J., Qin, X. Y., & He, J. Q. (2017). Extraordinary Thermoelectric Performance Realized in n-Type PbTe through Multiphase Nanostructure Engineering. *Adv. Mater., 29*(39), 1703148.

[95] Berche, A., & Jund, P. (2018). Oxidation of half-Heusler NiTiSn materials: Implications for thermoelectric applications. *Intermetallics, 92*, 62-71. doi:10.1016/j.intermet.2017.09.014

[96] Galazka, K., Populoh, S., Sagarna, L., Karvonen, L., Xie, W. J., Beni, A., . . . Weidenkaff, A. (2014). Phase formation, stability, and oxidation in (Ti, Zr, Hf)NiSn half-Heusler compounds. *Phys. Status Solidi A, 211*(6), 1259-1266. doi:10.1002/pssa.201300209

[97] Polak, M., & Rubinovich, L. (2000). The interplay of surface segregation and atomic order in alloys. *Surf. Sci. Rep., 38*(4), 127-194. doi:https://doi.org/10.1016/S0167-5729(99)00010-2

[98] Appel, O., Cohen, S., Beeri, O., Shamir, N., Gelbstein, Y., & Zalkind, S. (2018). Surface Oxidation of TiNiSn (Half-Heusler) Alloy by Oxygen and Water Vapor. *Materials (Basel, Switzerland), 11*(11), 2296. doi:10.3390/ma11112296

[99] Vitos, L., Ruban, A. V., Skriver, H. L., & Kollar, J. (1998). The surface energy of metals. *Surf. Sci., 411*(1-2), 186-202. doi:Doi 10.1016/S0039-6028(98)00363-X

[100] Silpawilawan, W., Kurosaki, K., Ohishi, Y., Muta, H., & Yamanaka, S. (2017). FeNbSb p-type half-Heusler compound: beneficial thermomechanical properties and high-temperature stability for thermoelectrics. *J. Mater. Chem. C, 5*(27), 6677-6681. doi:10.1039/C7TC01570D

[101] Young, D., Zhang, J., Geers, C., & Schütze, M. (2011). Recent advances in understanding metal dusting: A review. *Mater. Corros., 62*(1), 7-28.

[102] Geers, C., Galetz, M., & Schütze, M. (2013). Investigation of the effect of the alloy 600 substrate for the stability of a Ni_3Sn_2 coating for metal dusting protection at 620°C. *Surf. Coat. Technol., 215*, 2-6. doi:https://doi.org/10.1016/j.surfcoat.2012.04.100

[103] Pei, Y., Wang, H., & Snyder, G. J. (2012). Band Engineering of Thermoelectric Materials. *Adv. Mater., 24*(46), 6125-6135. doi:10.1002/adma.201202919

[104] Lin, H., Wray, L. A., Xia, Y. Q., Xu, S. Y., Jia, S. A., Cava, R. J., . . . Hasan, M. Z. (2010). Half-Heusler ternary compounds as new multifunctional experimental platforms for topological quantum phenomena. *Nat. Mater., 9*(7), 546-549. doi:10.1038/nmat2771

[105] Anand, S., Xia, K., Zhu, T., Wolverton, C., & Snyder, G. J. (2018). Temperature Dependent n-Type Self Doping in Nominally 19-Electron Half-Heusler Thermoelectric Materials. *Adv. Energy Mater., 8*(30), 1801409. doi:doi:10.1002/aenm.201801409

[106] Li, Z.-Y., & Li, J.-F. (2014). Fine-Grained and Nanostructured $AgPb_mSbTe_{m+2}$ Alloys with High Thermoelectric Figure of Merit at Medium Temperature. *Adv. Energy Mater., 4*(2), 1300937. doi:10.1002/aenm.201300937

[107] Li, J. F., Liu, W. S., Zhao, L. D., & Zhou, M. (2010). High-performance nanostructured thermoelectric materials. *Npg Asia Materials, 2*(4), 152-158. doi:10.1038/asiamat.2010.138

[108] Vineis, C. J., Shakouri, A., Majumdar, A., & Kanatzidis, M. G. (2010). Nanostructured Thermoelectrics: Big Efficiency Gains from Small Features. *Adv. Mater., 22*(36), 3970-3980. doi:10.1002/adma.201000839

[109] Nielsch, K., Bachmann, J., Kimling, J., & Böttner, H. (2011). Thermoelectric Nanostructures: From Physical Model Systems towards Nanograined Composites. *Adv. Energy Mater., 1*(5), 713-731. doi:10.1002/aenm.201100207

[110] Yan, X., Liu, W., Chen, S., Wang, H., Zhang, Q., Chen, G., & Ren, Z. (2013). Thermoelectric Property Study of Nanostructured p-Type Half-Heuslers (Hf, Zr, Ti)$CoSb_{0.8}Sn_{0.2}$. *Adv. Energy Mater., 3*(9), 1195-1200. doi:10.1002/aenm.201200973

[111] Qiu, Q., Liu, Y., Xia, K., Fang, T., Yu, J., Zhao, X., & Zhu, T. (2019). Grain Boundary Scattering of Charge Transport in n-Type (Hf,Zr)CoSb Half-Heusler Thermoelectric Materials. *Adv. Energy Mater., 9*(11), 1803447. doi:10.1002/aenm.201803447

[112] Schrade, M., Berland, K., Eliassen, S. N. H., Guzik, M. N., Echevarria-Bonet, C., Sorby, M. H., . . . Finstad, T. G. (2017). The role of grain boundary scattering in reducing the thermal conductivity of polycrystalline XNiSn (X = Hf, Zr, Ti) half-Heusler alloys. *Sci Rep, 7*(1), 13760. doi:10.1038/s41598-017-14013-8

[113] Yu, J. J., Fu, C. G., Liu, Y. T., Xia, K. Y., Aydemir, U., Chasapis, T. C., . . . Zhu, T. J. (2018). Unique Role of Refractory Ta Alloying in Enhancing the Figure of Merit of NbFeSb Thermoelectric Materials. *Adv. Energy Mater., 8*(1), 1701313. doi:ARTN 170131310.1002/aenm.201701313

[114] Li, S. K., Liu, X. R., Liu, Y. D., Liu, F. S., Luo, J., & Pan, F. (2017). Optimized hetero-interfaces by tuning 2D SnS_2 thickness in $Bi_2Te_{2.7}Se_{0.3}/SnS_2$ nanocomposites to enhance thermoelectric performance. *Nano Energy, 39,* 297-305. doi:10.1016/j.nanoen.2017.07.011

[115] You, L., Liu, Y., Li, X., Nan, P., Ge, B., Jiang, Y., . . . Luo, J. (2018). Boosting the thermoelectric performance of PbSe through dynamic doping and hierarchical phonon scattering. *Energy Environ. Sci., 11*(7), 1848-1858. doi:10.1039/C8EE00418H

[116] Sootsman, J. R., Chung, D. Y., & Kanatzidis, M. G. (2009). New and Old Concepts in Thermoelectric Materials. *Angew. Chem. Int. Ed., 48*(46), 8616-8639. doi:10.1002/anie.200900598

[117] Jung, D., Kurosaki, K., Kim, C., Muta, H., & Yamanaka, S. (2010). Thermal expansion and melting temperature of the half-Heusler compounds: MNiSn (M = Ti, Zr, Hf). *J. Alloy. Compd., 489*(2), 328-331. doi:10.1016/j.jallcom.2009.09.139

[118] Lee, H., Sharp, J., Stokes, D., Pearson, M., & Priya, S. (2018). Modeling and analysis of the effect of thermal losses on thermoelectric generator performance using effective properties. *Appl. Energy, 211,* 987-996.

[119] Liu, W., Wang, H., Wang, L., Wang, X., Joshi, G., Chen, G., & Ren, Z. (2013). Understanding of the contact of nanostructured thermoelectric n-type $Bi_2Te_{2.7}Se_{0.3}$ legs for power generation applications. *J. Mater. Chem. A, 1*(42), 13093-13100.

[120] Ka, X., Weichao, W., Husam, N. A., Rahul, P. G., John, B. W., Bruce, E. G., & Kyeongjae, C. (2010). Electronic structures and stability of Ni/Bi_2Te_3 and Co/Bi_2Te_3 interfaces. *J. Phys. D, 43*(11), 115303.

[121] Bartholome, K., Balke, B., Zuckermann, D., Kohne, M., Muller, M., Tarantik, K., & Konig, J. (2014). Thermoelectric Modules Based on Half-Heusler Materials Produced in Large Quantities. *J. Electron. Mater., 43*(6), 1775-1781.

[122] Zhang, Y., Cleary, M., Wang, X., Kempf, N., Schoensee, L., Yang, J., . . . Meda, L. (2015). High-temperature and high-power-density nanostructured thermoelectric generator for automotive waste heat recovery. *Energ. Convers. Manage., 105*, 946-950.